Doctoral Dissertation

Physicochemical Properties and Oxidation Reactivities of Mononuclear Tetrahedral Copper(II) Complexes

Lan Yang

January 2025

Bio-functional Chemistry Laboratory

Division of Applied Chemistry

Graduate School of Engineering

Osaka University

Contents

General Introduction 1

Chapter 1. Characterization and Reactivity Studies of Mononuclear Tetrahedral Copper(II)-halide Complexes..... 5

Chapter 2. Oxidation Mechanism of Phenols by Copper(II)-halide Complexes 39

Chapter 3. Oxidation Reactivity of Mononuclear Tetrahedral Copper(II)-methoxide Complex..... 59

General Conclusion 79

List of publications 80

Acknowledgement 81

General Introduction

In this study, a N_3-tridentate ligand, TMG_3tach, consisting with a rigid *cis,cis*-1,3,5-triaminocyclohexane (tach) framework and three TMG (*N,N,N',N'*-tetramethyl-guanidino) donor groups (Chart 1(a)) was used to prepare a mononuclear tetrahedral copper(II) complexes containing a labile axial coordination site.[5,6] The TMG group has attracted much recent attention as a strongly electron-donating group in coordination chemistry.[7-10] The tach derivatives have been adopted to construct transition-metal complexes with tetrahedral geometry, which can mimic the reaction centers for biological activation and binding of small molecules.[11-15] By using this TMG_3tach ligand, the mononuclear tetrahedral copper(II) complexes with a series of halide and methoxide axial ligands, $[Cu^{II}(TMG_3tach)(L)]^+$ ($\mathbf{1^L}$; L = F^-, Cl^-, Br^-, I^- and MeO^-) (Chart 1(b)), have been prepared and characterized to get insights into the labile coordination site effect on the chemical properties and redox reactivity.

Chart 1. (a) Ligand TMG_3tach. (b) Copper(II) complexes $[Cu^{II}(TMG_3tach)(L)]^+$ $\mathbf{1^L}$ used in this research.

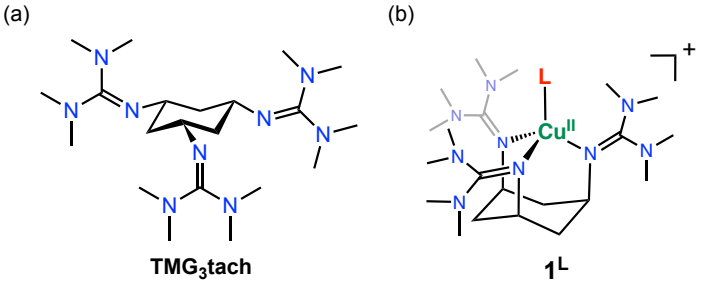

Physicochemical properties and reactivities of copper complexes are largely controlled by the coordination geometry of the metal centers.[1] To get insights into the chemical properties and functions of the mononuclear tetrahedral copper reaction centers found in dopamine β-monooxygenases (DβM), peptidylglycine α-hydroxylating monooxygenase (PHM), and blue copper proteins, copper model complexes need to be developed. The first example of biomimetic mononuclear tetrahedral copper(II) complex was prepared by Kitajima and co-workers using well-known hydrotrispyrazolylborate (Tp) ligands.[2-4] In their model system, copper(II) complexes having a tetrahedral geometry were easily changed to a five-coordinate square-pyramidal geometry upon addition of a slight amount of a coordinating solvent such as DMSO or DMF making reactivity studies on these copper(II) complexes difficult.[2] Thus, it is rather difficult to develop such copper(II) complexes having a tetrahedral geometry, since

copper(II) ion favors the square planer, square pyramidal, or trigonal bipyramidal geometry.

Scheme 1. C–H activation by tetrahedral copper(II)-halide complexes.

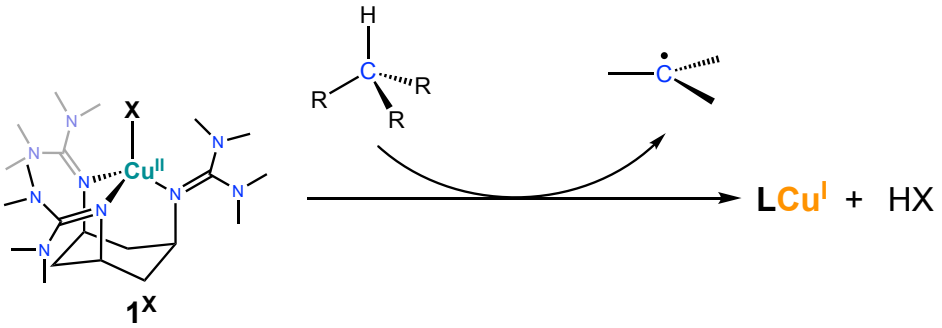

In Chapter 1, the structures, physicochemical properties, and reactivity of the whole series of copper(II)-halide complexes ($\mathbf{1}^{\mathbf{X}}$; X = F^-, Cl^-, Br^-, and I^-) were examined using TMG_3tach tridentate supporting ligand consisting of *cis,cis*-1,3,5-triaminocyclohexane (tach) and *N,N,N',N'*-tetramethylguanidine (TMG). The tach ligand framework with the bulky and strongly electron donating TMG substituents enforced the copper(II) complexes to take a tetrahedral geometry as inferred from the electron paramagnetic resonance (EPR) spectra exhibiting relatively large g_z and small A_z values. The electronic absorption spectra of $\mathbf{1}^{\mathbf{X}}$ agreed with the simulation spectra obtained by time-dependent density functional theory (TD-DFT) calculations on a slightly distorted tetrahedral geometry. $\mathbf{1}^{\mathbf{I}}$ and $\mathbf{1}^{\mathbf{Br}}$ gradually decomposed to generate the corresponding copper(I) complex and halide radical X•, and in the case of $\mathbf{1}^{\mathbf{Br}}$, intramolecular hydroxylation of a methyl group of the TMG substituent took place under aerobic conditions, that may be caused by the reaction of generated copper(I) complex and dioxygen (O_2) generating a reactive oxygen species. $\mathbf{1}^{\mathbf{X}}$ except $\mathbf{1}^{\mathbf{I}}$ showed hydrogen atom abstraction (HAA) reactivity towards cyclohexadiene (CHD), where $\mathbf{1}^{\mathbf{F}}$ exhibited the highest reactivity with a second-order rate constant as 1.4×10^{-3} M^{-1} s^{-1} at 25°C. Such a HAA reactivity can be attributed to the basicity of F^- and unstable copper(II) electronic state in the tetrahedral geometry.

In Chapter 2, the oxidation mechanism of phenols by the tetrahedral copper(II)-halide complexes $\mathbf{1}^{\mathbf{X}}$ was investigated to demonstrate that phenols with an electron-withdrawing substituent are oxidized *via* a proton-transfer/electron-transfer (PTET) mechanism, whereas the oxidation of phenols with an electron-donating substituent

involves a concerted proton/electron transfer (CPET) mechanism (Scheme 2).

Scheme 2. O–H activation by tetrahedral copper(II)-halide complexes

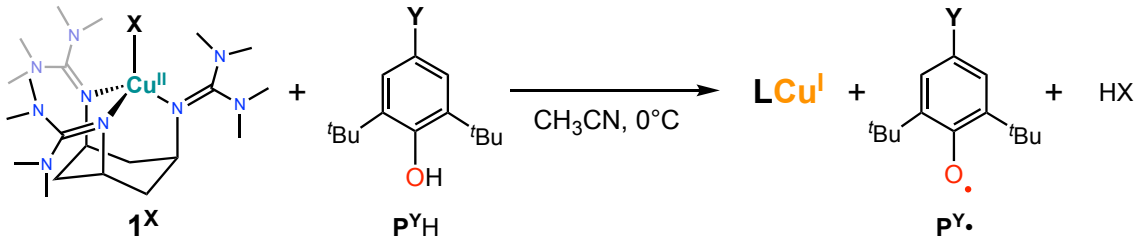

In Chapter 3, reactivity of a mononuclear tetrahedral copper(II)-methoxide complex $\mathbf{1}^{\mathbf{OMe}}$ was examined in the C–H and O–H bond activation reactions using 1,4-cyclohexadiene (CHD), 4-substituted-2,6-di-*tert*-butylphenol ($\mathbf{P}^{\mathbf{Y}}$H), and 2,2,6,6-tetramethylpiperidin-1-ol (TEMPOH) as the substrates. In these reactions, $\mathbf{1}^{\mathbf{OMe}}$ showed much higher reactivity compared to the copper(II)-halide complexes $\mathbf{1}^{\mathbf{X}}$. Such an enhanced reactivity can be attributed to higher basicity of the methoxide (MeO^-) axial ligand compared to those of halide (X^-) ligands.

Scheme 3. Reactivity studies on tetrahedral copper(II)-methoxide complexes

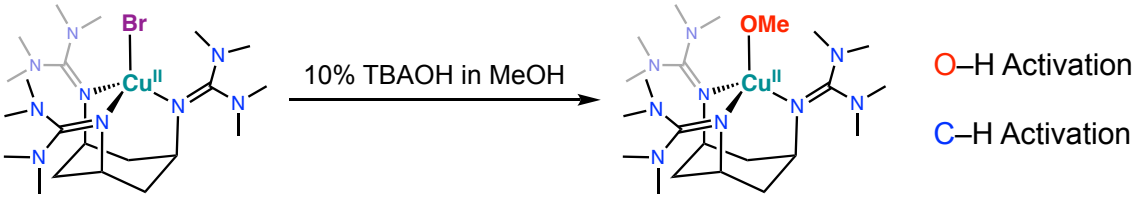

In this research, physicochemical properties and oxidation reactivities of mononuclear tetrahedral copper(II) complexes supported by TMG_3tach were examined in detail. These copper(II) complexes $\mathbf{1}^{\mathbf{L}}$ have been proved to have the ability of C–H and O–H activation, even though the metal ion has a normal copper(II) oxidation state but not a high-valent oxidation state such as copper(III). Such an oxidation reactivity is attributed to the tetrahedral geometry of copper(II) center which basically stabilizes the low-valent copper(I) oxidation.

Reference

(1) Solomon, E. I.; Heppner, D. E.; Johnston, E. M.; Ginsbach, J. W.; Cirera, J.; Qayyum, M.; Kieber-Emmons, M. T.; Kjaergaard, C. H.; Hadt, R. G.; Tian, L., *Chem. Rev.*, **2014**, *114*, 3659-3853.

(2) Kitajima, N.; Fujisawa, K.; Morooka, Y., *J. Am. Chem. Soc.*, **1990**, *112*, 3210-3212.
(3) Kitajima, N.; Fujisawa, K.; Tanaka, M.; Morooka, Y., *J. Am. Chem. Soc.*, **1992**, *114*, 9232-9233.
(4) Kitajima, N.; Katayama, T.; Fujisawa, K.; Iwata, Y.; Morooka, Y., *J. Am. Chem. Soc.*, **1993**, *115*, 7872-7873.
(5) Shimizu, I.; Morimoto, Y.; Faltermeier, D.; Kerscher, M.; Paria, S.; Abe, T.; Sugimoto, H.; Fujieda, N.; Asano, K.; Suzuki, T., *Inorg. Chem.*, **2017**, *56*, 9634-9645.
(6) Shimizu, I.; Morimoto, Y.; Velmurugan, G.; Gupta, T.; Paria, S.; Ohta, T.; Sugimoto, H.; Ogura, T.; Comba, P.; Itoh, S., *Chem. Eur. J.*, **2019**, *25*, 11157-11165.
(7) Neuba, A.; Flörke, U.; Meyer-Klaucke, W.; Salomone-Stagni, M.; Bill, E.; Bothe, E.; Höfer, P.; Henkel, G., *Angew. Chem. Int. Ed.*, **2011**, *50*, 4503-4507.
(8) Neuba, A.; Haase, R.; Meyer-Klaucke, W.; Flörke, U.; Henkel, G., *Angew. Chem. Int. Ed.*, **2012**, *51*, 1714-1718.
(9) Hoffmann, A.; Binder, S.; Jesser, A.; Haase, R.; Flörke, U.; Gnida, M.; Salomone-Stagni, M.; Meyer-Klaucke, W.; Lebsanft, B.; Grünig, L. E., *Angew. Chem. Int. Ed.*, **2014**, *53*, 299-304.
(10) Bagchi, V.; Paraskevopoulou, P.; Das, P.; Chi, L.; Wang, Q.; Choudhury, A.; Mathieson, J. S.; Cronin, L.; Pardue, D. B.; Cundari, T. R., *J. Am. Chem. Soc.*, **2014**, *136*, 11362-11381.
(11) Cronin, L.; Greener, B.; Foxon, S. P.; Heath, S. L.; Walton, P. H., *Inorg. Chem.*, **1997**, *36*, 2594-2600.
(12) J. Boxwell, C.; H. Walton, P., *Chem. Commun.*, **1999**, 1647-1648.
(13) Greener, B.; Foxon, S. P.; Walton, P. H., *New J. Chem.*, **2000**, *24*, 269-273.
(14) Park, G.; Shao, J.; Lu, F. H.; Rogers, R. D.; Chasteen, N. D.; Brechbiel, M. W.; Planalp, R. P., *Inorg. Chem.*, **2001**, *40*, 4167-4175.
(15) Arii, H.; Saito, Y.; Nagatomo, S.; Kitagawa, T.; Funahashi, Y.; Jitsukawa, K.; Masuda, H., *Chem. Lett.*, **2003**, *32*, 156-157.

Chapter 1. Characterization and Reactivity Studies of Mononuclear Tetrahedral Copper(II)-halide Complexes

Introduction

Copper(II) complexes favor to take square planar, square pyramidal, or trigonal bipyramidal structure. However, some copper monooxygenases such as peptidylglycine α-hydroxylating monooxygenase (PHM) and dopamine *β*-monooxygenase (D*β*M) have a mononuclear tetrahedrally distorted copper reaction center having a labile coordination site for dioxygen binding and activation.[1,2] Thus, it is highly desired to explore the redox reactivity of copper(II) complexes having such an unusual structural feature. In this context, *cis,cis*-1,3,5-triamino-cyclohexane (tach) provides an ideal ligand framework that can enforce the metal ion to take a tetrahedral (Td) geometry with an axial coordination site for the binding of an external substrate.[3-11] However, the strong tendency of copper(II) ion to take the tetragonal basal structures hampers the synthesis of copper(II) complexes taking Td geometry. Namely, a counter anion and/or solvent molecule easily coordinate to the metal center to break the Td geometry. Moreover, tetrahedral distortion destabilizes copper(II) complexes through enhancement of electron acceptability. For instance, bis(2,9-dimethyl-1,10-phenanthroline)copper(II) complex

Scheme 1-1. Preparation of Tetrahedral Copper(II) Complexes through Axial Ligand Exchange Reactions.

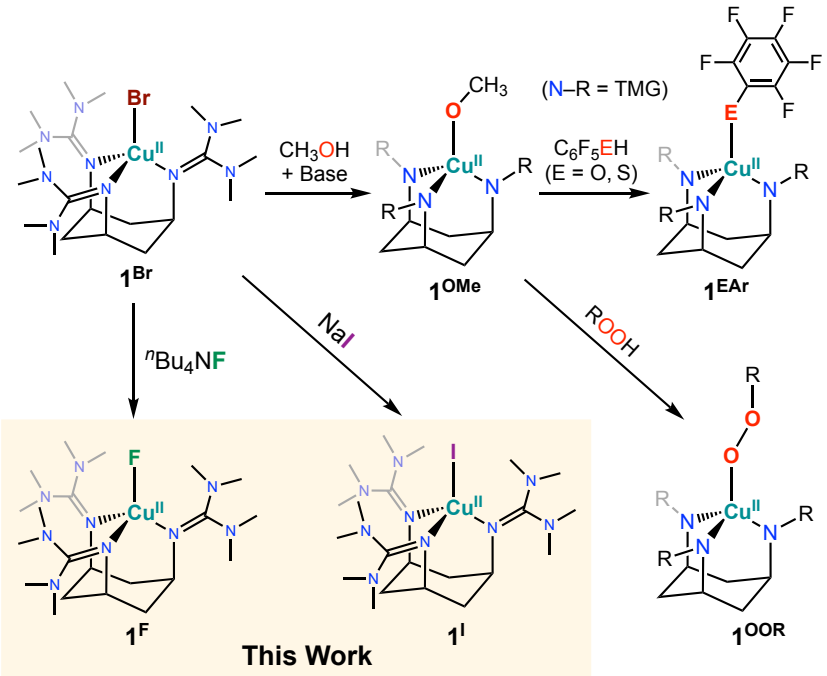

taking a Td geometry is reduced to the corresponding copper(I) complex even by residual water in solvents.[12]

To overcome such difficulties, Itoh and coworkers employed a bulky and strongly electron donating substituent TMG (*N*,*N*,*N'*,*N'*-tetra-methylguanidine) to develop a new tridentate ligand, TMG_3tach ((2,2′,2″-((1s,3s,5s)-cyclohexane-1,3,5-triyl)tris(1,1,3,3-tetra-methyl-guanidine)).[13] The TMG substituent has recently been employed in model studies of metallo-oxygenase.[14-21] By using this ligand, Itoh and coworkers have succeeded to prepare copper(II) complexes taking a tetrahedral geometry with a labile axial coordination site (Scheme 1).[13,22] For instance, copper(II)-bromide complex $\mathbf{1^{Br}}$ can be converted to a methoxide complex $\mathbf{1^{OMe}}$ by the reaction of $\mathbf{1^{Br}}$ with $^{n}Bu_4NOH$ (tetra-*n*-butylammonium hydroxide) in methanol.[13] Moreover, the reaction of $\mathbf{1^{OMe}}$ with C_6F_5OH, C_6F_5SH (C_6F_5 = pentafluorophenyl; Ar), and an alkylhydroperoxide (ROOH) gave the corresponding phenolate ($\mathbf{1^{OAr}}$), thiophenolate ($\mathbf{1^{SAr}}$), and alkylperoxide copper(II) ($\mathbf{1^{OOR}}$) complexes, respectively (Scheme 1-1).[13,22] These results clearly demonstrated that the axial coordination site in $\mathbf{1^{X}}$ is labile to undergo ligand exchange reaction with external substrates.

Scheme 1-2. C–H Bond Activation by $\mathbf{1^{X}}$

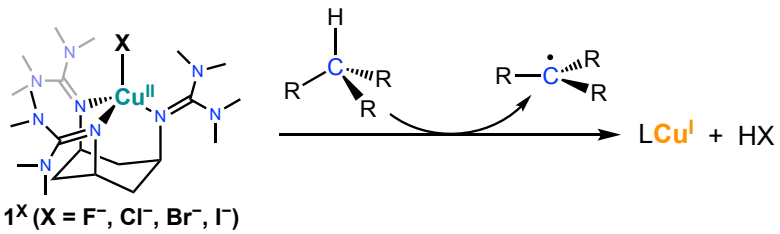

Meanwhile, halide complexes of high-valent group 10 metals such as Ni^{III} and Pd^{IV} have been demonstrated to induce aliphatic C–H bond activation, where homolytic metal-halide bond (M–X) cleavage is proposed to occur to generate halogen radical (X•) as the hydrogen atom accepter from aliphatic substrates.[23-31] Regarding to group 11 metals, however, a little is known about such reactivity of M–X complexes.[32,33] Stieber, Zhang, and coworkers recently reported the aliphatic C–H fluorination using a Cu^{III}–F complex,[34] and McDonald and coworkers reported C–H and O–H bond activation reactivity of a Au^{III}–Cl complex.[35] In this study, the author prepared Cu^{II}–F and Cu^{II}–I complexes supported by TMG_3tach ($\mathbf{1^{F}}$ and $\mathbf{1^{I}}$), and compared their physicochemical properties and C–H bond activation reactivity with those of $\mathbf{1^{Cl}}$ and $\mathbf{1^{Br}}$ (Scheme 1-2). As mentioned above, high-valent metal ions (Ni^{III}, Pd^{IV}, Cu^{III}, and Au^{III}) were used to induce the M–X bond cleavage, but the author expect that the tetrahedral Cu^{II} complex can also induce

such M–X bond cleavage even though Cu^{II} is not a high-valent metal ion, since the tetrahedral geometry is more suited for the lower Cu^{I} oxidation state.

Experimental Section

General

The reagents and solvents used in this study, except the ligand and the copper complexes, were commercial products of the highest available purity and used as received without further purification,[44] unless otherwise noted. Ligand, TMG_3tach, and its Cu(II) complexes, $\mathbf{1^{Cl}}$ and $\mathbf{1^{Br}}$, were prepared according to the reported procedures.[13] All reactions were carried out under N_2 atmosphere using standard Schlenkline or a gloveboxes (miwa DB0-1KP or KK-011-AS, KOREA KIYON product, $[O_2]<1$ ppm). UV-visible spectra were taken on a Jasco V-570 or a Hawlett Packard 8453 photo diode array spectrophotometer equipped with a Unisoku thermostated cryostat cell holder USP-203. ^{1}H-NMR spectra were recorded on a JEOL JNM-ECS400 or a JEOL ECS400 spectrometer. Electrospray ionization mass spectra (ESI-MS) measurements were performed on a microTOF II focus (Bruker Daltonics). Electron paramagnetic resonance (EPR) spectra were measured on a BRUKER EMX-micro continuous-wave X-band spectrometer, and simulated with the SpinCount program.[45] Electrochemical measurements (cyclic voltammetry) were performed at 298 K using an Automatic Polarization System HZ-7000 in deaerated acetonitrile (CH_3CN) containing $^n Bu_4NPF_6$ (tetra-*n*-butylammonium hexafluorophosphate, 0.10 mM) as a supporting electrolyte. A conventional three-electrode cell was used with a glassy carbon working electrode and a platinum wire as a counter electrode. The measured potentials were recorded with respect to $Ag/AgNO_3$ (1.0×10^{-2} M). All electrochemical measurements of the copper complexes were carried out under a nitrogen atmosphere. All redox potentials are referenced to ferrocene/ferrocenium (Fc/Fc^+) redox potential.

X-ray Structure Determination

All single crystals obtained in this study were mounted on a DT-MicroLoop (MiTegen, LLC) with mineral oil, and all X-ray data were collected at –163°C on a Rigaku R-AXIS RAPID diffractometer using filtered Mo-*K*α radiation. The structures were solved by direct method (SIR2011) and expanded using Fourier techniques.[46] Non-hydrogen atoms were refined anisotropically by full-matrix least squares on F^2. Hydrogen atoms were attached at idealized positions on carbon atoms and were not refined. All structures in the final stages of refinement showed no movement in the atom positions. The calculations were performed using Single-Crystal Structure Analysis

Software, version 4.1 (Rigaku Corporation: The Woodlands, TX). The crystallographic data of **2** are summarized in Table S1-3 and the selected bond lengths and angles are presented in the figure caption of Figure 1-5.

Theoretical Calculations

DFT calculations were performed by using Gaussian 09 (revision D.01; Gaussian, Inc.).[47] Molecular structures were optimized by using the UB3LYP functional with 6-311+G(d) basis set. For the optimized geometry, normal coordinate analyses for energy minima were performed to confirm no imaginary frequency. Electronic excitation energies and intensities were computed by the time-dependent TD-DFT calculations at the same level to its geometric optimization.[48] The first 30 excited states were calculated. Graphical outputs of the computational results were generated with the GaussView software program (ver. 5.0.8) developed by Semichem, Inc.[49]

Kinetic Measurements

Kinetic measurements for the reaction of copper(II) halide complexes $\mathbf{1^X}$ with external substrates were performed using a Hawlett Pckard 8453 photo diode array spectrophotometer equipped with a Unisoku thermostaic cryostat cell holder USP-203 (a desired temperature can be fixed within ± 0.5°C) in CH_3CN. Typically, after formation of $\mathbf{1^F}$ by the reaction of $\mathbf{1^{Br}}$ (0.25 mM) with an equimolar amount of ^{n}Bu$_4$NF·3H$_2$O at 0–25°C in CH_3CN, the reactions were initiated by injecting a substrate solution into the solution of $\mathbf{1^F}$ with use of a microsyringe at a desired temperature. The amount of the added substrates is kept more than 2.5 mM to maintain the pseudo-first-order-reaction conditions. The reactions were monitored by following decrease in absorbance at 445 nm, and the pseudo first-order rate constants (k_{obs}) of the reactions were obtained from the plot of ln(ΔA) against time (t).

Results and Discussion

Preparation of Cu^{II}-fluoride ($\mathbf{1^F}$) and Cu^{II}-iodide ($\mathbf{1^I}$) Complexes

Copper(II)-chloride ($\mathbf{1^{Cl}}$) and copper(II)-bromide ($\mathbf{1^{Br}}$) complexes were prepared according to the reported procedure by treating the ligand (TMG_3tach) and $CuCl_2$ and $CuBr_2$, respectively.[5] Copper(II)-fluoride ($\mathbf{1^F}$) and copper(II)-iodide ($\mathbf{1^I}$) complexes were prepared by a ligand exchange reaction of the axial bromide ligand $\mathbf{1^{Br}}$ with fluoride or iodide anions using tetrabutylammonium fluoride (^{n}Bu$_4$NF) and NaI, respectively.

Ligand exchange reaction of $\mathbf{1^{Br}}$ with 1 equiv. of tetrabutylammonium fluoride (^{n}Bu$_4$NF) proceeded quite efficiently to give fluoride complex $\mathbf{1^F}$ in CH_3CN at 25°C, demonstrating stronger Cu^{II}–F bond compared to the Cu^{II}–Br bond. In Figure 1-1(a) is

shown a spectral change observed upon the addition of 1 equiv. of $^{n}Bu_4NF$ to $\mathbf{1^{Br}}$ in CH_3CN, where the absorption bands at 410 nm (ε = 1,470 M^{-1} cm^{-1}) and 560 nm (1,080 M^{-1} cm^{-1}) due to $\mathbf{1^{Br}}$ (black) decreased to give new absorption bands at 350 nm (ε = 805 M^{-1} cm^{-1}) and 445 nm (520 M^{-1} cm^{-1}) together with a weak d-d band at 900 nm (100 M^{-1} cm^{-1}) (red). The ESI-MS (positive mode) of the solution showed a major peak cluster at *m/z* = 505.31, the peak position as well as the isotope distrubution pattern of which were consistent with molecular formula of mononuclear copper(II)-fluoride complex, $[Cu^{II}(TMG_3tach)(F)]^+$ ($\mathbf{1^F}$) (Figure 1-1(b)).

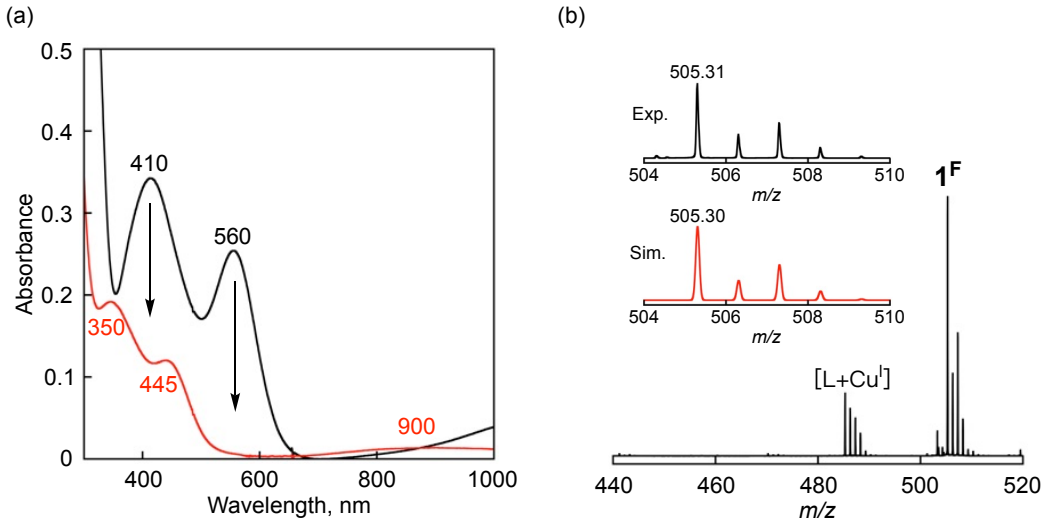

Figure 1-1. (a) UV-vis spectral change observed upon addition of $^{n}Bu_4NF$ (1 equiv.) to an CH_3CN solution of $\mathbf{1^{Br}}$ (0.25 mM, black) generating $\mathbf{1^F}$ (red) at 25°C. (b) ESI-MS of $\mathbf{1^F}$ in CH_3CN at 25°C. Inset: An expanded spectrum (black) and its simulation spectrum (red).

On the other hand, a large excess of iodide ion was required to reach quantitative formation of the iodide complex $\mathbf{1^I}$, indicating weaker Cu^{II}–I bond compared to the Cu^{II}–Br bond. Treatment of $\mathbf{1^{Br}}$ (0.12 mM) with an excess amount of NaI (500 equiv) in CH_3CN at 25°C resulted in a spectral change to give $\mathbf{1^I}$ exhibiting absorption bands at 470 nm (ε = 1,380 M^{-1} cm^{-1}) and 575 nm (1,660 M^{-1} cm^{-1}) together with a weak and broad absorption band in the near IR region (λ_{max} = 1,140 nm, ε = 200 M^{-1} cm^{-1}) (Figure S1-1). Generated complex $\mathbf{1^I}$, however, gradually decomposed to give Cu^I complexes and I_3^- (93 % based on $\mathbf{1^I}$) at 25°C (Figure S1-1 and S1-2), indicating that homolytic Cu^{II}–I bond cleavage took place at room temperature. Thus, the reaction of $\mathbf{1^{Br}}$ and NaI was conducted at a lower temperature (–40°C) to stabilize the generated $\mathbf{1^I}$ (Figure S1-3), and the equilibrium constant of the ligand exchange process was determined to be 3.9×10^2

M^{-1} by the titration experiment at –40°C shown in Figure S1-4. The formation of $\mathbf{1^I}$ was confirmed by ESI-MS, which exhibited a peak cluster at m/z = 613.18, the peak position as well as the isotope distribution pattern were consistent with the chemical formula of $(TMG_3tach)Cu^{II}I$ ($\mathbf{1^I}$) (Figure S1-5).

Physicochemical properties of copper(II)-halide complexes $\mathbf{1^X}$

EPR spectra of $\mathbf{1^X}$ were measured in acetone (Figure 1-2 and Figure S1-6). Although the EPR spectra of $\mathbf{1^{Cl}}$ and $\mathbf{1^{Br}}$ in CH_2Cl_2 have already been reported in our previous paper,[13] those in acetone were re-examined to obtain better hyperfine structures. Simulations of the spectra gave relatively large g_z values and small A_z values (Table 1-1), which are the typical spectral feature of the copper(II) complexes having a tetrahedral geometry.[36,37] It should be noted that $\mathbf{1^F}$ is a rare example of mononuclear copper(II)-fluoride complex having a tetrahedral geometry, even though single crystals suitable for X-ray crystallographic analysis has yet to be obtained despite our great efforts.

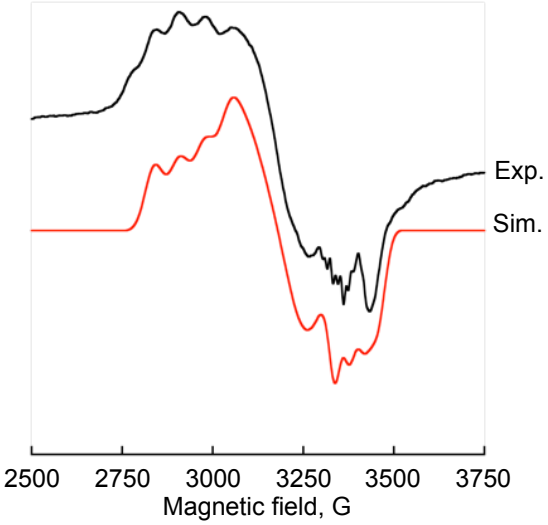

Figure 1-2. X-band EPR spectrum of $\mathbf{1^F}$ (0.5 mM) measured in acetone at 110 K (Exp. black) and its simulation spectrum (Sim. red) generated by using parameters: $g_z = 2.31$, $g_y = 2.14$, $g_x = 2.00$, $A_z = 69$ G, $A_y = 39$ G, $A_x = 39$ G. Fine structures around 3300 G are due to impurities.

Cyclic voltammetric measurements of $\mathbf{1^F}$ gave only a definitive reduction peak at –1.48 V (vs ferrocene/ferrocenium) (Figure S1-7). This is due to instability of the Cu^I complex of TMG_3tach as suggested by synthetic difficulty of the mononuclear copper(I) complex.[13] Namely, treatment of the ligand and $[Cu^I(CH_3CN)_4](OTf)$ always provided a trinuclear copper(I) complex taking a linear two-coordinate geometry at the copper(I) center.[13] In fact, $\mathbf{1^{Cl}}$, $\mathbf{1^{Br}}$, and $\mathbf{1^I}$ complexes also showed irreversible voltammograms

Table 1-1. Electronic absorption spectral data and EPR parameter of $\mathbf{1^X}$

Complex	λ/nm (ε/M^{-1} cm^{-1})			g_x, g_y, g_z (g_{iso})	A_x, A_y, A_z/G
$\mathbf{1^F}$	340 (930)	445 (620)	800 (70)	2.00, 2.14, 2.31 (2.15)	39, 39, 69
$\mathbf{1^{Cl}}$	405 (1,030)	535 (1,360)	1100 (210)	2.00, 2.11, 2.32 (2.14)	58, 33, 65
$\mathbf{1^{Br}}$	410 (1,395)	560 (1,075)	1120 (220)	2.00, 2.11, 2.32 (2.14)	61, 44, 31
$\mathbf{1^{I}}$	470 (1,200)	575 (1,420)	1140 (220)	2.04, 2.05, 2.32 (2.14)	62, 80, 18

with reduction peaks at –0.72 V, –0.67 V, and –0.59 V, respectively. Although the accurate redox potentials of $\mathbf{1^X}$ could not be determined, the systematic negative shift of the reduction peak potentials in going from iodide to fluoride is consistent with the order of the electron donor ability of halide ligands. For instance, iodide anion has the smallest electron donor ability to the copper center, thus having the smallest impact on the ligand field splitting consistent with the lowest d–d band absorption energy of $\mathbf{1^I}$ (see below).

DFT Calculation Studies for Cu^{II}-halide Complexes $\mathbf{1^X}$

The electronic structures of $\mathbf{1^X}$ were deduced by the DFT calculation performed at the UB3LYP/6-311+G(D) level of theory. Selected bond lengths and angles around the metal centers of optimized structures of $\mathbf{1^X}$ are listed in Table 1-2 together with those of $\mathbf{1^{Cl}}$ and $\mathbf{1^{Br}}$ determined by X-ray crystallographic analysis indicated in parentheses.[13] The bond lengths and angles as well as the τ_4 values[38] in the crystal strucutres of $\mathbf{1^{Cl}}$ and $\mathbf{1^{Br}}$ were well reproduced by the DFT calculation, demonstrating validity of the calculation method. As shown in Figure 1-3, $\mathbf{1^F}$ and $\mathbf{1^I}$ take slightly distorted tetrahedral geometry as in the case of $\mathbf{1^{Cl}}$ and $\mathbf{1^{Br}}$. The τ_4 value of the iodide complex was the largest (0.83) among the Cu-halide complexes, and the value decreases with decreasing of the ionic radie of the halide ligand in the order of $\mathbf{1^I} > \mathbf{1^{Br}} > \mathbf{1^{Cl}} > \mathbf{1^F}$ (Table 1-2). The major difference appears in the N2–Cu–X angle, which decreses in going from $\mathbf{1^F}$ (138.55°) to $\mathbf{1^{Cl}}$ (128.09°) to $\mathbf{1^{Br}}$ (127.11°) and to $\mathbf{1^I}$ (125.28°) as shown in Figure 1-3. The steric repulsion between the bulky TMG substituents on the nitrogen donor atoms and the halide ion decreses in the order of I > Br > Cl > F (Figure S1-8), allowing the metal center to take more favoralbe tetragonal geometry.

In Figure 1-4 is shown the electronic absorption spectrum of $\mathbf{1^F}$ (black dotted) together with the simulated spectrum obtained by TD-DFT calculation (red), and the spectral and TD-DFT data of other complexes are presented in Figure S1-9 together with the λ_{max} and ε values summarized in Table 1-1. Red shift and increase of intensity of the

Table 1-2. Bond lengths (Å), bond angles (deg), and τ_4 values of the optimized structures of $\mathbf{1}^{\mathbf{X}}$ obtained by DFT calculations at the UB3LYP/6-311+G(D) level of theory.

	$\mathbf{1}^{\mathbf{F}}$	$\mathbf{1}^{\mathbf{Cl}}$	$\mathbf{1}^{\mathbf{Br}}$	$\mathbf{1}^{\mathbf{I}}$
Cu–X	1.828	2.262 (2.259)	2.378 (2.397)	2.685
Cu–N1	2.000	1.986 (1.953)	1.987 (1.948)	1.978
Cu–N2	1.956	1.947 (1.948)	1.952 (1.945)	1.947
Cu–N3	2.070	2.052 (2.068)	2.061 (2.047)	2.030
N1–Cu–X	107.86	114.13 (114.89)	115.14 (115.56)	114.33
N2–Cu–X	138.55	128.09 (129.80)	127.11 (128.28)	125.28
N3–Cu–X	112.95	117.29 (117.01)	117.92 (116.95)	117.64
τ_4	0.77	0.81 (0.80)	0.82 (0.81)	0.83

Bond lengths, bond angles, and τ_4 values obtained from the crystal structures of $\mathbf{1}^{\mathbf{Cl}}$ and $\mathbf{1}^{\mathbf{Br}}$ are shown in the parentheses.[9]

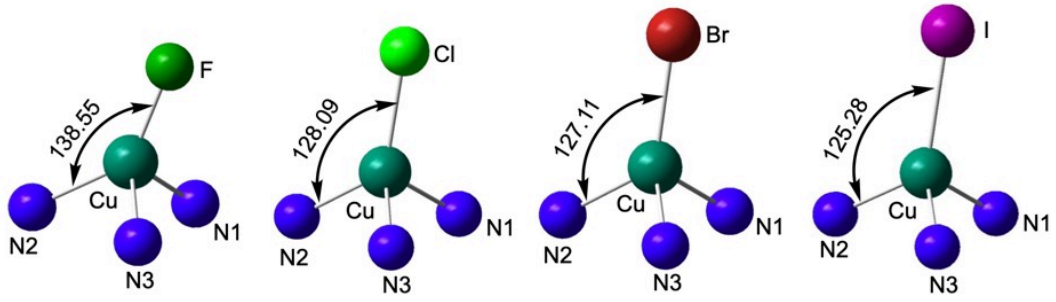

Figure 1-3. Cu centers of the optimized structures of $\mathbf{1}^{\mathbf{X}}$ by DFT calculations with UB3LYP/6-311+G(D) basis set.

absorption bands are recognized when the metal center has a better tetrahedral geometry. Natural transition orbital (NTO) analyses endorsed the assignment of three absorption bands of each complex.[39] Both the excited particles and the holes corresponding to the lowest energy absorption bands ($\mathbf{1}^{\mathbf{F}}$: 900 nm, $\mathbf{1}^{\mathbf{Cl}}$: 1100 nm , $\mathbf{1}^{\mathbf{Br}}$: 1120 nm, $\mathbf{1}^{\mathbf{I}}$: 1140 nm) are mainly localized on copper d-orbitals (Table S1-2, Figure S1-10). The differences in the absorption coefficient factors can be ascribed to the involvement of 4p orbital components into the orbitals correspond to the exited particle ($\mathbf{1}^{\mathbf{F}}$: 0.01%, $\mathbf{1}^{\mathbf{Cl}}$: 1.57%, $\mathbf{1}^{\mathbf{Br}}$:1.36%, $\mathbf{1}^{\mathbf{I}}$:0.46%), and hole ($\mathbf{1}^{\mathbf{F}}$: 3.38%, $\mathbf{1}^{\mathbf{Cl}}$: 4.56%, $\mathbf{1}^{\mathbf{Br}}$: 4.52%, $\mathbf{1}^{\mathbf{I}}$: 4.81%). As for relatively strong absorption bands in 300–600 nm, they are assigned as ligand-to-metal charge transfer (LMCT) bands (Table S1-2, Figures S1-11 and S1-12). Both absorption bands are ascribed to the CT from guanidine-moiety to the copper centerr in $\mathbf{1}^{\mathbf{F}}$. The

higher energy absorption bands involve partial CT from the halide to copper (XMCT) in $\mathbf{1}^{\mathbf{Cl}}$ (30%) and $\mathbf{1}^{\mathbf{Br}}$ (60%), and the lower energy bands are the LMCT with guanidine based orbitals. The most donating iodide ligand makes the lower energy band (575 nm) to a CT band from iodide (99%) to copper, and the higher energy band (470 nm) is a ligand based CT.

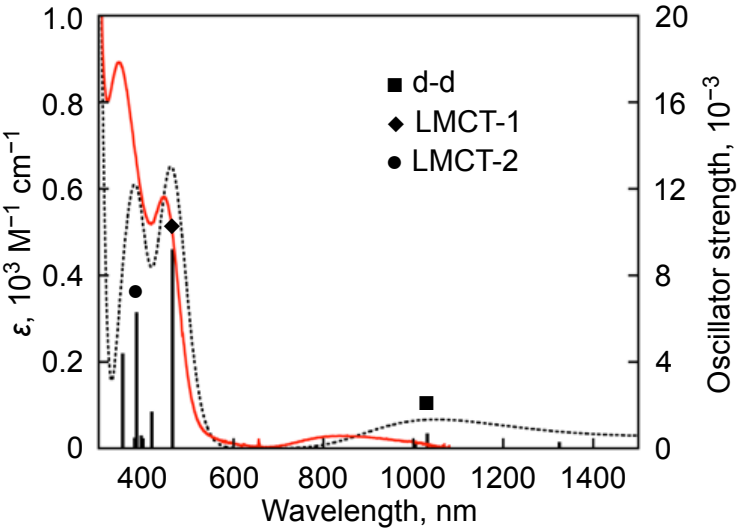

Figure 1-4. UV-vis-NIR spectrum of $\mathbf{1}^{\mathbf{F}}$ in CH_3CN measured at 25°C (red) and the calculated electronic absorption bands (bar) and a corresponding spectrum (black dotted line, peak half-width at half height is 0.2 eV).

Self-decomposition Cu^{II}-halide Complexes $\mathbf{1}^{\mathbf{X}}$

As described above, $\mathbf{1}^{\mathbf{I}}$ gradually decomposed to give the copper(I) complex and I_3^- ($I_2 + I^-$) indicating that homolytic Cu^{II}–I bond cleavage took place. $\mathbf{1}^{\mathbf{Br}}$ also underwent self-decomposition to give the copper(I) complex under anaerobic conditions, but its stability ($t_{1/2} = 5 \times 10^3$ sec at 70°C in CH_3CN, see Figure S1-13) was much higher than that of $\mathbf{1}^{\mathbf{I}}$ ($t_{1/2} = 7.9 \times 10^2$ sec at 25°C in CH_3CN, see Figure S1-1). When the self-decomposition of $\mathbf{1}^{\mathbf{Br}}$ was carried out under O_2 atmosphere, ligand hydroxylation reaction took place to give a green solid in about 50% yield. X-ray crystallographic analysis of the sample revealed that the product was a trinuclear copper(II) complex **2,** which consists of two molecules of copper(II) complex of a hydroxylated ligand that are connected by a copper(II) ion (Cu1) through hydroxide (O1 and O1') and alkoxide (O2 and O2') bridges (Figure 1-5).

The copper(II) ions ligated by the hydroxylated ligand exhibit a distorted square pyramidal geometry with three nitrogen atoms (N1, N4, N7 and N1', N4', N7') of the

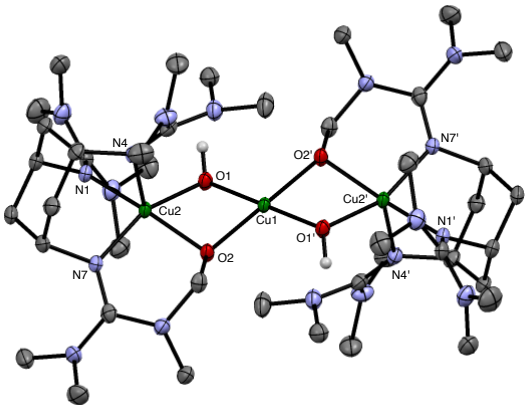

Figure 1-5. ORTEP drawing of complex **2** showing 50 % probability thermal ellipsoids. Hydrogen atoms except for those of the hydroxide bridges (O1-H and O1'-H) and THF molecules and counter anions (ClO_4) are omitted for simplicity. Selected bond lengths (Å) and angles (deg): Cu1–O1 1.902(4), Cu1–O1' 1.902(4), Cu1–O2 1.920(4), Cu1–O2 1.920(4), Cu2–O1 1.992(5), Cu2–O2 1.928(4), Cu2–N1 2.024(5), Cu2–N4 1.979(4), O1–Cu1–O1' 180.0(3), O2–Cu1–O2' 180.0(3), O1–Cu1–O2 79.28(17), O1–Cu1–O2' 100.72(17), Cu1–O1–Cu2 100.7(2), Cu1–O2–Cu2 102.42(19). The crystallographic data are presented in Table S1-3.

Scheme 1-2. Presumed Ligand Hydroxylation Pathway from $\mathbf{1}^{Br}$

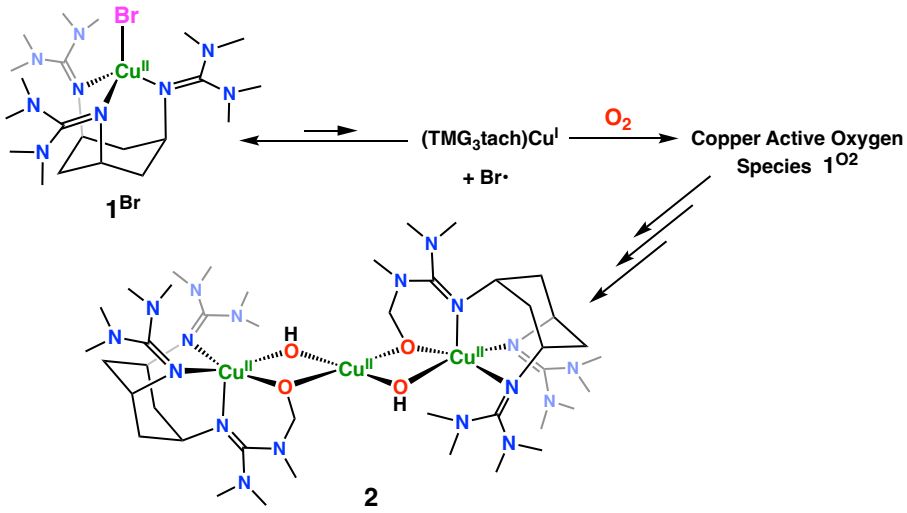

ligand and two oxygen atoms of the hydroxide (O1 and O1') and alkoxide (O2 and O2') groups, and the bridging copper(II) ion (Cu1) exhibits square planer geometry with the four oxygen atoms (O1, O1', O2, O2'). Mechanistic details of the ligand hydroxylation reaction are not clear since the reaction was too slow to perform detailed kinetic analysis. Nonetheless, it can be assumed that homolytic cleavage of the Cu^{II}–Br bond generates a

Cu^{I} complex, which may react with O_2 to generate a Cu^{II}-active oxygen speceis $\mathbf{1}^{O_2}$, from which the aliphatic ligand hydroxylation takes place (Scheme 3).[40,41] In fact, the same product was obtained by treating the isolated copper(I) complex of TMG_3tach ligand under O_2 atmosphere. Notably, $\mathbf{1}^{Cl}$ and $\mathbf{1}^{F}$ were stable at 70°C, indicating stronger Cu^{II}–Cl and Cu^{II}–F bonds compared to the Cu^{II}–I and Cu^{II}–Br bonds.

C–H Bond Activation of External Substrate

C–H bond activation reactivity of $\mathbf{1}^{X}$ was then examined by using 1,4-cyclohexadiene (CHD) as an external substrate. A typical example of the spectral change for the reaction of $\mathbf{1}^{F}$ and CHD is shown in Figure 1-6(a). Addition of an excess amount of CHD to a CH_3CN solution of $\mathbf{1}^{F}$ (0.25 mM) at 25°C resulted in quantitative formation of benzene based on $\mathbf{1}^{F}$, which was confirmed by FID-GC using a calibration curve. The reaction obeyed first-order kinetics, and the pseudo-first-order rate constant (k_{obs}) was determined from the linear plot of $\ln(A - A_\infty)$ vs. reaction time based on the absorption change at 445 nm (Figure 1-6(a), inset). The second-order rate constant (k_2) was then determined as 1.4×10^{-3} M^{-1} s^{-1} from the slope of the linear dependence of k_{obs} against the concentration of CHD (Figure 1-6(b)). Notably, this is the first example of hydrogen abstraction reaction by a copper(II)-fluoride complex. $\mathbf{1}^{Cl}$ and $\mathbf{1}^{Br}$ could also oxidize CHD, but their reaction rates were much smaller than that of $\mathbf{1}^{F}$ as shown in Figure S1-14 and Figure S1-15, respectively. Since these reactions were too slow to perform detailed kinetic analysis, the reaction rates were roughly estimated using their half-life times; 7.0×10^3 sec and 2.5×10^4 sec, respectively. On the other hand, iodide complex

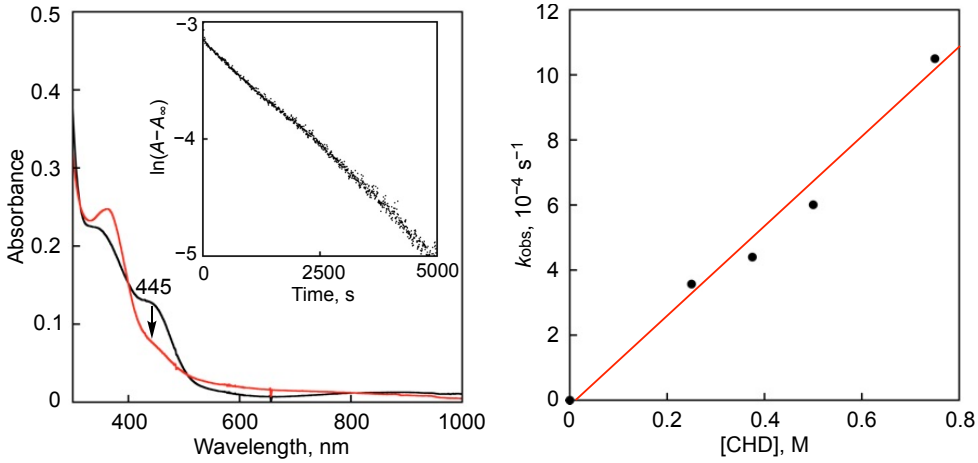

Figure 1-6. (a) UV-vis spectral change for the reaction of $\mathbf{1}^{F}$ (0.25 mM) with 1,4-cyclohexadiene (CHD, 250 mM) in CH_3CN at 25°C. Inset: A pseudo first-order plot based on the absorption change at 445 nm. (b) Plot of k_{obs} vs. [CHD] for the reaction of $\mathbf{1}^{F}$ with 1,4-cyclohexadiene (CHD).

$\mathbf{1^I}$ hardly react with CHD under the same reaction conditions. Thus, the reactivity of the halide complexes toward CHD increases in the order of $\mathbf{1^I} << \mathbf{1^{Br}} < \mathbf{1^{Cl}} < \mathbf{1^F}$. This trend seems to correlate with the order of pK_b values of X^- or bond dissociate free energy (BDFE) of H–X, but not the electron transfer reactivity of $\mathbf{1^X}$ as shown in Table S1-4.[42,43]

The reaction may proceed through a proton-coupled electron transfer (PCET) mechanism initialized by a proton transfer process, or a hydrogen atom abstraction (HAA) mechanism, which is largely influenced by the pK_b or BDFE values, respectively. Notably, in the presented system, the dissociation process of Cu–X bond should also be considered as it is involved in the rate-determining step of the oxidation reaction. Thus, the heterolytic or homolytic dissociation energy needs to be considered when studying the reaction mechanism in detail, and this point should be addressed in future studies by combining experimental data with calculations.

The reactivity tendency is the same to that of the high-valent Cu^{III}–X system showing hydrogen atom abstracting (HAA) reactivity toward 9,10-dihydroanthracene reported by Zhang and co-workers.[34] Similarly, McDonald reported a high-valent Ni^{III}–F complex showing a higher HAA reactivity than that of corresponding Ni^{III}–Cl complex.[29] Such a high HAA reactivity of the trivalent metal–halide complexes can be attributed to the proton and electron acceptability of the halide ligand and the metal center, respectively. Thus, the author thinks that $\mathbf{1^X}$ may abstract hydrogen atom from the substrate via a similar mechanism, where the HAA process is promoted by the unstable tetrahedral structure of the copper(II) oxidation state in $\mathbf{1^X}$.

Conclusion

In this chapter, the author has evaluated the strucutres, physicochemical properties, and C–H bond activation reactivity of the whole series of copper(II)-halide complexes $\mathbf{1^X}$ supported by TMG_3tach ligand, which enforces the copper(II) center to take an unusual tetrahedral geometry. Disorder of the geometry from the ideal tetrahedral one increases as the ionic size of the halide ligand decreased as $\mathbf{1^I} > \mathbf{1^{Cl}} > \mathbf{1^F} > \mathbf{1^I}$. Such a geometric effect impacts the compressed ligand field splitting of the copper center and larger participation of copper 4p orbital into the electronic absorption, thus alternating the λ_{max} and ε values of the d–d bands. Strength of the Cu^{II}–X bond increases in the order of I < Br < Cl < F to enhance the stability of the copper(II) complexes. Thus, the less stable $\mathbf{1^I}$ and $\mathbf{1^{Br}}$ easily underwent Cu^{II}–X bond homolysis to generate Cu^I complex and X•. The generated Cu^I complex reacted with O_2 to induce aliphatic ligand hydroxylation reaction through the formation of a Cu^{II}-superoxide complex. On the other hand, $\mathbf{1^F}$ induced direct C–H bond activation of the external substrate CHD. Such a reactivity can be

attributed to the basicity of F^- and unstable Cu(II) electronic state in tetrahedral geometry, resulting the higher hydrogen atom accepting ability. The unusual tetrahedral Cu^{II}–X complexes were demonstrated to possess C–H bond activation ability via two distinct pathways with and without oxygen molecule.

Reference

(1) Prigge, S. T.; Eipper, B. A.; Mains, R. E.; Amzel, L. M., *Science*, **2004**, *304*, 864-867.

(2) Solomon, E. I.; Heppner, D. E.; Johnston, E. M.; Ginsbach, J. W.; Cirera, J.; Qayyum, M.; Kieber-Emmons, M. T.; Kjaergaard, C. H.; Hadt, R. G.; Tian, L., *Chem. Rev*., **2014**, *114*, 3659-3853.

(3) Cronin, L.; Greener, B.; Foxon, S. P.; Heath, S. L.; Walton, P. H., *Inorg. Chem*., **1997**, *36*, 2594-2600.

(4) Cronin, L.; Walton, P. H., *Chem. Commun*. **2003**, 13, 1572-1573.

(5) Nairn, A. K.; Archibald, S. J.; Bhalla, R.; Boxwell, C. J.; Whitwood, A. C.; Walton, P. H., *Dalton Trans*. **2006**, *14*, 1790-1795.

(6) Kajita, Y.; Arii, H.; Saito, T.; Saito, Y.; Nagatomo, S.; Kitagawa, T.; Funahashi, Y.; Ozawa, T.; Masuda, H., *Inorg. Chem*., **2007**, *46*, 3322-3335.

(7) Cushion, M.; Ebrahimpour, P.; Haddow, M. F.; Hallett, A. J.; Mansell, S. M.; Orpen, A. G.; Wass, D. F., *Dalton Trans.*, **2009**, *9*, 1632-1635.

(8) Ebrahimpour, P.; Cushion, M.; Haddow, M. F.; Hallett, A. J.; Wass, D. F., *Dalton Trans*. **2010**, *39*, 10910-10919.

(9) Rocks, S. S.; Brennessel, W. W.; Machonkin, T. E.; Holland, P. L., *Inorg. Chem*., **2010**, *49*, 10914-10929.

(10) Matsumoto, J.; Kajita, Y.; Masuda, H., *Eur. J. Inorg. Chem*., **2012**, *26*, 4149-4158.

(11) Ebrahimpour, P.; Haddow, M. F.; Wass, D. F., *Inorg. Chem*. **2013**, *52*, 3765-3771.

(12) Itoh, S.; Kishikawa, N.; Suzuki, T.; Takagi, H. D., *Dalton Trans*. **2005**, *6*, 1066-1078.

(13) Shimizu, I.; Morimoto, Y.; Faltermeier, D.; Kerscher, M.; Paria, S.; Abe, T.; Sugimoto, H.; Fujieda, N.; Asano, K.; Suzuki, T.; Comba, P.; Itoh, S., *Inorg. Chem*. **2017**, *56*, 9634-9645.

(14) Schatz, M.; Raab, V.; Foxon, S. P.; Brehm, G.; Schneider, S.; Reiher, M.; Holthausen, M. C.; Sundermeyer, J.; Schindler, S., *Angew. Chem., Int. Ed*., **2004**, *43*, 4360-4363.

(15) Herres-Pawlis, S.; Florke, U.; Henkel, G., Eur. J. *Inorg. Chem*., **2005**, *19*, 3815-3824.

(16) Würtele, C.; Gaoutchenova, E.; Harms, K.; Holthausen, M. C.; Sundermeyer, J.; Schindler, S., *Angew. Chem., Int. Ed*. **2006**, *45*, 3867-3869.

(17) England, J.; Martinho, M.; Farquhar, E. R.; Frisch, J. R.; Bominaar, E. L.; Münck, E.; Que, L., *Angew. Chem., Int. Ed*., **2009**, *48*, 3622-3626.

(18) Herres-Pawlis, S.; Verma, P.; Haase, R.; Kang, P.; Lyons, C. T.; Wasinger, E. C.; Florke, U.; Henkel, G.; Stack, T. D. P., *J. Am. Chem. Soc*. **2009**, *131*, 1154-1169.
(19) England, J.; Guo, Y.; Van Heuvelen, K. M.; Cranswick, M. A.; Rohde, G. T.; Bominaar, E. L.; Münck, E.; Que, L., *J. Am. Chem. Soc*. **2011**, *133*, 11880-11883.
(20) Pfaff, F. F.; Heims, F.; Kundu, S.; Mebs, S.; Ray, K., *Chem. Commun*. **2012**, *48*, 3730-3732.
(21) Peterson, R. L.; Ginsbach, J. W.; Cowley, R. E.; Qayyum, M. F.; Himes, R. A.; Siegler, M. A.; Moore, C. D.; Hedman, B.; Hodgson, K. O.; Fukuzumi, S.; Solomon, E. I.; Karlin, K. D., *J. Am. Chem. Soc*., **2013**, *135*, 16454-16467.
(22) Shimizu, I.; Morimoto, Y.; Velmurugan, G.; Gupta, T.; Paria, S.; Ohta, T.; Sugimoto, H.; Ogura, T.; Comba, P.; Itoh, S., *Chem. Eur. J*. **2019**, *25*, 11157-11165.
(23) Pérez-Temprano, M. H.; Racowski, J. M.; Kampf, J. W.; Sanford, M. S., *J. Am. Chem. Soc*., **2014**, *136*, 4097-4100.
(24) Hwang, S. J.; Powers, D. C.; Maher, A. G.; Anderson, B. L.; Hadt, R. G.; Zheng, S. L.; Chen, Y. S.; Nocera, D. G., *J. Am. Chem. Soc*., **2015**, *137*, 6472-6475.
(25) Hwang, S. J.; Anderson, B. L.; Powers, D. C.; Maher, A. G.; Hadt, R. G.; Nocera, D. G., *Organometallics*, **2015**, *34*, 4766-4774.
(26) Shields, B. J.; Doyle, A. G., *J. Am. Chem. Soc*. **2016**, *138*, 12719-12722.
(27) Mondal, P.; Pirovano, P.; Das, A.; Farquhar, E. R.; McDonald, A. R., *J. Am. Chem. Soc*., **2018**, *140*, 1834-1841.
(28) Mondal, P.; Lovisari, M.; Twamley, B.; McDonald, A. R., *Angew. Chem., Int. Ed*., **2020**, *59*, 13044-13050.
(29) Mondal, P.; McDonald, A. R., *Chem. Eur. J*. **2020**, *26*, 10083-10089.
(30) Gygi, D.; Gonzalez, M. I.; Hwang, S. J.; Xia, K. T.; Qin, Y.; Johnson, E. J.; Gygi, F.; Chen, Y. S.; Nocera, D. G., *J. Am. Chem. Soc*., **2021**, *143*, 6060-6064.
(31) Kariofillis, S. K.; Doyle, A. G., *Acc. Chem. Res*., **2021**, *54*, 988-1000.
(32) Kochi, J. K., *J. Am. Chem. Soc*., **1955**, *77*, 5274-5278.
(33) Castro, C. E.; Gaughan, E. J.; Owsley, D. C., *J. Org. Chem*. **1965**, *30*, 587-592.
(34) Bower, J. K.; Cypcar, A. D.; Henriquez, B.; Stieber, S. C. E.; Zhang, S., *J. Am. Chem. Soc*., **2020**, *142*, 8514-8521.
(35) Lovisari, M.; Gericke, R.; Twamley, B.; McDonald, A. R., *Inorg. Chem*., **2021**, *60*, 15610-15616.
(36) Sakaguchi, U.; Addison, A. W., *Dalton Trans*., **1979**, *4*, 600-608.
(37) Yokoi, H.; Addison, A. W., *Inorg. Chem*., **1977**, *16*, 1341-1349.
(38) Yang, L.; Powell, D. R.; Houser, R. P., *Dalton Trans*., **2007**, *9*, 955-964.
(39) Martin, R. L., *J. Chem. Phys*., **2003**, *118*, 4775-4777.

(40) Kunishita, A.; Kubo, M.; Sugimoto, H.; Ogura, T.; Sato, K.; Takui, T.; Itoh, S., *J. Am. Chem. Soc*., **2009**, *131*, 2788-2789.
(41) Kunishita, A.; Ertem, M. Z.; Okubo, Y.; Tano, T.; Sugimoto, H.; Ohkubo, K.; Fujieda, N.; Fukuzumi, S.; Cramer, C. J.; Itoh, S., *Inorg. Chem*., **2012**, *51*, 9465-9480.
(42) Bordwell, F. G., *Acc. Chem. Res*., **1988**, *21*, 456-463.
(43) Luo, Y. R. *Comprehensive Handbook of Chemical Bond Energies*. CRC Press, Boca Raton, FL, **2007**.
(44) Armarego, W. L. F. *Purification of Laboratory Chemicals*. Elsevier Science, **2017**.
(45) Petasis, D. T.; Hendrich, M. P., *Electron Paramagnetic Resonance Investigations of Biological Systems by Using Spin Labels, Spin Probes, and Intrinsic Metal Ions, Pt A*, Qin, P. Z., Warncke, K., Ed.; **2015**; Vol. 563, pp 171-208.
(46) Burla, M. C.; Caliandro, R.; Camalli, M.; Carrozzini, B.; Cascarano, G. L.; Giacovazzo, C.; Mallamo, M.; Mazzone, A.; Polidori, G.; Spagna, R., *J. Appl. Cryst*., **2012**, *45*, 357-361.
(47) Frisch, M. J.; Trucks, G. W.; Schlegel, H. B.; Scuseria, G. E.; Robb, M. A.; Cheeseman, J. R.; Scalmani, G.; Barone, V.; Mennucci, B.; Petersson, G. A.; Nakatsuji, H.; Caricato, M.; Li, X.; Hratchian, H. P.; Izmaylov, A. F.; Bloino, J.; Zheng, G.; Sonnenberg, J. L.; Hada, M.; Ehara, M.; Toyota, K.; Fukuda, R.; Hasegawa, J.; Ishida, M.; Nakajima, T.; Honda, Y.; Kitao, O.; Nakai, H.; Vreven, T.; Montgomery, J., J. A.; Peralta, J. E.; Ogliaro, F.; Bearpark, M.; Heyd, J. J.; Brothers, E.; Kudin, K. N.; Staroverov, V. N.; Kobayashi, R.; Normand, J.; Raghavachari, K.; Rendell, A.; Burant, J. C.; Iyengar, S. S.; Tomasi, J.; Cossi, M.; Rega, N.; Millam, J. M.; Klene, M.; Knox, J. E.; Cross, J. B.; Bakken, V.; Adamo, C.; Jaramillo, J.; Gomperts, R.; Stratmann, R. E.; Yazyev, O.; Austin, A. J.; Cammi, R.; Pomelli, C.; Ochterski, J. W.; Martin, R. L.; Morokuma, K.; Zakrzewski, V. G.; Voth, G. A.; Salvador, P.; Dannenberg, J. J.; Dapprich, S.; Daniels, A. D.; Farkas, O.; Foresman, J. B.; Ortiz, J. V.; Cioslowski, J.; Fox, D. J. *Gaussian 09*, Gaussian, Inc.: Wallingford CT, **2009**.
(48) Casida, M. E. *In Recent Advances in Computational Chemistry*; Chong, D. P., Ed.; World Scientific: New York, **1995**; Vol. 1, pp 155-192.
(49) Dennington, I., R.; Keith, T.; Millam, J.; Eppinnett, K.; Hovell, W. L.; Gilliland, R. *GaussView, Semichem, Shawnee Mission*, KS. **2003**.

Supporting Information

Table S1-1. Summary of the copper components of the d-d transitions of $\mathbf{1^X}$ using natural transition orbital (NTO) calculations showing with 4p orbital contribution in parenthesis.

	$\mathbf{1^F}$	$\mathbf{1^{Cl}}$	$\mathbf{1^{Br}}$	$\mathbf{1^I}$
Particle	Cu 70.2% (0.01%)	Cu 71.5% (1.57%)	Cu 66.4% (1.36%)	Cu 64.2% (0.46%)
Hole	Cu 71.6% (3.38%)	Cu 71.0% (4.56%)	Cu 70.9% (4.52%)	Cu 66.2% (4.81%)
Oscillation Strength	0.0007	0.0012	0.0017	0.0027

Table S1-2. Summary of the main components of the ligand to metal charge transfer (LMCT) transitions of $\mathbf{1^X}$ using natural transition orbital (NTO) calculations.

		$\mathbf{1^F}$		$\mathbf{1^{Cl}}$		$\mathbf{1^{Br}}$		$\mathbf{1^I}$	
LMCT-1	Particle	F	0.2%	Cl	0.3%	Br	1.7%	X	69.0%
		Cu	0.6%	Cu	0.6%	Cu	0.7%	Cu	15.7%
		L	99.2%	L	99.1%	L	97.6%	L	15.3%
	Hole	F	4.4%	Cl	4.6%	Br	5.7%	I	4.4%
		Cu	66.5%	Cu	66.2%	Cu	65.1%	Cu	62.1%
		L	29.0%	L	29.2%	L	29.2%	L	33.4%
LMCT-2	Particle	F	2.7%	Cl	30.1%	Br	59.5%	I	0.6%
		Cu	4.4%	Cu	10.1%	Cu	7.6%	Cu	0.4%
		L	92.9%	L	59.8%	L	32.8%	L	99.1%
	Hole	F	4.4%	Cl	4.6%	Br	5.7%	I	4.4%
		Cu	66.1%	Cu	66.5%	Cu	65.1%	Cu	61.8%
		L	29.4%	L	28.9%	L	29.2%	L	33.9%

Table S1-3. Crystallographic data for **2**.

	2•2THF
formula	$C_{50}H_{104}Cl_2Cu_3N_{18}O_{14}$
fw	1443.06
crystal description	blue, plate
crystal size, mm	0.10 × 0.07 × 0.06
crystal system	monoclinic
space group	$P2_1/c$ (#14)
a, Å	11.8018(7)
b, Å	27.9068(13)
c, Å	10.1974(6)
α, deg	90
β, deg	94.144(2)
γ, deg	90
V, Å^3	3349.7(4)
Z	2
D_{calced}, g cm^{-3}	1.494
μ, cm^{-1}	1.095
T, K	110
$2\theta_{max}$, deg	55.0
total reflns	27062
unique reflns (R_{int})	7643(0.1012)
no. of params	394
$R1$ [$I > 2\sigma(I)$]^a	0.0802
$wR2$ (all data)^b	0.2094
GOF	1.170
max./min. $\Delta\rho$, e Å^{-3}	0.87/-0.80

^{a} $R1 = \Sigma(|F_o| - |F_c|)/\Sigma|F_o|$. ^{b} $wR2 = (\Sigma(w(F_o^2 - F_c^2)^2)/\Sigma w(F_o^2)^2)^{1/2}$.

Table S1-4. The pK_b values of X^- in DMSO, BDFE of H–X, and half-life time ($t_{1/2}$) of the reactions between $\mathbf{1^X}$ (0.25 mM) and CHD (250 mM)

$\mathbf{1^X}$	$t_{1/2}$ / 10^3 sec	pK_b of X^- in DMSO	BDFE of H–X /kcal/mol
$\mathbf{1^F}$	1.8	15	135
$\mathbf{1^{Cl}}$	7.0	1.8	103
$\mathbf{1^{Br}}$	25	0.9	87

Table S1-5. Coordinate of optimized structure of $\mathbf{1^F}$.

	X	Y	Z
F	-0.14674	-0.51650	2.02061
Cu	-0.03560	0.04566	0.28516
N	-1.45992	-0.89519	-0.75689
N	-3.01301	-2.69204	-0.94083
N	-3.14618	-1.18402	0.82895
N	-0.19094	1.71077	-0.72914
N	-0.89758	3.98552	-0.78186
N	0.20035	3.12521	1.08455
N	1.68924	-0.59639	-0.66255
N	4.04852	-0.90936	-0.85575
N	2.87310	-1.84343	0.91838
C	-1.13483	-0.85039	-2.19352
C	-1.27864	0.60470	-2.69510
C	-0.16265	1.54156	-2.18981
C	1.21267	0.97578	-2.59945
C	1.46911	-0.47001	-2.11749
C	0.28163	-1.37410	-2.54553
C	-2.49497	-1.57745	-0.30891
C	-2.16225	-3.72397	-1.51778
C	-4.44677	-2.95843	-1.00131
C	-3.55698	-2.15316	1.84571
C	-3.05768	0.18760	1.31830
C	-0.30256	2.90173	-0.16999
C	-2.12878	3.87545	-1.55392
C	-0.35281	5.33589	-0.66666
C	-0.49548	3.95964	2.06322
C	1.29364	2.32590	1.63266
C	2.83345	-1.08915	-0.21950
C	4.42657	0.35224	-1.47566
C	5.05053	-1.96812	-0.93771
C	3.94750	-1.72165	1.89979
C	1.74218	-2.67156	1.33763
H	-1.86148	-1.45694	-2.74618
H	-1.23806	0.59784	-3.79245
H	-2.26599	0.98458	-2.41393
H	-0.27583	2.51648	-2.67534
H	1.26352	0.97862	-3.69665
H	1.99740	1.64914	-2.24301
H	2.35464	-0.84356	-2.64642
H	0.43563	-2.37582	-2.13332
H	0.32068	-1.47175	-3.63917
H	-1.12638	-3.55469	-1.22396
H	-2.47179	-4.70581	-1.13623
H	-2.22354	-3.75353	-2.61402
H	-2.93915	-2.02260	2.74296
H	-4.60943	-2.01149	2.11807
H	-3.41867	-3.16944	1.47808
H	-4.73100	-3.82780	-0.39294
H	-5.00019	-2.08705	-0.65013
H	-4.73587	-3.16302	-2.04003
H	-4.00967	0.44984	1.79426
H	-2.24342	0.29008	2.04378
H	-2.88258	0.86087	0.47797
H	-2.56124	2.88332	-1.42549
H	-2.85210	4.61662	-1.18990
H	-1.96769	4.05872	-2.62451
H	0.62444	5.30313	-0.18400
H	-0.23216	5.76597	-1.66886
H	-1.01272	5.99744	-0.08993
H	-1.42485	4.34189	1.64139
H	-0.73669	3.35805	2.94830
H	0.12743	4.80467	2.38078
H	1.85796	1.87655	0.81411
H	1.95905	2.98417	2.20326
H	0.92684	1.52959	2.29143
H	3.75097	1.14173	-1.14577
H	5.44489	0.61716	-1.16375
H	4.41132	0.30617	-2.57315
H	4.62586	-2.90853	-0.58523
H	5.36167	-2.09648	-1.98226
H	5.94437	-1.73686	-0.34285
H	4.49815	-2.66402	2.01424
H	4.64455	-0.93825	1.60051
H	3.52034	-1.45425	2.87410
H	1.10542	-2.15277	2.05825
H	1.13848	-2.91755	0.46214
H	2.13774	-3.59867	1.76906

Table S1-6. Coordinate of optimized structure of $\mathbf{1}^{Cl}$.

	X	Y	Z
Cl	-0.16422	-0.30403	2.52126
Cu	-0.03146	0.02571	0.28758
N	-1.44511	-0.90107	-0.75520
N	-2.95546	-2.73197	-0.90607
N	-3.21168	-1.12721	0.75853
N	-0.18411	1.70251	-0.69020
N	-0.96505	3.94828	-0.69464
N	0.33807	3.15477	1.06381
N	1.67077	-0.62030	-0.65961
N	4.03404	-0.91342	-0.81473
N	2.83019	-1.92086	0.89892
C	-1.12636	-0.85357	-2.19486
C	-1.27871	0.60624	-2.67914
C	-0.16919	1.54002	-2.15437
C	1.20798	0.98538	-2.57703
C	1.46912	-0.46692	-2.11546
C	0.28794	-1.36665	-2.56577
C	-2.50025	-1.57068	-0.31832
C	-2.05082	-3.74699	-1.42935
C	-4.37696	-3.04908	-1.01423
C	-3.70562	-2.03452	1.79400
C	-3.30656	0.28821	1.09780
C	-0.27433	2.89948	-0.13036
C	-2.22607	3.77238	-1.40365
C	-0.48484	5.32628	-0.61750
C	-0.28646	3.96696	2.10622
C	1.60583	2.53829	1.44611
C	2.80968	-1.12609	-0.21258
C	4.40846	0.36623	-1.40010
C	5.05103	-1.95782	-0.90756
C	3.89082	-1.84464	1.89985
C	1.74621	-2.84212	1.22649
H	-1.85618	-1.46009	-2.74423
H	-1.23031	0.61580	-3.77615
H	-2.26990	0.97702	-2.40079
H	-0.28926	2.52165	-2.62596
H	1.25581	1.00127	-3.67426
H	1.99261	1.65634	-2.21604
H	2.36191	-0.82720	-2.64156
H	0.44627	-2.37877	-2.18179
H	0.32317	-1.43552	-3.66171
H	-1.03470	-3.54274	-1.09229
H	-2.35138	-4.73047	-1.04660
H	-2.06189	-3.79284	-2.52651
H	-3.24084	-1.76924	2.75052
H	-4.79545	-1.96482	1.89774
H	-3.43474	-3.06244	1.55361
H	-4.65968	-3.89422	-0.37295
H	-4.97346	-2.17979	-0.73627
H	-4.61113	-3.31622	-2.05230
H	-4.35243	0.52574	1.33035
H	-2.68139	0.53102	1.96308
H	-2.98388	0.88714	0.24659
H	-2.61177	2.76833	-1.22994
H	-2.95764	4.49572	-1.02234
H	-2.12259	3.93341	-2.48483
H	0.52807	5.34629	-0.21474
H	-0.46779	5.76084	-1.62461
H	-1.13159	5.95019	0.01279
H	-1.29423	4.25448	1.80574
H	-0.35221	3.37465	3.02613
H	0.29750	4.87221	2.31496
H	2.00884	1.98138	0.60054
H	2.31409	3.32754	1.73088
H	1.47403	1.85206	2.28812
H	3.71801	1.14070	-1.06641
H	5.41754	0.63482	-1.06316
H	4.41396	0.34208	-2.49816
H	4.63122	-2.91472	-0.59635
H	5.38562	-2.04756	-1.94867
H	5.92808	-1.73476	-0.28583
H	4.46416	-2.77901	1.95595
H	4.57015	-1.02437	1.66599
H	3.44088	-1.65593	2.88155
H	1.20127	-2.51723	2.11691
H	1.04872	-2.89126	0.39029
H	2.17061	-3.83979	1.40166

Table S1-7. Coordinate of optimized structure of $\mathbf{1^{Br}}$.

	X	Y	Z
Br	-0.17017	-0.27943	2.65918
Cu	-0.03461	0.02362	0.30429
N	-1.43997	-0.90543	-0.74865
N	-2.94389	-2.74011	-0.89723
N	-3.22325	-1.12036	0.74901
N	-0.18632	1.70389	-0.67775
N	-0.97539	3.94643	-0.68405
N	0.35899	3.17068	1.05824
N	1.66873	-0.62810	-0.65598
N	4.03333	-0.91320	-0.80957
N	2.82843	-1.94497	0.88875
C	-1.12345	-0.85576	-2.18887
C	-1.28039	0.60469	-2.66899
C	-0.17303	1.53947	-2.14221
C	1.20528	0.98835	-2.56594
C	1.46916	-0.46553	-2.11084
C	0.29003	-1.36522	-2.56506
C	-2.49957	-1.57202	-0.31576
C	-2.02913	-3.75208	-1.40874
C	-4.36282	-3.06362	-1.02023
C	-3.73649	-2.01776	1.78340
C	-3.34358	0.29906	1.06226
C	-0.27200	2.90422	-0.12357
C	-2.24101	3.75976	-1.38182
C	-0.50285	5.32774	-0.61903
C	-0.25331	3.98228	2.10803
C	1.64540	2.57834	1.41424
C	2.80803	-1.13606	-0.21307
C	4.40417	0.37287	-1.38288
C	5.05441	-1.95284	-0.91039
C	3.88479	-1.87742	1.89463
C	1.75027	-2.87900	1.19607
H	-1.85385	-1.46272	-2.73714
H	-1.23247	0.61762	-3.76600
H	-2.27241	0.97210	-2.38916
H	-0.29519	2.52107	-2.61363
H	1.25387	1.00867	-3.66310
H	1.98853	1.65926	-2.20193
H	2.36299	-0.82104	-2.63864
H	0.45052	-2.37906	-2.18664
H	0.32323	-1.42829	-3.66144
H	-1.01779	-3.54177	-1.06123
H	-2.32949	-4.73595	-1.02707
H	-2.02824	-3.80014	-2.50585
H	-3.29352	-1.73867	2.74623
H	-4.82871	-1.95224	1.86253
H	-3.45522	-3.04703	1.56131
H	-4.64932	-3.90632	-0.37751
H	-4.96626	-2.19534	-0.75438
H	-4.58374	-3.33743	-2.05945
H	-4.40043	0.53406	1.24313
H	-2.75906	0.55709	1.95107
H	-2.98267	0.88698	0.21912
H	-2.61957	2.75462	-1.19946
H	-2.97335	4.48136	-0.99881
H	-2.14678	3.91513	-2.46468
H	0.51459	5.35600	-0.22845
H	-0.50063	5.75759	-1.62828
H	-1.14605	5.95041	0.01606
H	-1.26701	4.26390	1.82223
H	-0.30242	3.39064	3.02946
H	0.32928	4.89091	2.30576
H	2.02242	1.99642	0.57372
H	2.35632	3.38161	1.64992
H	1.54721	1.91742	2.28052
H	3.71018	1.14172	-1.04375
H	5.41161	0.64219	-1.04166
H	4.41180	0.35833	-2.48109
H	4.63760	-2.91435	-0.60955
H	5.39164	-2.03109	-1.95158
H	5.92924	-1.73260	-0.28455
H	4.46086	-2.81063	1.94216
H	4.56236	-1.05234	1.67296
H	3.43011	-1.70090	2.87642
H	1.20954	-2.57950	2.09815
H	1.04779	-2.90549	0.36319
H	2.17769	-3.88019	1.34244

Table S1-8. Coordinate of optimized structure of **1**[I].

	X	Y	Z
I	-0.17222	-0.30641	2.95527
Cu	-0.01978	0.00249	0.29231
N	-1.44711	-0.92211	-0.71855
N	-2.95236	-2.75182	-0.88561
N	-3.27320	-1.11240	0.73329
N	-0.19137	1.69517	-0.65532
N	-0.97890	3.93637	-0.66597
N	0.39836	3.18105	1.05206
N	1.67635	-0.62112	-0.63283
N	4.04130	-0.87979	-0.79261
N	2.84938	-1.96342	0.88244
C	-1.12543	-0.87071	-2.15991
C	-1.29068	0.58825	-2.64221
C	-0.18632	1.52877	-2.12080
C	1.19280	0.98498	-2.55098
C	1.46699	-0.46456	-2.08936
C	0.29106	-1.37345	-2.53482
C	-2.52465	-1.57799	-0.30550
C	-2.02245	-3.76613	-1.36500
C	-4.36717	-3.07229	-1.05845
C	-3.86664	-1.99655	1.73627
C	-3.41312	0.31139	1.01776
C	-0.26031	2.90274	-0.11065
C	-2.25614	3.73882	-1.33936
C	-0.50546	5.31889	-0.63393
C	-0.17194	4.02969	2.09663
C	1.70808	2.61716	1.36642
C	2.82220	-1.13114	-0.20001
C	4.39058	0.41925	-1.35142
C	5.07720	-1.90317	-0.91623
C	3.91596	-1.92602	1.88009
C	1.80311	-2.94704	1.14352
H	-1.85063	-1.48267	-2.70907
H	-1.24562	0.59929	-3.73937
H	-2.28361	0.95201	-2.36087
H	-0.31614	2.50936	-2.59190
H	1.23456	0.99869	-3.64850
H	1.97459	1.66237	-2.19624
H	2.36130	-0.81747	-2.61762
H	0.45703	-2.38494	-2.15230
H	0.32272	-1.44146	-3.63088
H	-1.02206	-3.55357	-0.98832
H	-2.33441	-4.74790	-0.98778
H	-1.98926	-3.81883	-2.46138
H	-3.51112	-1.69354	2.72725
H	-4.96238	-1.94268	1.72123
H	-3.55530	-3.02602	1.56035
H	-4.68074	-3.90713	-0.41857
H	-4.97786	-2.19945	-0.82615
H	-4.54885	-3.35579	-2.10259
H	-4.48024	0.55828	1.09391
H	-2.91745	0.57442	1.95749
H	-2.96374	0.88781	0.21063
H	-2.62927	2.73534	-1.13842
H	-2.98279	4.46389	-0.95246
H	-2.18049	3.88134	-2.42544
H	0.52128	5.35422	-0.26921
H	-0.52780	5.73215	-1.64980
H	-1.13362	5.95112	0.00641
H	-1.20104	4.28996	1.84820
H	-0.17153	3.47357	3.04086
H	0.40939	4.95063	2.23176
H	2.02667	1.96161	0.55707
H	2.43457	3.43258	1.48700
H	1.66913	2.03410	2.29096
H	3.68894	1.17404	-0.99739
H	5.39664	0.69657	-1.01339
H	4.39055	0.41778	-2.44958
H	4.67405	-2.87760	-0.63960
H	5.41522	-1.95117	-1.95878
H	5.94800	-1.68505	-0.28460
H	4.51400	-2.84649	1.87242
H	4.57084	-1.07364	1.69699
H	3.46584	-1.81275	2.87288
H	1.29760	-2.74385	2.09154
H	1.06593	-2.91527	0.34180
H	2.25393	-3.94825	1.18373

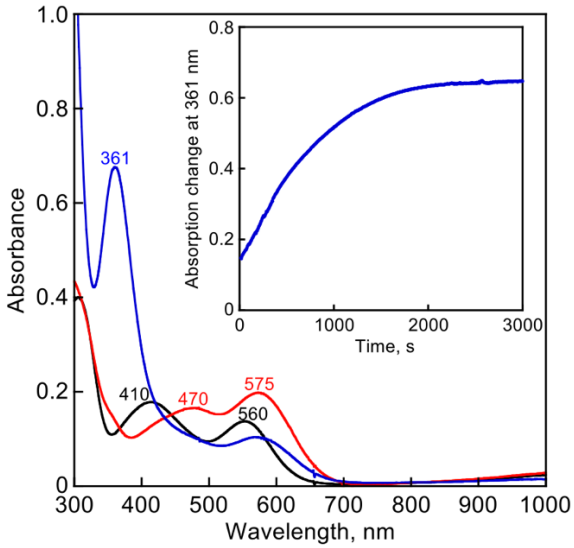

Figure S1-1. UV-vis spectral changes observed upon addition of an CH_3CN solution containing NaI (500 eq in the final solution) to an CH_3CN solution of $[Cu^{II}(TMG_3tach)(Br)](OTf)$ ($\mathbf{1^{Br}}$, 0.12 mM, black) at room temperature giving a spectrum of $\mathbf{1^{I}}$ (red), and following decomposition reaction of $\mathbf{1^{I}}$ giving I_3^- (blue). Inset: Time course of the absorption change at 361 nm due to the formation of I_3^-. The yield of I_3^- was 93% based on $\mathbf{1^{I}}$, which was deduced by using the ε value (25,000 M^{-1} cm^{-1}) of I_3^- at 361 nm.

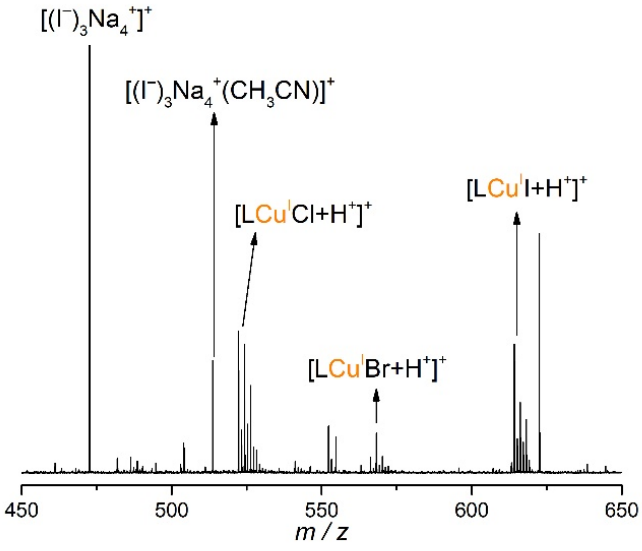

Figure S1-2. ESI-MS (positive mode) of the solution after decomposition of $\mathbf{1^{I}}$ at 25 ºC in CH_3CN.

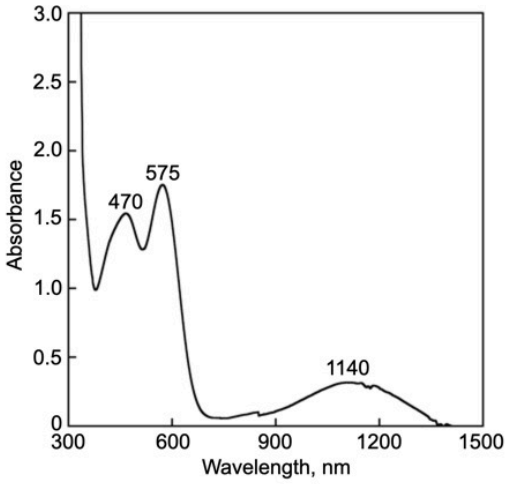

Figure S1-3. UV-vis-NIR spectrum of $\mathbf{1}^{\mathbf{I}}$ (1.2 mM) in CH_3CN measured at –40°C.

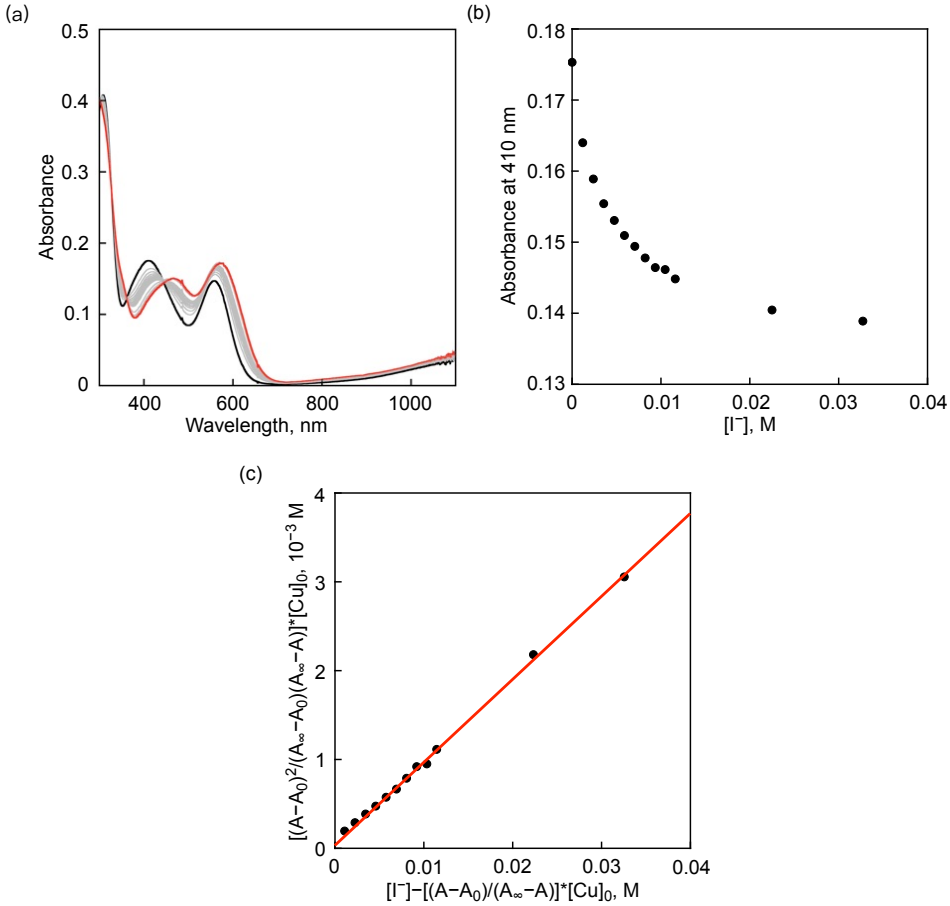

Figure S1-4. (a) UV-vis spectral changes observed upon addition of a CH_3CN solution containing NaI to a CH_3CN solution of $\mathbf{1}^{\mathbf{Br}}$ (0.12 mM) at −40°C. (b) Titration plot based on the absorption change (ΔA) at 410 nm. (c) Plot of $[(A-A_0)^2/(A_\infty-A_0)(A_\infty-A)]*[Cu]_0$ vs. $[I^-]-[(A-A_0)/(A_\infty-A)]*[Cu]_0$, from which the equilibrium constant was determined as 0.093.

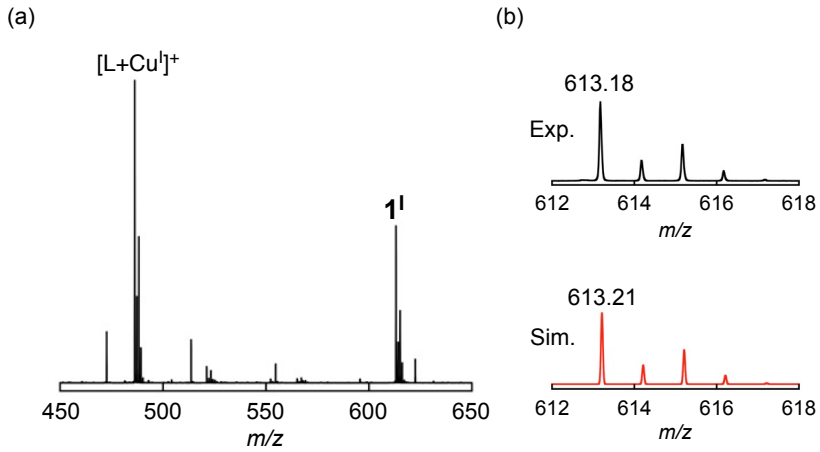

Figure S1-5. (a) ESI-MS of $\mathbf{1}^{\mathbf{I}}$ in CH_3CN. (b) An expanded spectrum (Exp., black) and its simulation spectrum (Sim., red).

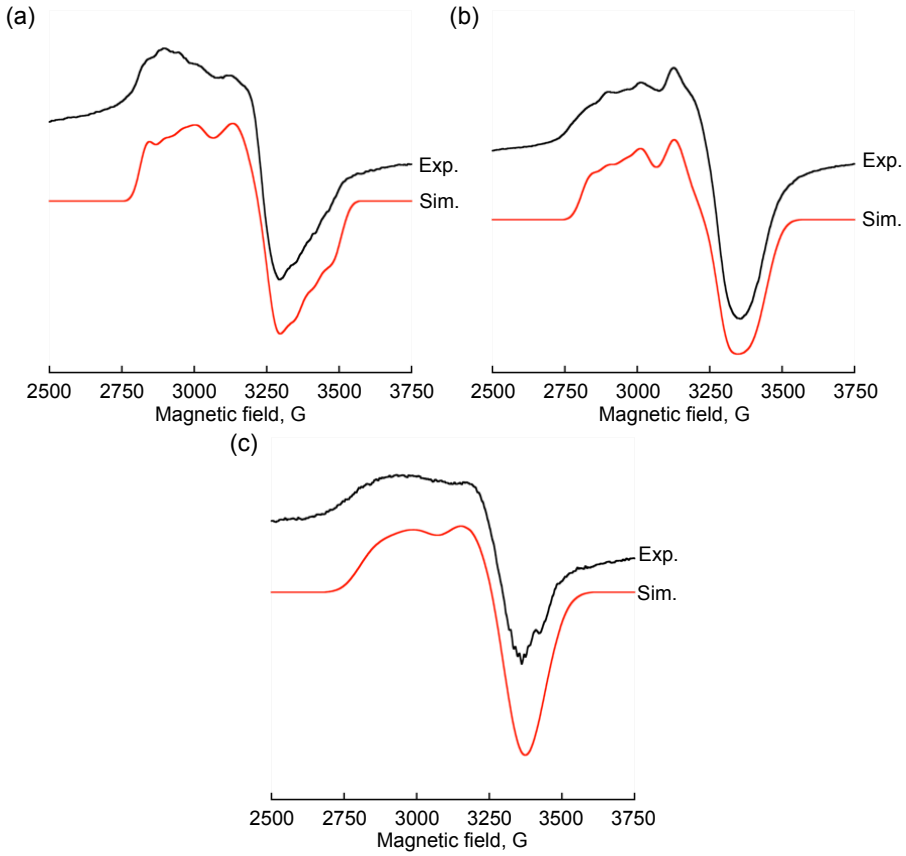

Figure S1-6. X-band EPR spectrum of $\mathbf{1}^{\mathbf{X}}$ measured in acetone at 110 K (Exp: black) and its simulation spectra (Sim: red) generated by using parameters; (a) $\mathbf{1}^{\mathbf{Cl}}$ (0.5 mM), $g_z = 2.32$, $g_y = 2.11$, $g_x = 2.00$, $A_z = 58$ G, $A_y = 33$ G, $A_x = 65$ G; (b) $\mathbf{1}^{\mathbf{Br}}$ (0.5 mM), $g_z = 2.32$, $g_y = 2.11$, $g_x = 2.00$, $A_z = 61$ G, $A_y = 44$ G, $A_x = 31$ G and (c) $\mathbf{1}^{\mathbf{I}}$ (0.5 mM) $g_z = 2.32$, $g_y = 2.05$, $g_x = 2.04$, $A_z = 62$ G, $A_y = 80$ G, $A_x = 18$ G.

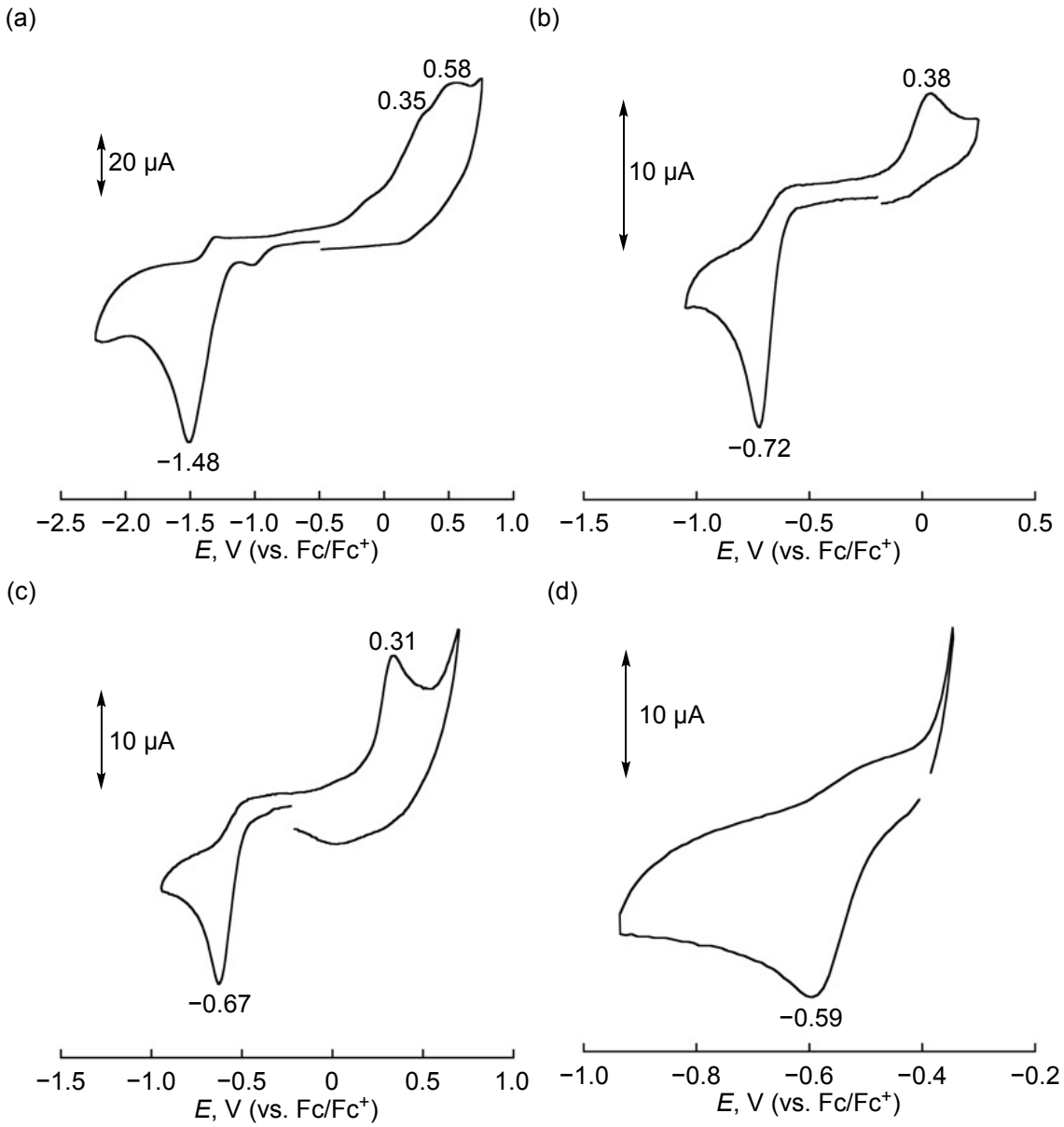

Figure S1-7. Cyclic voltammograms for $\mathbf{1^X}$ ((a) X = F, (b) X = Cl, (c) X = Br, (d) X = I) measured in an CH_3CN solution containing 0.10 M of $TBAPF_6$. Grassy carbon is employed as a working electrode and the scan rate is 100 mV s^{-1}. The voltammogram was measured against $Ag/AgNO_3$ reference electrode, and the potential was converted to the value based on ferrocene/ferrocenium.

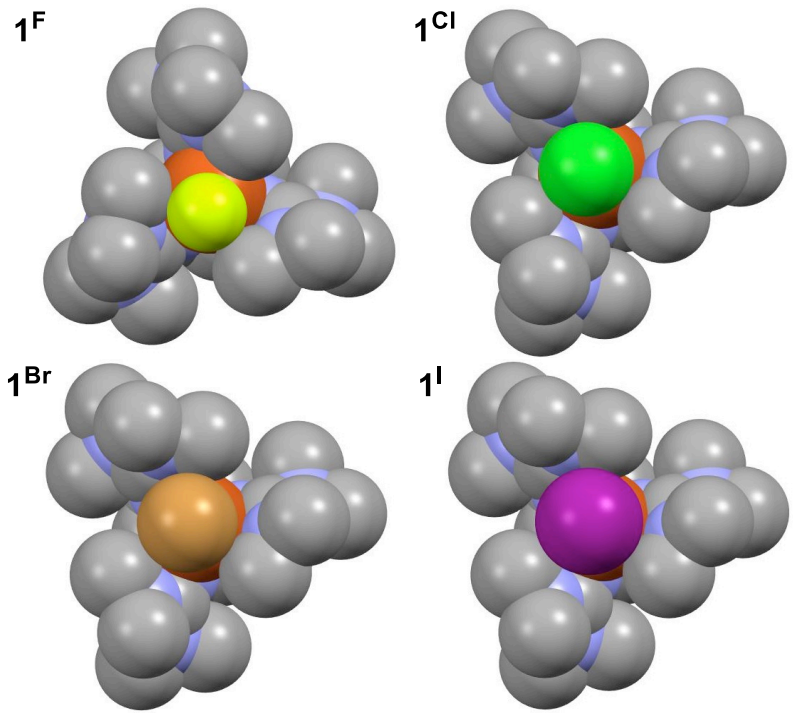

Figure S1-8. Space-filling modes of $\mathbf{1^X}$ ($X = F^-$, Cl^-, Br^-, I^-) (C: grey; N: blue; Cu: red; halide: colored by atom) showing steric repulsion between the TMG substituents and the halide ion may decrease in the order of I > Br > Cl > F.

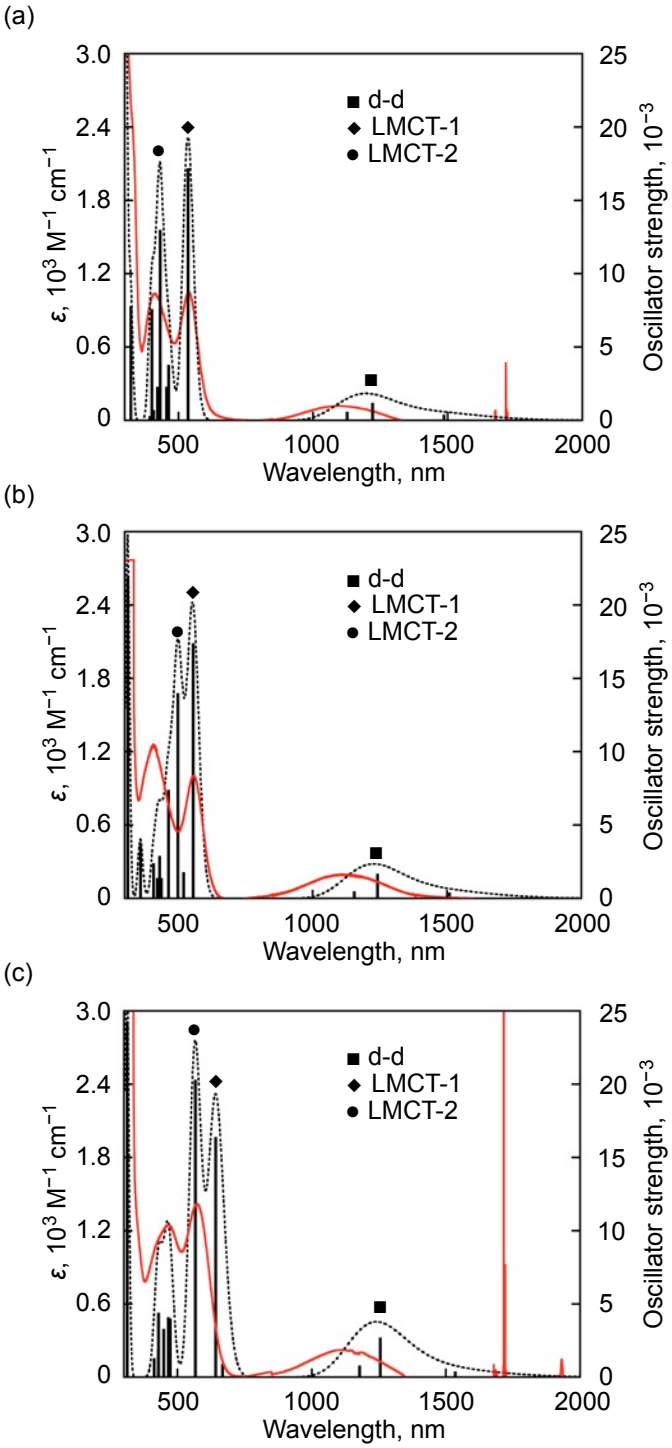

Figure S1-9. UV-vis-NIR spectra of of $\mathbf{1^X}$ in CH_3CN measured at –40°C and calculated UV-vis-NIR (a) $\mathbf{1^{Cl}}$, (b) $\mathbf{1^{Br}}$, and (c) $\mathbf{1^{I}}$.

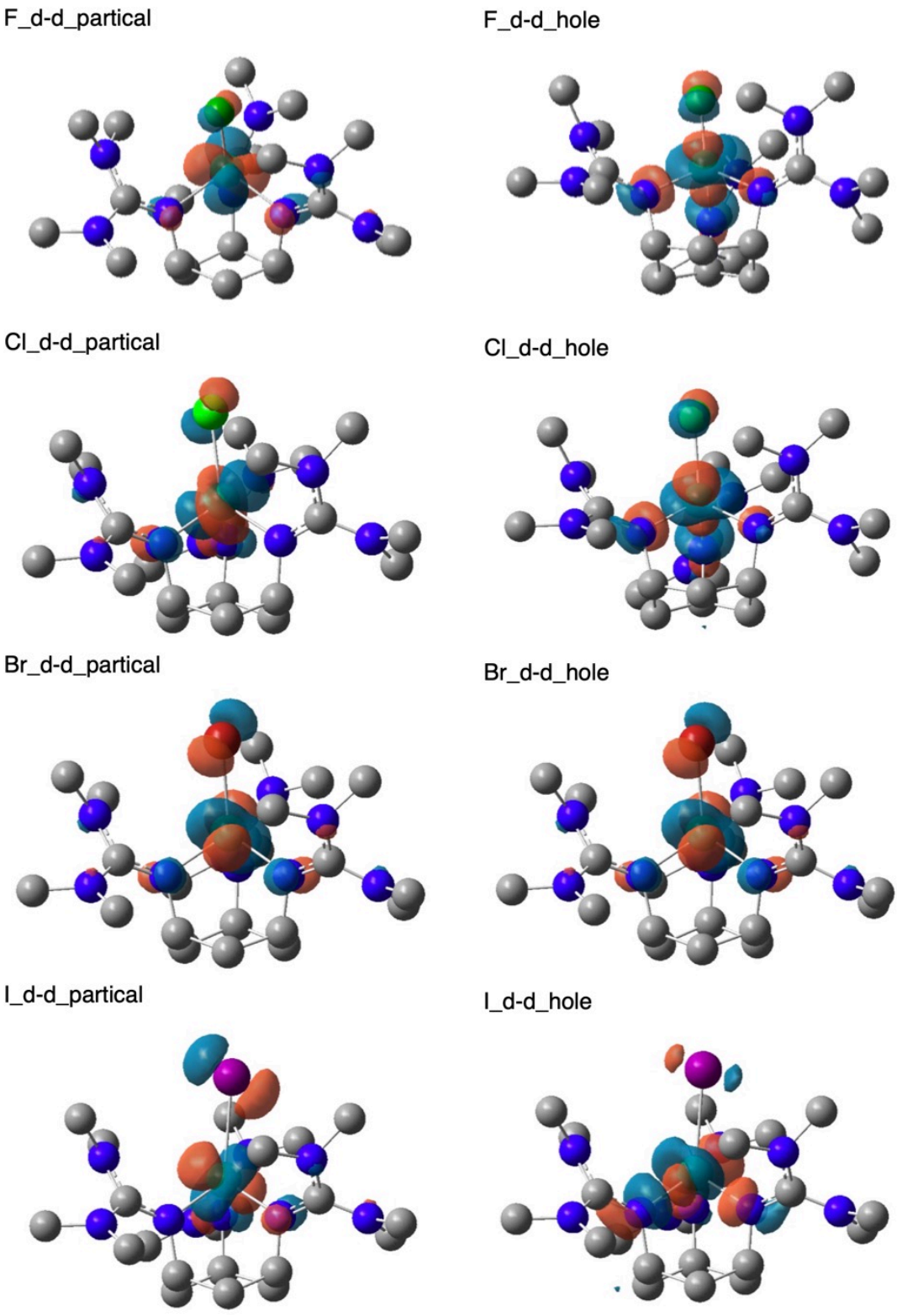

Figure S1-10. Natural transition orbitals of $\mathbf{1^X}$ calculated with UB3LYP/6-311+G(D) basis set relating to their d-d transitions.

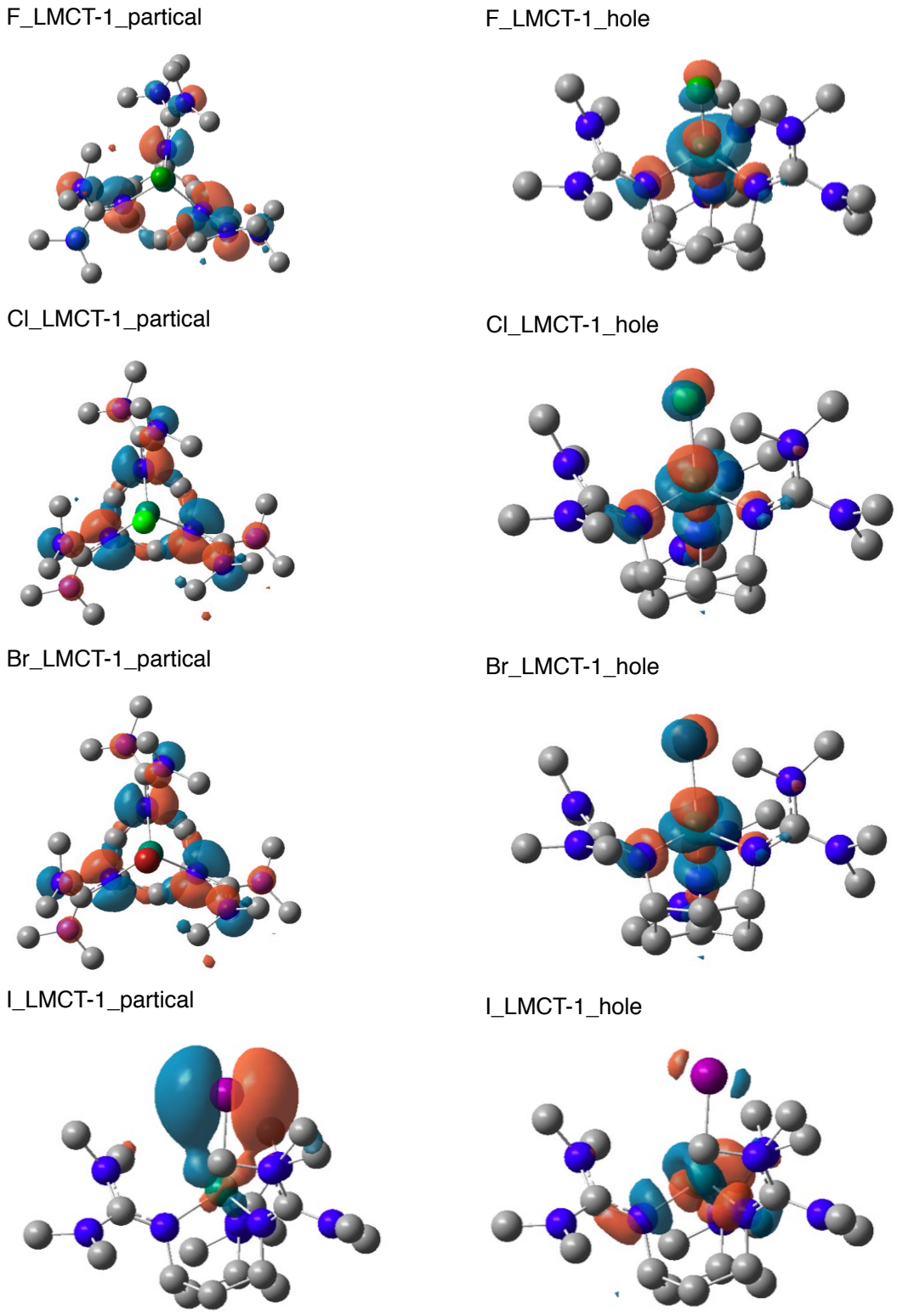

Figure S1-11. Natural transition orbitals of $\mathbf{1}^{\mathbf{X}}$ calculated with UB3LYP/6-311+G(D) basis set relating to their LMCT-1 transitions.

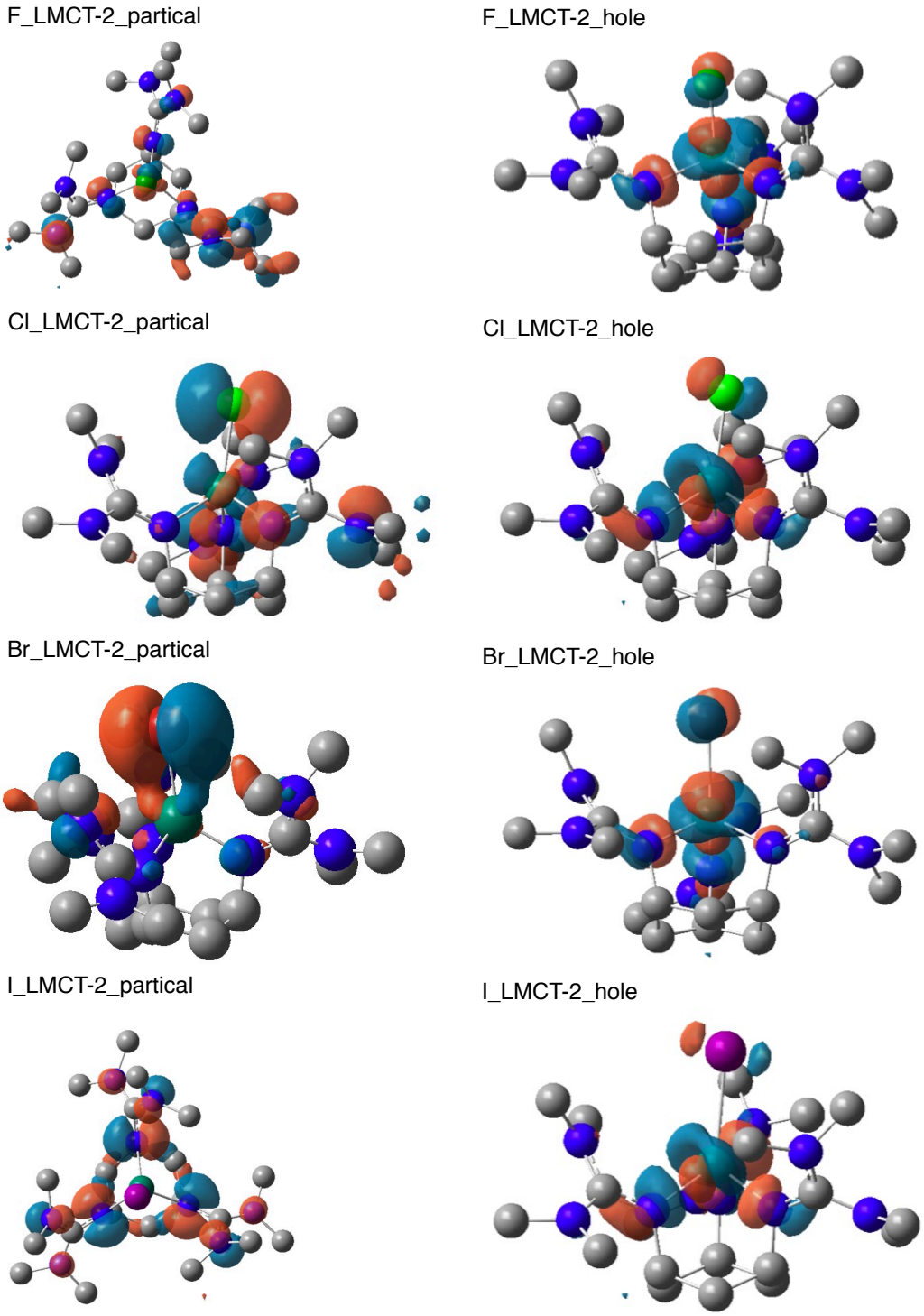

Figure S1-12. Natural transition orbitals of $\mathbf{1}^{X}$ calculated with UB3LYP/6-311+G(D) basis set relating to their LMCT-2 transitions.

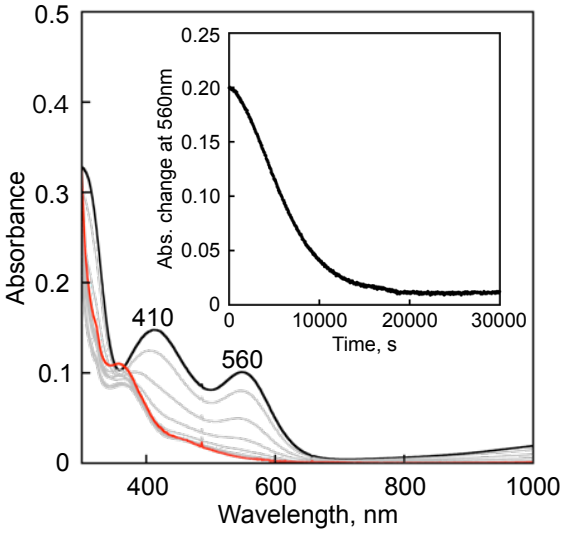

Figure S1-13. UV-vis spectral change observed upon heating an CH_3CN solution of $\mathbf{1}^{Br}$ (0.25 mM, black line) at 70°C under anaerobic condition giving a spectrum of a decomposed complex exhibiting no d-d band above 600 nm (red line).

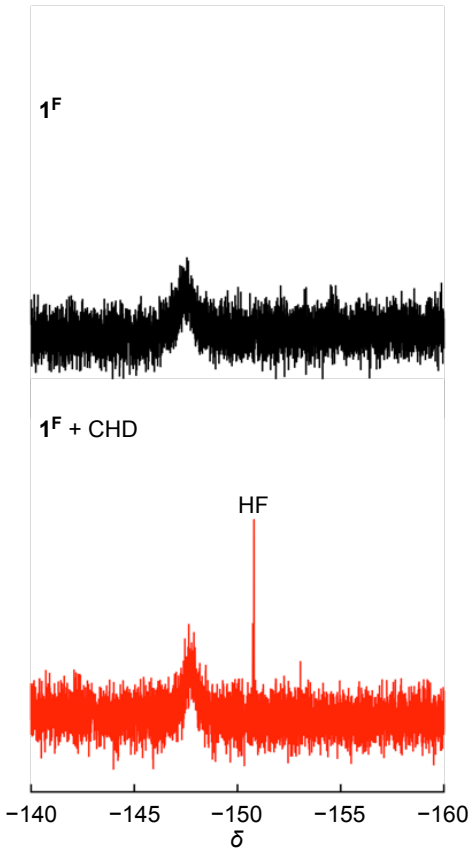

Figure S1-14. ^{19}F NMR spectra of $\mathbf{1}^{F}$ (above) and after the reaction with CHD (below) in CH_3CN.

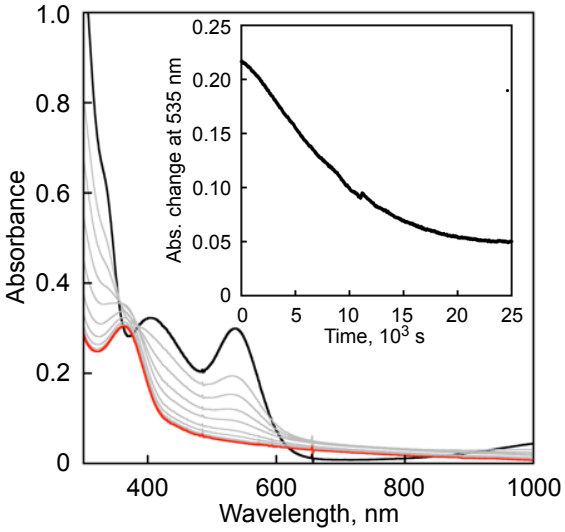

Figure S1-15. UV-vis specrtral change for the reaction of $\mathbf{1}^{Cl}$ (0.25 mM) with 1,4-cyclohexadiene (CHD, 250 mM) in CH_3CN at 25°C. Inset: Absorbance change at 535 nm.

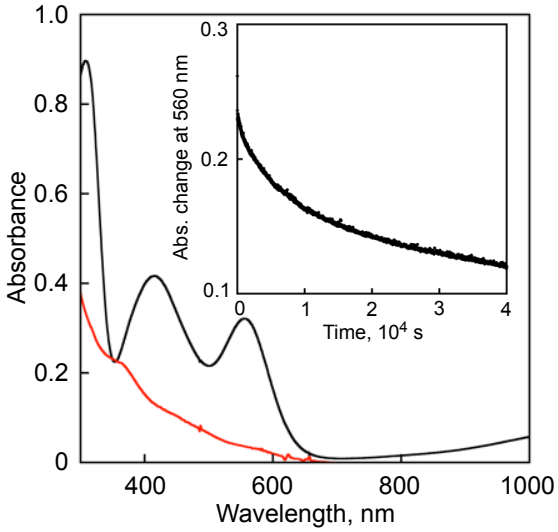

Figure S1-16. UV-vis specrtral change for the reaction of $\mathbf{1}^{Br}$ (0.25 mM) with 1,4-cyclohexadiene (CHD, 250 mM) in CH_3CN at 25°C. Inset: Absorbance change at 535 nm.

Chapter 2. Oxidation Mechanism of Phenols by Copper(II)-halide Complexes

Introduction

Redox reactivity of transition-metal complexes depends largely on the geometry of metal center. In the case of copper(II) complexes with similar donor groups, for example, oxidation ability of copper(II) complexes taking a tetrahedral (Td) geometry may be higher than those having a square planar, square pyramidal, or trigonal bipyramidal structure, since the Td geometry is more suited to copper(I) oxidation state compared to the others. To explore the redox reactivity of such tetrahedral copper(II) complexes, Itoh and coworkers have developed a series of copper(II) complexes, $[Cu^{II}(TMG_3tach)X]^+$ ($\mathbf{1}^{\mathbf{X}}$), where TMG_3tach is an N_3-tridentate ligand consisting of *cis,cis*-1,3,5-triamino-cyclohexane (tach) and *N*,*N*,*N*′,*N*′-tetramethylguanidino (TMG) substituents and X is an anionic co-ligand (F^-, Cl^-, Br^-, I^-, MeO^-, $C_6F_5O^-$, $C_6F_5S^-$, and ROO^-).[1-3] Reactivity study of the halide complexes have demonstrated that they undergo Cu^{II}–X cleavage, and in the case of X = F^-, Cl^-, and Br^-, they induce C–H bond activation of an external substrate such as 1,4-cyclohexadiene (CHD) having a weak C–H bond (76.0 ± 1.2 kcal/mol)[4] to give the corresponding copper(I) complex and benzene as the oxidation product.[3] Such C–H bond activation reactivity of transition-metal halide complexes has been reported by using high-valent transition metal halide complexes of Ni^{III}, Pd^{IV}, Cu^{III}, and Au^{III}, where the higher oxidation state of metal ions induces homolytic cleavage of the metal–halide bond.[5-14] In the case of $\mathbf{1}^{\mathbf{X}}$, on the other hand, metal center has a normal Cu^{II} oxidation state, but not a high-valent metal ion such as Cu^{III}. Thus, the author suspected that such a reactivity of the halide complexes can be attributed to their tetrahedrally distorted geometry, which induces the Cu^{II}–X bond homolysis to give Cu^{I} and X•, the latter of which formally abstracts hydrogen atom from the substrate.[3] Unfortunately, however, the oxidation reaction of CHD by $\mathbf{1}^{\mathbf{X}}$ was too slow to perform detailed kinetic analysis.

In this chapter, the author has further examined the reactivity of $\mathbf{1}^{\mathbf{X}}$ (X = F^-, Cl^-, Br^-, and I^-) toward phenolic substrates (4-substituted-2,6-di-*tert*-butylphenol $\mathbf{P}^{\mathbf{Y}}$H, Scheme

Scheme 2-1. Reaction of copper(II) complexes and 4-substituted-2,6-di-*tert*-butylphenol ($\mathbf{P}^{\mathbf{Y}}$H)

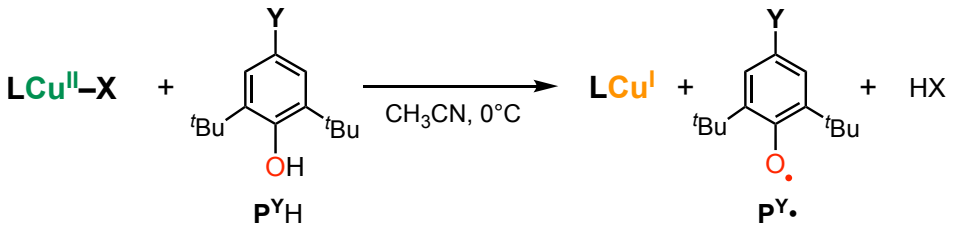

P^YH P^Y•

2-1) in order to shed light on the O–H bond activation mechanism by copper(II)-halide complexes. Phenols are often used as a mechanistic probe for the hydrogen atom transfer reactions. To examine the geometric effect on the reactivity of copper(II)-halide complexes, the author also employed copper(II)-halide complexes $\mathbf{3^X}$ (X = Cl^- or Br^-) supported by tripodal tetradentate ligand TMG_3tren (1,1,1-tris(2-(N^2-(1,1,3,3-tetramethylguanidino))ethyl)amine),[15-17] that enforces trigonal bipyramidal (Tbp) geometry of the metal center (Figure 2-1).

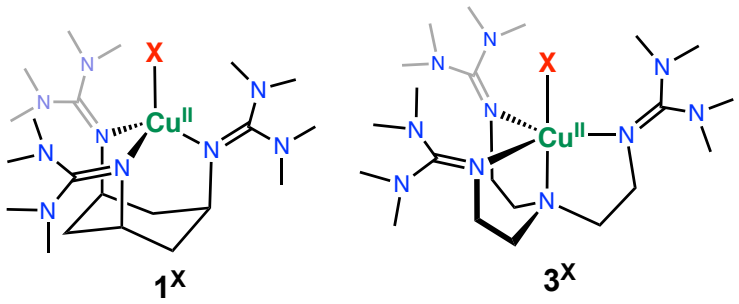

Figure 2-1. ChemDraw structures of $\mathbf{1^X}$ and $\mathbf{3^X}$.

Experimental Section

General

The reagents and solvents used in this study, except the ligand and the copper complexes, were commercial products of the highest available purity and used as received without further purification, unless otherwise noted. Ligand, TMG_3tach, and its Cu(II) complexes, $\mathbf{1^{Cl}}$ and $\mathbf{1^{Br}}$, were prepared according to the reported procedures.[13] All reactions were carried out under N_2 atmosphere using standard Schlenkline or a gloveboxes (miwa DB0-1KP or KK-011-AS, KOREA KIYON product, [O_2]<1 ppm). UV-visible spectra were taken on a Jasco V-570 or a Hawlett Packard 8453 photo diode array spectrophotometer equipped with a Unisoku thermostated cryostat cell holder USP-203. ^{1}H-NMR spectra were recorded on a JEOL JNM-ECS400 or a JEOL ECS400 spectrometer. Electrospray ionization mass spectra (ESI-MS) measurements were performed on a microTOF II focus (Bruker Daltonics). Electron paramagnetic resonance (EPR) spectra were measured on a BRUKER EMX-micro continuous-wave X-band spectrometer, and simulated with the SpinCount program.

Kinetic Measurements

Kinetic measurements for the reaction of copper(II) halide complexes $\mathbf{1^X}$ with external substrates were performed using a Hawlett Pckard 8453 photo diode array spectrophotometer equipped with a Unisoku thermostaic cryostat cell holder USP-203 (a desired temperature can be fixed within ± 0.5°C) in CH_3CN. Typically, the reactions were initiated by injecting a substrate solution into the solution of $\mathbf{1^{Br}}$ with

use of a microsyringe at a desired temperature. The amount of the added substrates is kept more than 2.5 mM to maintain the pseudo-first-order-reaction conditions. The reactions were monitored by following decrease in absorbance at 420 nm, and the pseudo-first-order-rate constants (k_{obs}) of the reactions were obtained from the plot of ln(ΔA) aginst time (t).

Results and Discussion

Reactivity study of copper(II)-bromide complex $\mathbf{1^{Br}}$ with 4-substituted-2,6-di-*tert*-butylphenol ($\mathbf{P^{Y}H}$)

In Figure 2-2(a) is shown the spectral changes observed upon addition of $P^{tBu}H$ (Y = *tert*-butyl, 12.5 mM) to $\mathbf{1^{Br}}$ (0.25 mM) in CH_3CN at 0 °C under N_2 atmosphere as a typical example, where the absorption bands at 410 and 560 nm due to $\mathbf{1^{Br}}$ gradually decreases with concomitant increase of the absorption bands at 380, 400 and 626 nm, obeying first-order kinetics (see the first-order plot shown in the inset of Figure 2-2(a)). The absorption bands of the post-reaction solution at 380, 400 and 626 nm are identical to those of 2,4,6-tri-*tert*-butylphenoxyl radical (P^{tBu}•), and its quantitative formation based on $\mathbf{1^{Br}}$ was confirmed using the reported ε values of P^{tBu}•.[18] Formation of the phenoxyl radical P^{tBu}• and the copper(I) complex was further confirmed by the EPR spectrum shown in Figure S2-1, where only an EPR signal ascribable to P^{tBu}• was observed at g = 2.0041[19] but the EPR signals due to the copper(II) complex $\mathbf{1^{Br}}$ completely disappeared. The fate of generated HBr will be discussed below.

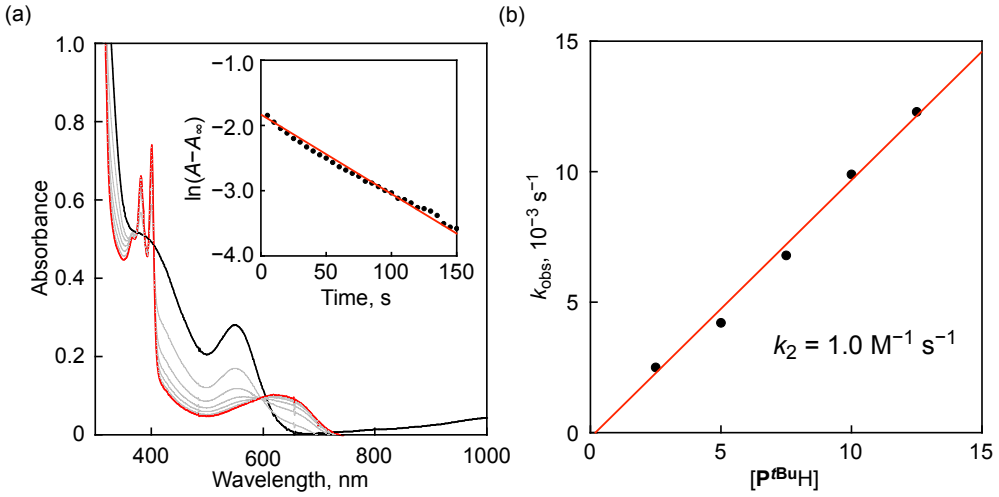

Figure 2-2. (a) UV-vis spectral changes for the reaction of $\mathbf{1^{Br}}$ (0.25 mM) with $P^{tBu}H$ (12.5 mM) in CH_3CN at 0°C. Inset: A pseudo first-order plot based on the absorption change at 410 nm. (b) Plot of k_{obs} vs. substrate concentration.

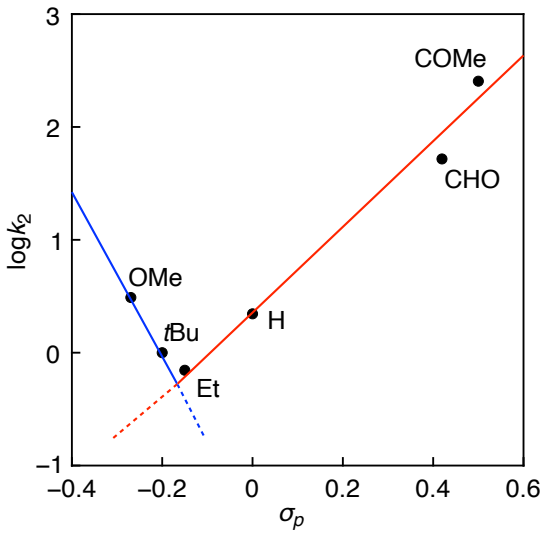

Figure 2-3. Hammett plot for the reaction of $\mathbf{1^{Br}}$ and $P^{Y}H$.

In Figure 2-3 is shown a Hammett plot of logk_2 against σ_p. As clearly seen, the reaction rate (k_2) increases linearly as the electron-withdrawing (EW) ability of the *p*-substituent Y increases (increasing the σ_p value) in going from Y = Et to COMe with a Hammett ρ value of 4.0. In the case of Y = OMe and *t*Bu, however, the data points deviated from the linear line, where the reaction rates were larger than those expected from the linear correlation. Such a phenomenon was also observed in the reactions of phenol derivatives with copper(III)-superoxide (Cu^{III}–OO•) and nickel(III)-fluoride (Ni^{III}–F) complexes supported by 2,6-diamidepyridine ligands.[10,21] The author suggested a change of reaction mechanism across the series of phenol derivatives. Namely, the reactions with the phenols having an electron-withdrawing (EW) substituent involve a PTET (proton transfer following electron transfer) mechanism, whereas the oxidation of phenols having an electron-donating (ED) substituent contains hydrogen atom transfer (HAT) or concerted proton/electron transfer (CPET) mechanism. Kinetic deuterium isotope effects (KIEs) were determined to be 1.6 and 1.7 for the oxidation of $P^{OMe}H(D)$ and $P^{tBu}H(D)$, respectively (Figure S2-8 and S2-9). Such a small KIE value was reported in the oxidation of $P^{H}H$ by Ni^{III}–Cl complex supported by the 2,6-diamidepyridine ligand, for which CPET mechanism was proposed.[9] On the other hand, no kinetic deuterium isotope effect was observed (KIE = 1.0) in the oxidation of $P^{COMe}H(D)$ having an EW-substituent by $\mathbf{1^{Br}}$ (Figure S2-10).

To explain these kinetic results, the author proposes a reaction mechanism illustrated in Scheme 2-2.

With phenol substrates having an EW-substituent such as $P^{COMe}H$, deprotonation of the phenol substrate by one of the TMG substituents of the supporting ligand takes place making an acid-base equilibrium (initial PT process in Scheme 2-2a). Then, electron transfer from generated phenolate to copper(II) ion occurs concomitant with

Scheme 2-2. Proposed mechanism for the phenol oxidation by $\mathbf{1}^{Br}$

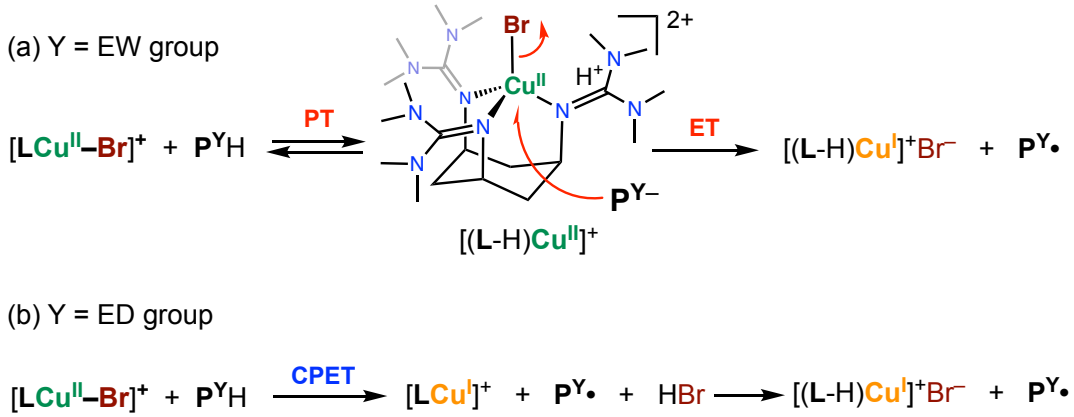

dissociation of Br^-, giving copper(I) complex and the phenoxyl radical product P^{COMe}•. Dissociated Br^- forms a guanidinium salt with the protonated TMG substituent (Scheme 2-2a). Thus, reductive dissociation process of Br^- from Cu^{II}–Br center is rate-limiting. This mechanism is consistent with the fact that no KIE was observed as mentioned above.

On the other hand, the reaction of phenols having ED-substituent like $P^{OMe}H$, such a proton transfer from the phenol hardly occurs due to the higher pK_a of phenolic proton of $P^{OMe}H$, so that concerted proton/electron transfer (CPET) becomes the major pathway (Scheme 2-2b). In this case as well, generated HBr eventually forms the guanidinium salt with the TMG substituent of the supporting ligand (Scheme 2-2b).

Axial ligand effect of copper(II)-halide toward phenol oxidation

To get further insight into the reaction mechanism, effects of the halide ligands X were examined using $P^{COMe}H$ having an EW-substituent as the substrates under the same reaction conditions. In Figures S2-12–S2-14 are shown the kinetic analysis data for the reactions of $\mathbf{1}^{F}$, $\mathbf{1}^{Cl}$, and $\mathbf{1}^{I}$, respectively. The k_2 values for these reactions were determined in the presence of a stoichiometric amount of the substrate (second-order reaction condition), since the reactions of $P^{COMe}H$ were too fast under the pseudo-first-order reaction condition (in the presence of an excess amount of the substrate). Thus, the plot of $(A_0–A)/[Cu]_0(A–A_\infty)$ against time gave a straight line passing through the

Table 2-1. The second-order reaction rates (k_2) for the reactions of $\mathbf{1}^{X}$ and $\mathbf{P}^{COMe}H$ and reported BDE of Cu^{II}–X.

	$\mathbf{1}^{F}$	$\mathbf{1}^{Cl}$	$\mathbf{1}^{Br}$	$\mathbf{1}^{I}$
$k_2/10^2(M^{-1}\ s^{-1})$	1.25	0.50	2.53	10.34
BDE (kcal/mol) of Cu–X [16]	103	90	80	70

origin, from which the second-order rate constant (k_2) was obtained as the slope of the linear line as listed in Table 2-1. Reported Cu–X bond dissociation energy (BDE) values are also included in Table 2-1. And the plot of logk_2 against BDE of Cu–X is shown in Figure 2-4.

Notably, logk_2 of $\mathbf{1}^{\mathbf{I}}$, $\mathbf{1}^{\mathbf{Br}}$ and $\mathbf{1}^{\mathbf{Cl}}$ exhibited very good linear correlation with the reported BDE values[4] of Cu–X, where the weaker the Cu–X bond, the faster the reaction rate. This is consistent with the proposed mechanism involving rete-limiting reductive Cu–X dissociation reaction for the oxidation of $P^{COMe}H$.

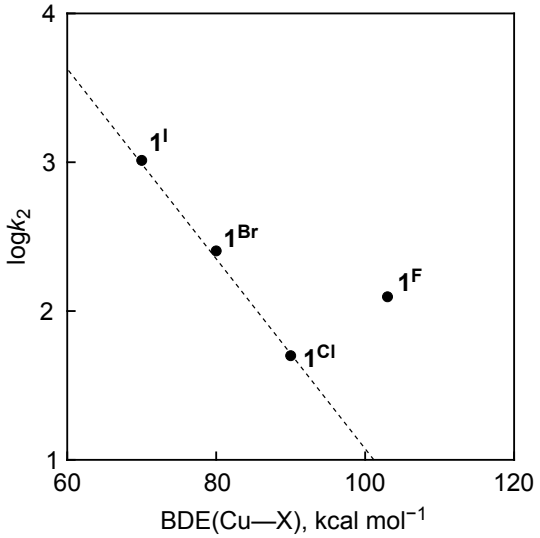

Figure 2-4. Plot of logk_2 vs. $BDE_{Cu–X}$ for the reaction of $\mathbf{1}^{\mathbf{X}}$ and $P^{COMe}H$.

On the other hand, logk_2 value of $\mathbf{1}^{\mathbf{F}}$ is significantly larger than that predicted from the linear line as shown in Figure 2-4. This result clear indicates that the reaction mechanism of $\mathbf{1}^{\mathbf{F}}$ is different from that of other complexes ($\mathbf{1}^{\mathbf{I}}$, $\mathbf{1}^{\mathbf{Br}}$, and $\mathbf{1}^{\mathbf{Cl}}$). Namely, oxidation of the phenol by $\mathbf{1}^{\mathbf{F}}$ may involve CPET mechanism rather than PTET mechanism. This may be due to the extremely strong BDE of HF (136 kcal/mol)[4] compared to those of others (HCl: 103 kcal/mol, HBr: 88 kcal/mol, HI: 71 kcal/mol).[4] In fact, the author obtained a similar KIE value as 1.4 with those of the CPET reactions mentioned above (KIE = 1.6~1.7, Figure S2-11). Formation of free HF was confirmed by ^{19}F-NMR for the reaction of $\mathbf{1}^{\mathbf{F}}$ with $P^{COMe}H$ in CH_3CN (*vide infra*), where the fluoride signal of HF was detected at $\delta = -148$ ppm and its yield was estimated as 78 % based on the copper(II) complex using OTf^- as an internal standard (Figure S2-15).

Conclusion

In this chapter, the author has demonstrated that the tetrahedrally distorted copper(II)-halide complexes $\mathbf{1}^{\mathbf{X}}$ supported by TMG_3tach ligand showed oxidation

ability toward phenol derivatives, where the substrates having an EW-substituent are oxidized via proton-transfer/electron-transfer (PTET) mechanism and those having an ED-substituent undergoes concerted proton/electron transfer (CPET) mechanism. Importance of the tetrahedral geometry of metal center was also demonstrated by comparing the reactivity with that of a copper(II)-halide complex $\mathbf{3^X}$ with a trigonal bipyramidal geometry. Moreover, the TMG group is shown to work as a proton accepter from the phenol substrate in the PTET mechanism, and in the reaction of P^{COMe} and $\mathbf{1^F}$, strong BDE of HF (product) greatly enhanced the reactivity.

Reference

(1) Shimizu, I.; Morimoto, Y.; Faltermeier, D.; Kerscher, M.; Paria, S.; Abe, T.; Sugimoto, H.; Fujieda, N.; Asano, K.; Suzuki, T.; Comba, P.; Itoh, S.; *Inorg. Chem*., **2017**, *56*, 9634-9645.

(2) Shimizu, I.; Morimoto, Y.; Velmurugan, G.; Gupta, T.; Paria, S.; Ohta, T.; Sugimoto, H.; Ogura, T.; Comba, P.; Itoh, S., *Chem. Eur. J*., **2019**, *25*, 11157-11165.

(3) Lan, Y.; Morimoto, Y.; Shimizu, I.; Sugimoto, H.; Itoh, S., *Inorg. Chem*., **2023**, *62*, 10539-10547.

(4) Luo, Y. R., *Conprehensive Handbook of Chemical Bond Energy*, CRC Press, Boca Raton, London, New York, **2007**.

(5) Pérez-Temprano, M. H.; Racowski, J. M.; Kampf, J. W.; Sanford, M. S., *J. Am. Chem. Soc.*, **2014**, *136*, 4097-4100.

(6) Hwang, S. J.; Powers, D. C.; Maher, A. G.; Anderson, B. L.; Hadt, R. G.; Zheng, S. L.; Chen, Y. S.; Nocera, D. G., *J. Am. Chem. Soc*., **2015**, *137*, 6472-6475.

(7) Hwang, S. J.; Anderson, B. L.; Powers, D. C.; Maher, A. G.; Hadt, R. G.; Nocera, D. G., *Organometallics*, **2015**, *34*, 4766-4774.

(8) Shields, B. J.; Doyle, A. G., *J. Am. Chem. Soc*., **2016**, *138*, 12719-12722.

(9) Mondal, P.; Pirovano, P.; Das, A.; Farquhar, E. R.; McDonald, A. R., *J. Am. Chem. Soc*., **2018**, *140*, 1834-1841.

(10) Mondal, P.; McDonald, A. R., *Chem. Eur. J*., **2020**, *26*, 10083-10089.

(11) Gygi, D. M.; Gonzalez, I.; Hwang, S. J.; Xia, K. T.; Qin, Y.; Johnson, E. J.; Gygi, F.; Chen ,Y. S.; Nocera, D. G., *J. Am. Chem. Soc*., **2021**, *143*, 6060-6064.

(12) Kariofillis, S. K.; Doyle, A. G., *Acc. Chem. Res*., **2021**, *54*, 988-1000.

(13) Bower, J. K.; Cypcar, A. D.; Henriquez, B.; Stieber, S. C. E.; Zhang, S., *J. Am. Chem. Soc*., **2020**, *142*, 8514-8521.

(14) Lovisari, M.; Gericke, R.; Twamley, B.; McDonald, A. R.; *Inorg. Chem*., **2021**, *60*, 15610-15616.

(15) Krockert, K. W.; Garg, F.; Heck, J.; Heinz, M. V.; Lange, J.; Schmidt, R.; Hoffmann, A.; Herres-Pawlis, S., *Dalton Trans.*, **2024**, *53*, 2973-2990.

(16) Raab,V.; Kipke, J.; Burghaus, O.; Sundermeyer, J., *Inorg. Chem*., **2001**, *40*, 6964-6971.
(17) Wittmann, H.; Raab, V.; Schorm, A.; Plackmeyer, J.; Sundermeyer, J.; *Eur. J. Inorg. Chem*., **2001**, 1937-1948.
(18) Manner, V. W.; Markle, T. F.; Freudenthal, J. H.; Roth, J. P.; Mayer, J. M., *Chem. Commun*., **2008**, 256-258.
(19) Ar, D.; Kilpatrick, A. F. R.; Cula, B.; Herwig, C.; Limberg, C.; *Inorg. Chem*., **2021**, *60*, 13844-13853.
(20) Collman, J. P.; Decréau, R. A.; Sunderland, C. J., *Chem. Commun*., **2006**, 3894-3896.
(21) Bailey, W. D.; Dhar, D.; Cramblitt, A. C.; Tolman, W. B., *J. Am. Chem. Soc*., **2019**, *141*, 5470-5480.

Supporting Information

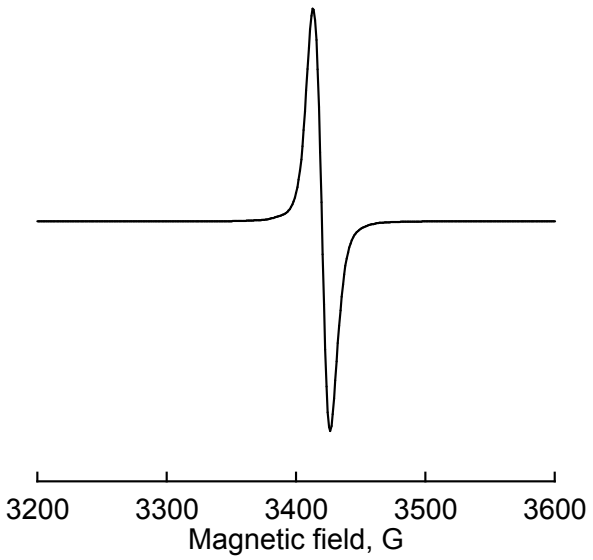

Figure S2-1. X-band EPR spectra of the post reaction solutions showing the existence of phenoxyl radical (P^{tBu}•) at g = 2.0041 in CH_2Cl_2 at 104 K. For the reaction of $\mathbf{1^{Br}}$ with $P^{tBu}H$.

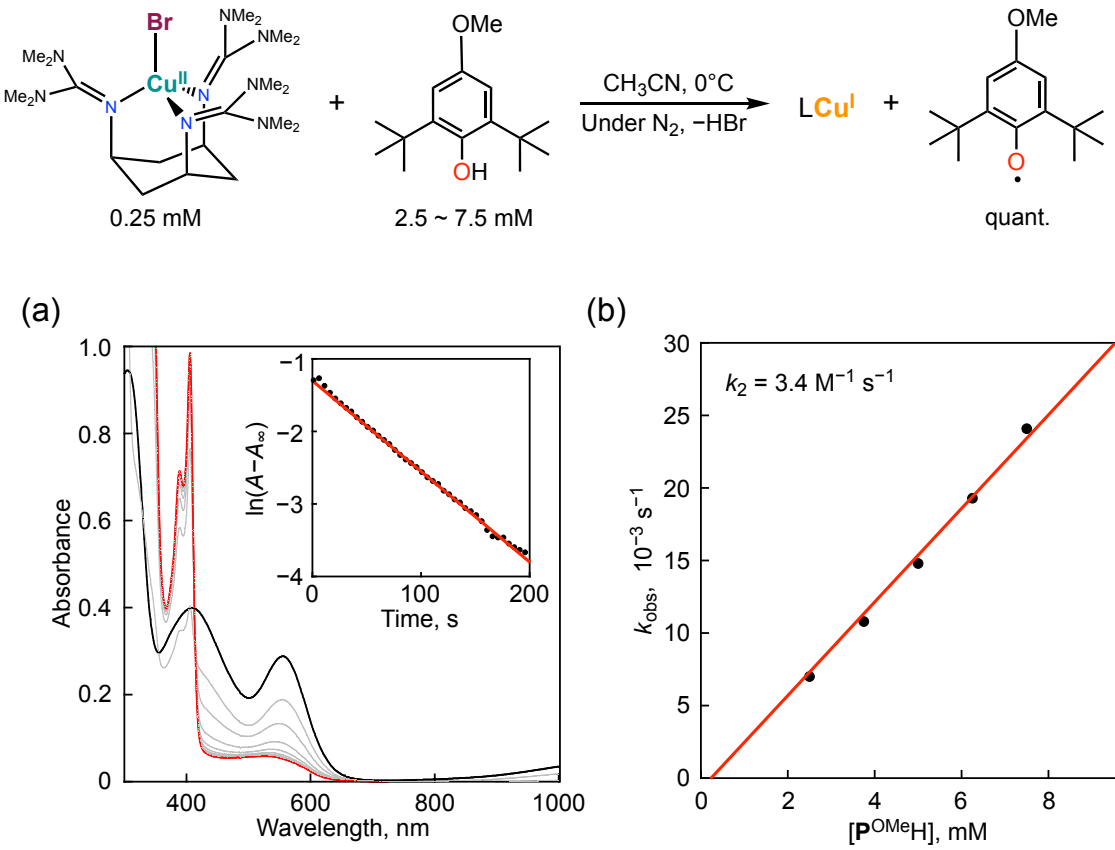

Figure S2-2. (a) UV-vis spectral change for the reaction of $\mathbf{1}^{\mathbf{Br}}$ (0.25 mM) with 4-OMe-2,6-di-*tert*-butylphenol ($P^{OMe}H$, 5.0 mM) in CH_3CN at 0°C. Inset: Pseudo first-order plots based on the absorption change at 560 nm. (b) Plot of k_{obs} vs. $[P^{OMe}H]$.

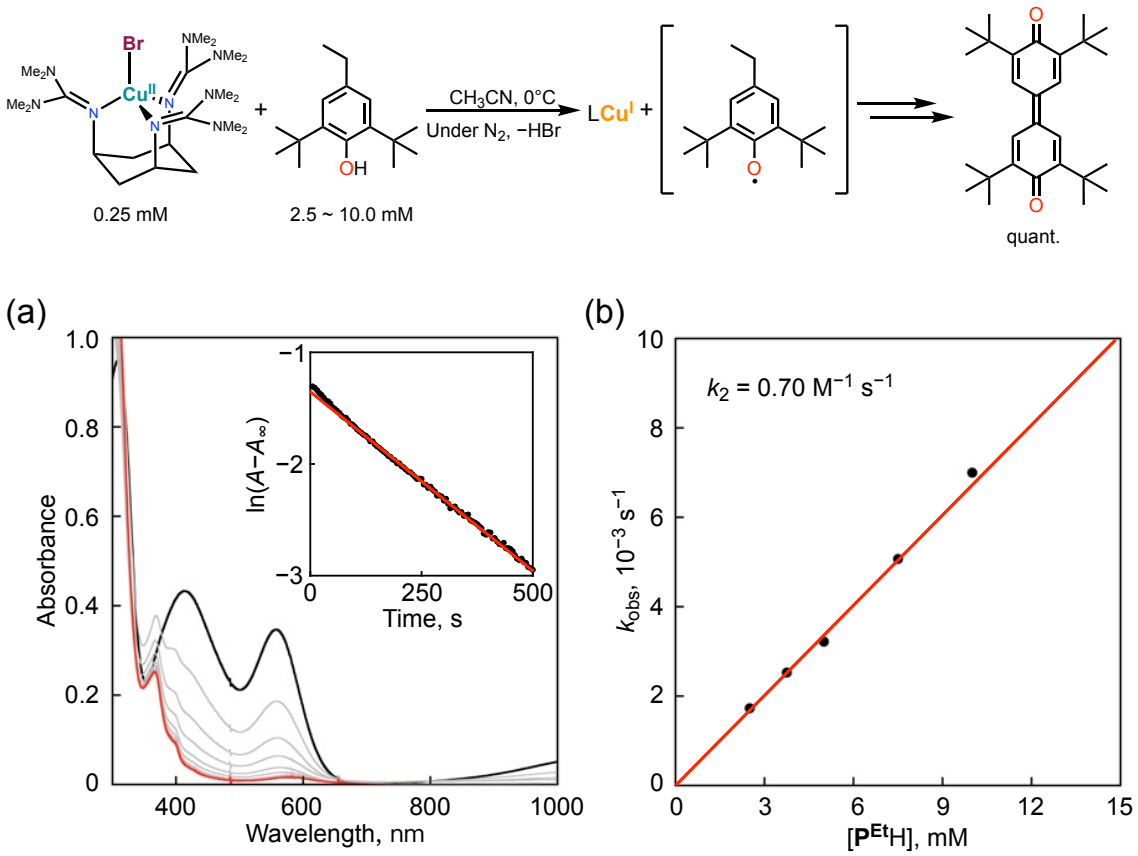

Figure S2-3. (a) UV-vis spectral changes for the reaction of $\mathbf{1}^{\mathbf{Br}}$ (0.25 mM) with 4-ethyl-2,6-di-*tert*-butylphenol ($P^{Et}H$, 5.0 mM) in CH_3CN at 0°C. Inset: Pseudo first-order plots based on the absorption change at 560 nm. (b) Plot of k_{obs} vs. [$P^{Et}H$].

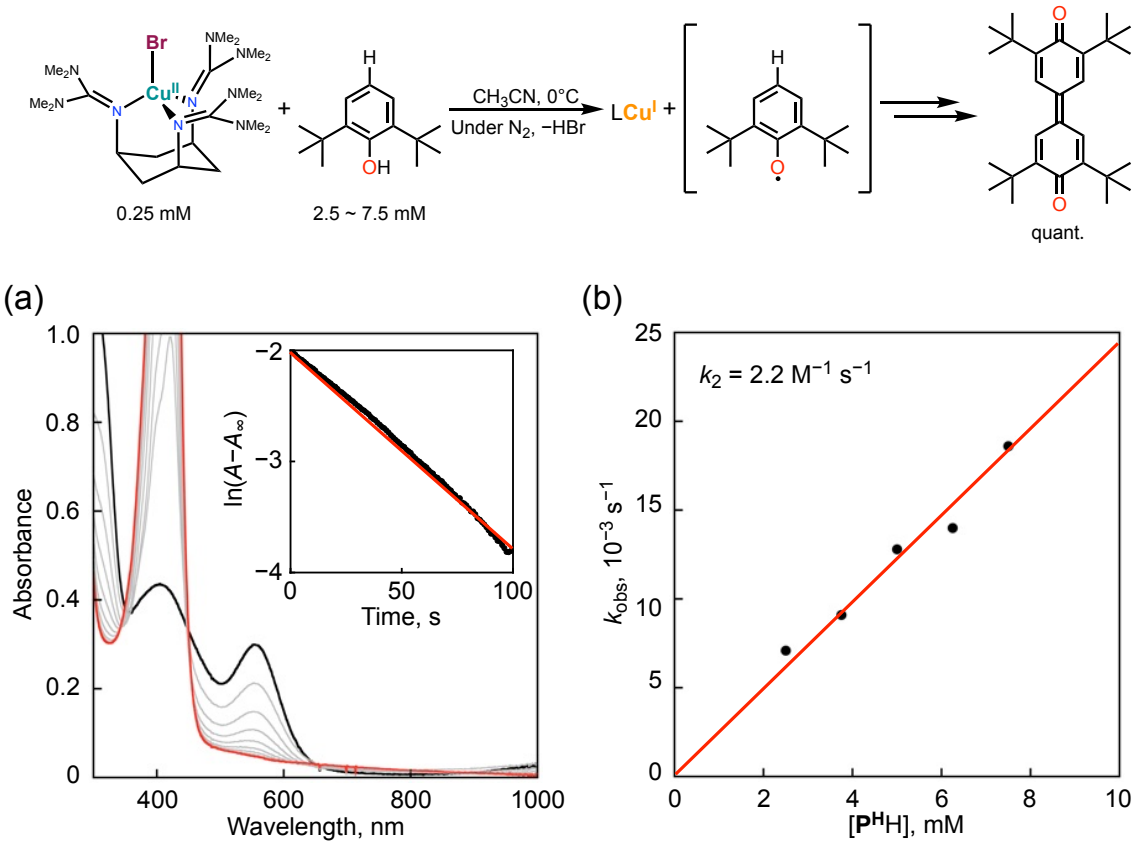

Figure S2-4. (a) UV-vis spectral changes for the reaction of $\mathbf{1}^{\mathbf{Br}}$ (0.25 mM) with 2,6-di-*tert*-butylphenol (P^HH, 7.5 mM) in CH_3CN at 0°C. Inset: Pseudo first-order plots based on the absorption change at 560 nm. (b) Plot of k_{obs} vs. [P^HH].

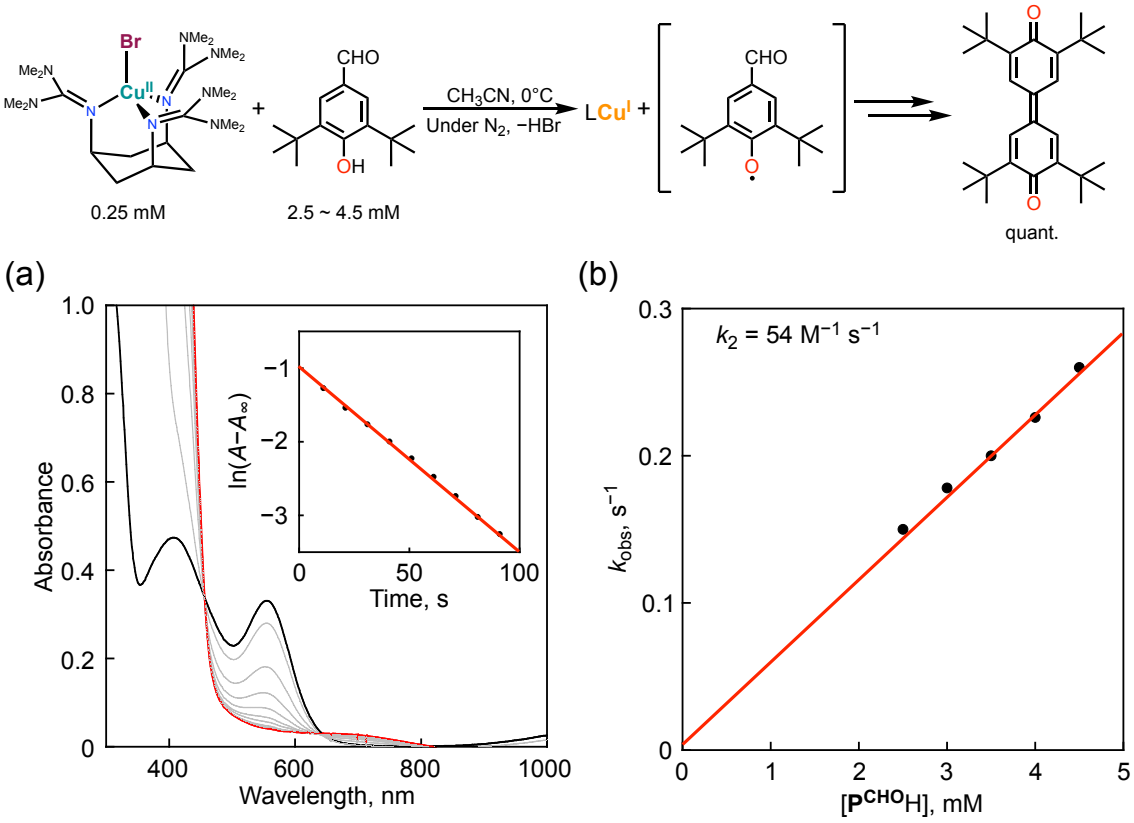

Figure S2-5. (a) UV-vis spectral changes for the reaction of $\mathbf{1}^{Br}$ (0.25 mM) with 4-formyl-2,6-di-*tert*-butylphenol ($P^{CHO}H$, 4.5 mM) in CH_3CN at 0°C. Inset: Pseudo first-order plots based on the absorption change at 560 nm. (b) Plot of k_{obs} vs. [$P^{CHO}H$].

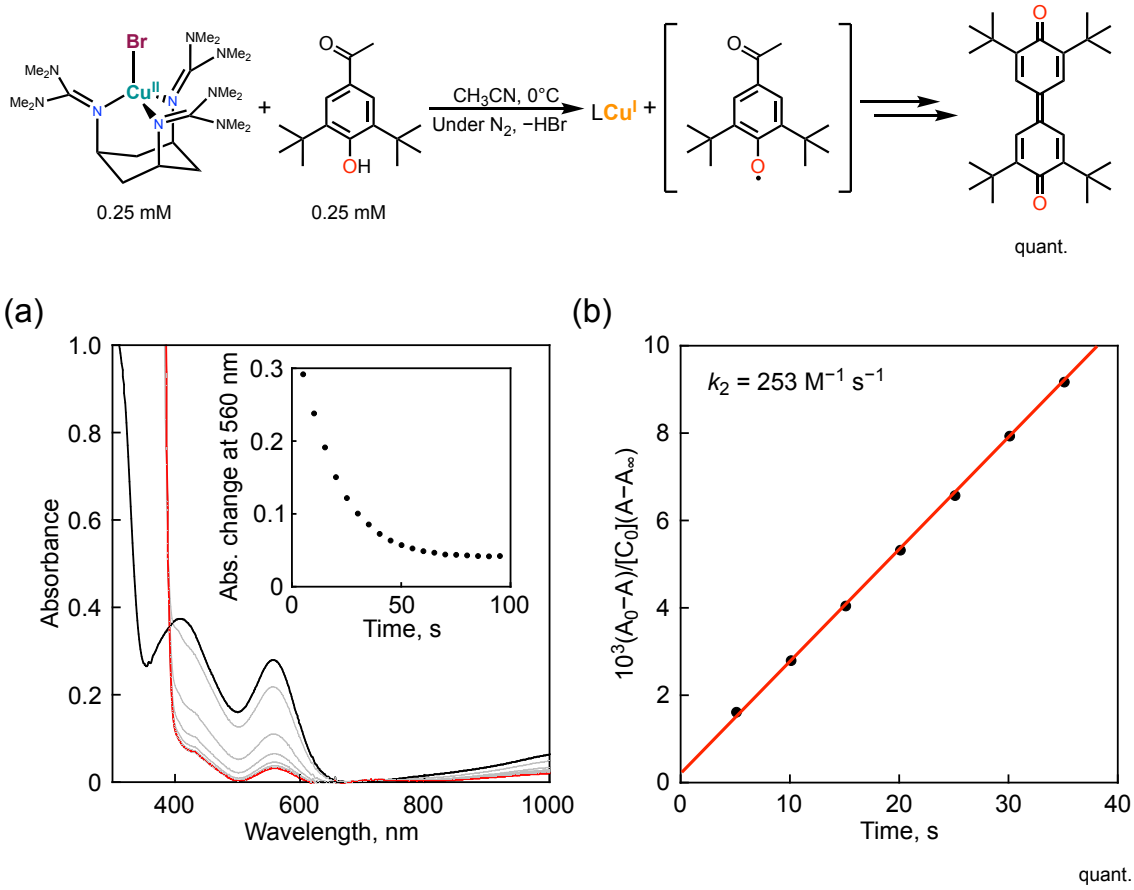

Figure S2-6. (a) UV-vis spectral changes for the reaction of $\mathbf{1}^{\mathbf{Br}}$ (0.25 mM) with 4-COMe-2,6-di-*tert*-butylphenol ($P^{COMe}H$, 0.25 mM) in CH_3CN at 0°C. Inset: Absorption change at 560 nm. (b) Second-order rate constant plot based on the absorption change at 560 nm.

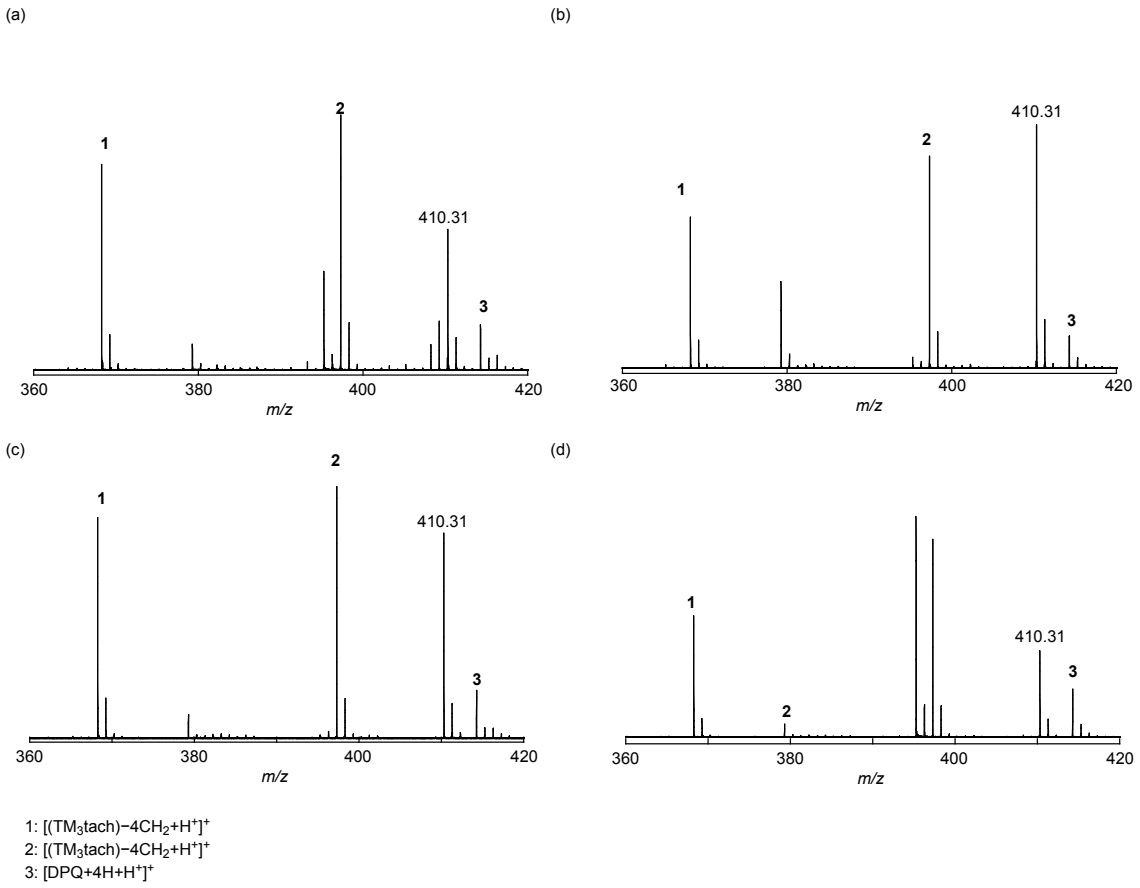

Figure S2-7. MALDI-TOF mass spectra of the post reaction solutions showing the formation of 3,3',5,5'-tetra-*tert*-butyl-[1,1'-bi(cyclohexylidene)]-2,2',5,5'-tetraene-4,4'-dione+2H]$^+$ in the reactions of **1**$^{\mathbf{Br}}$ and P$^{\mathrm{Y}}$H 4-Y-2,6-di-*tert*-butylphenol; (a) Y = Et, (b) Y = H, (c) Y = CHO, and (d) Y = COMe.

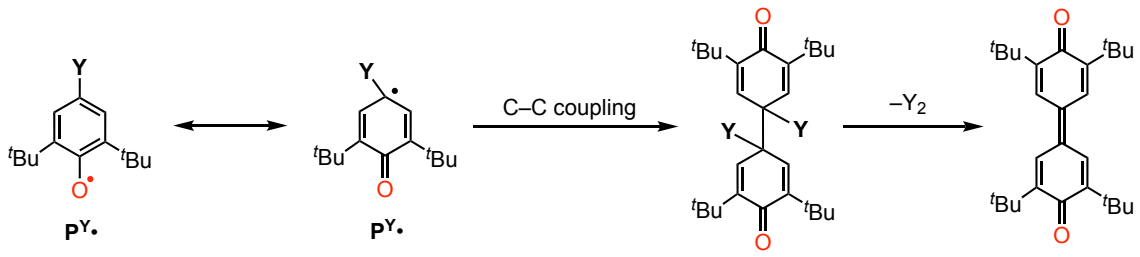

Scheme S2-1. Formation of 3,3',5,5'-tetra-*tert*-butyl-[1,1'-bi(cyclohexylidene)]-2,2',5,5'-tetraene-4,4'-dione by the C–C coupling reaction of **P**$^{\mathbf{Y}}$•.

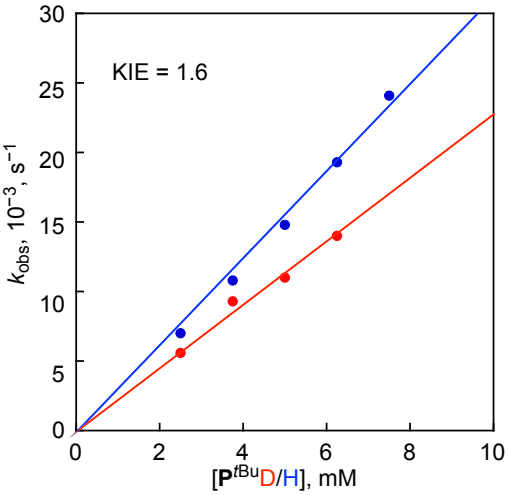

Figure S2-8. Plots of k_{obs} against phenol concentration for the reaction between **1^{Br}** with P^{OMe}H (blue) and P^{OMe}D (red).

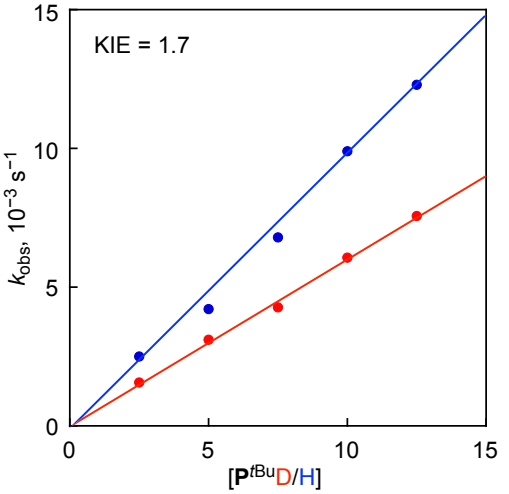

Figure S2-9. Plots of k_{obs} against phenol concentration for the reaction between **1^{Br}** with P$^{t\text{Bu}}$H (blue) and P$^{t\text{Bu}}$D (red).

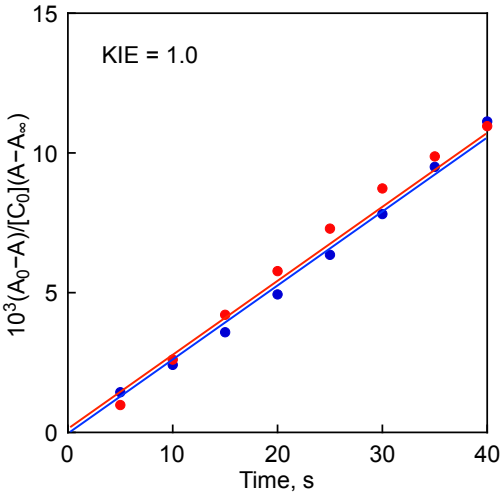

Figure S2-10 Second-order plot for the reaction between $\mathbf{1^{Br}}$ with $P^{COMe}H$ (blue) and $P^{COMe}D$ (red).

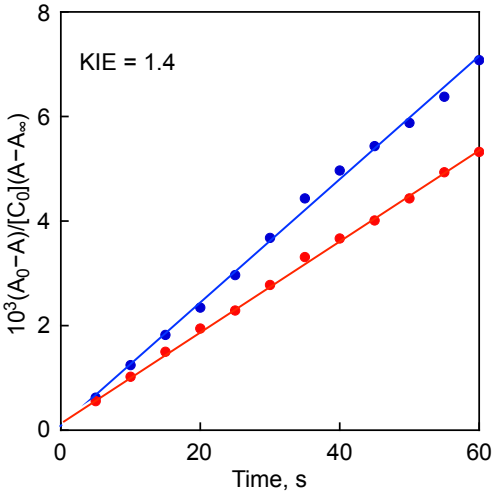

Figure S2-11. Second-order rate constant plot for the reaction between $\mathbf{1^{F}}$ with $P^{COMe}H$ (blue) and $P^{COMe}D$ (red).

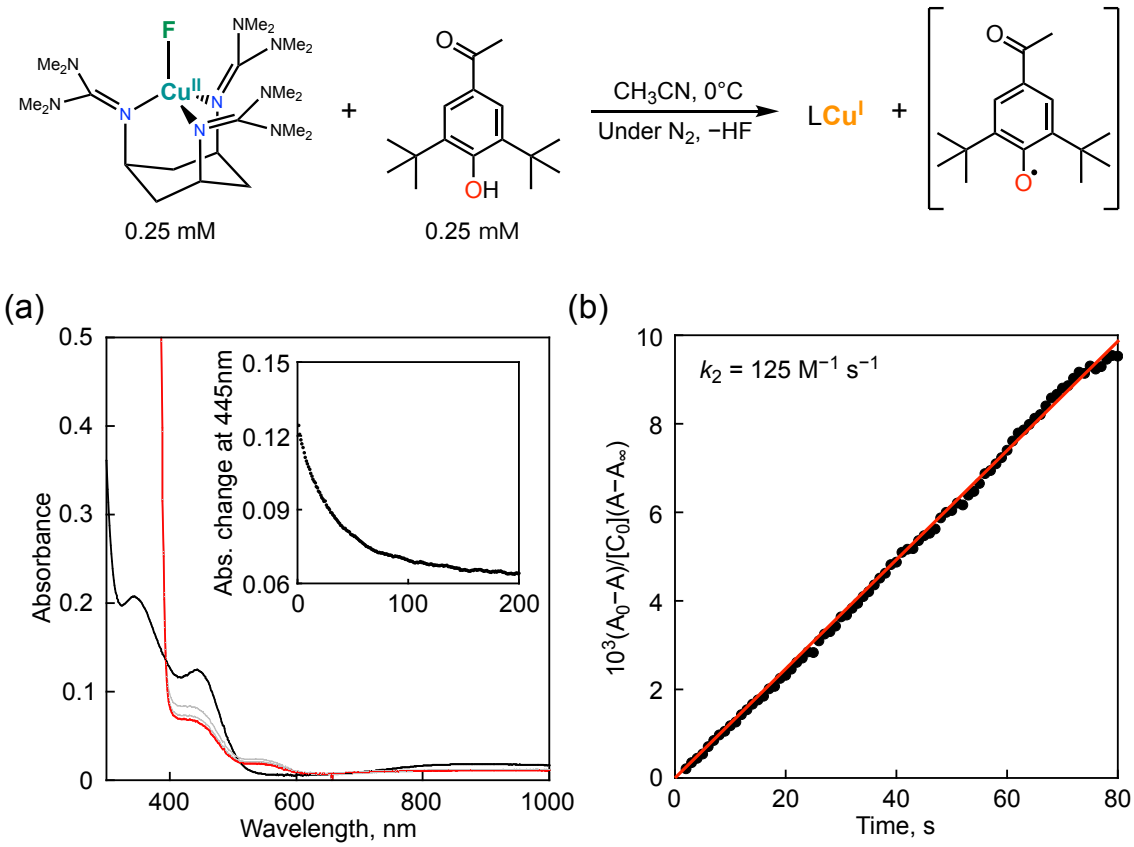

Figure S2-12. (a) UV-vis spectral changes for the reaction of $\mathbf{1}^{F}$ (0.25 mM) with 4-COMe-2,6-di-*tert*-butylphenol ($P^{COMe}H$, 0.25 mM) in CH_3CN at 0°C. Inset: Absorption change at 445 nm. (b) Second-order rate constant plot based on the absorption change at 445 nm.

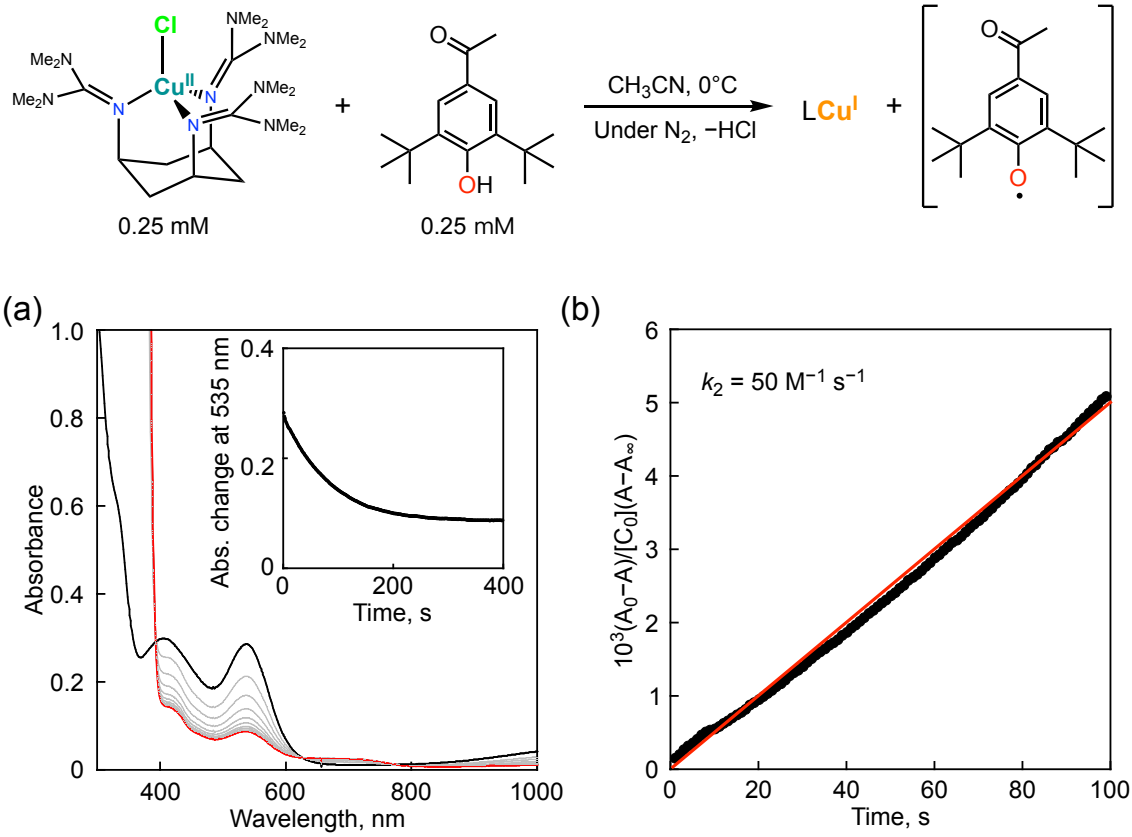

Figure S2-13. (a) UV-vis spectral changes for the reaction of $\mathbf{1}^{Cl}$ (0.25 mM) with 4-COMe-2,6-di-*tert*-butylphenol ($P^{COMe}H$, 0.25 mM) in CH_3CN at 0°C. Inset: Absorption change at 535 nm. (b) Second-order rate constant plot based on the absorption change at 535 nm.

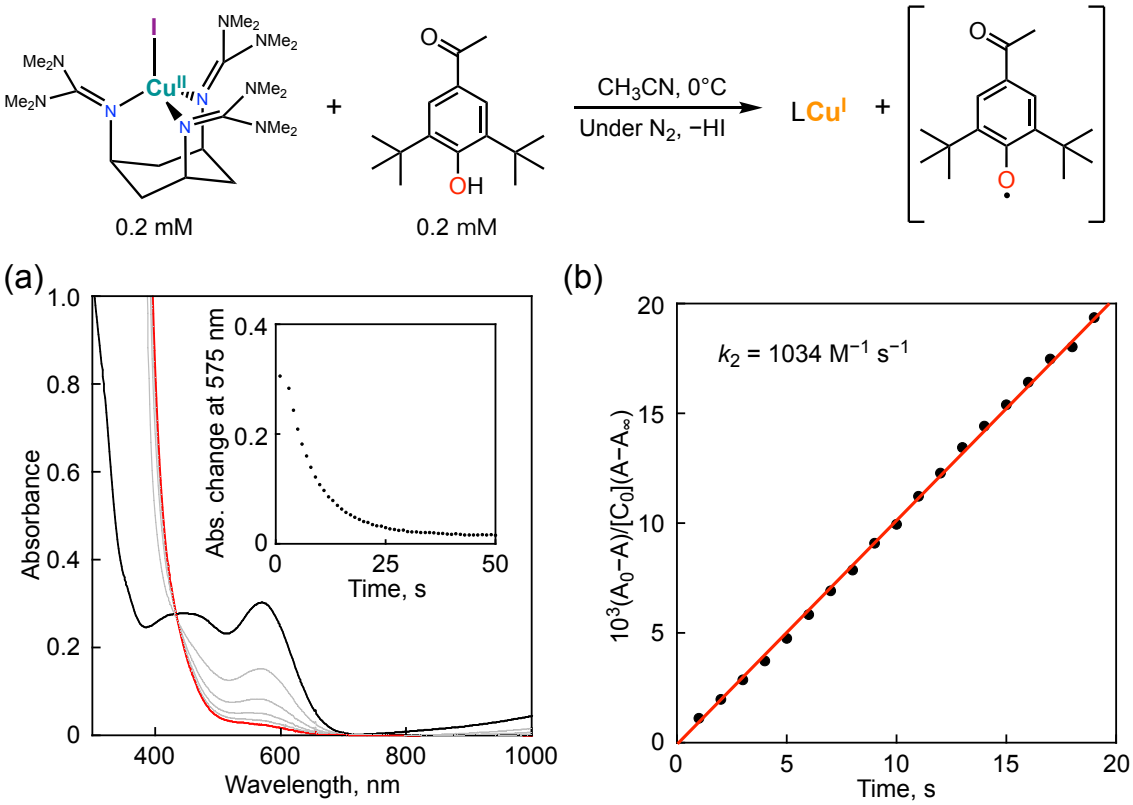

Figure S2-14. (a) UV-vis spectral change for the reaction of $\mathbf{1^I}$ (0.2 mM) with 4-COMe-2,6-di-*tert*-butylphenol ($P^{COMe}H$, 0.2 mM) in CH_3CN at 0°C. Inset: Absorption change based on absorbance at 575 nm. (b) Second-order plot based on the absorption change at 575 nm.

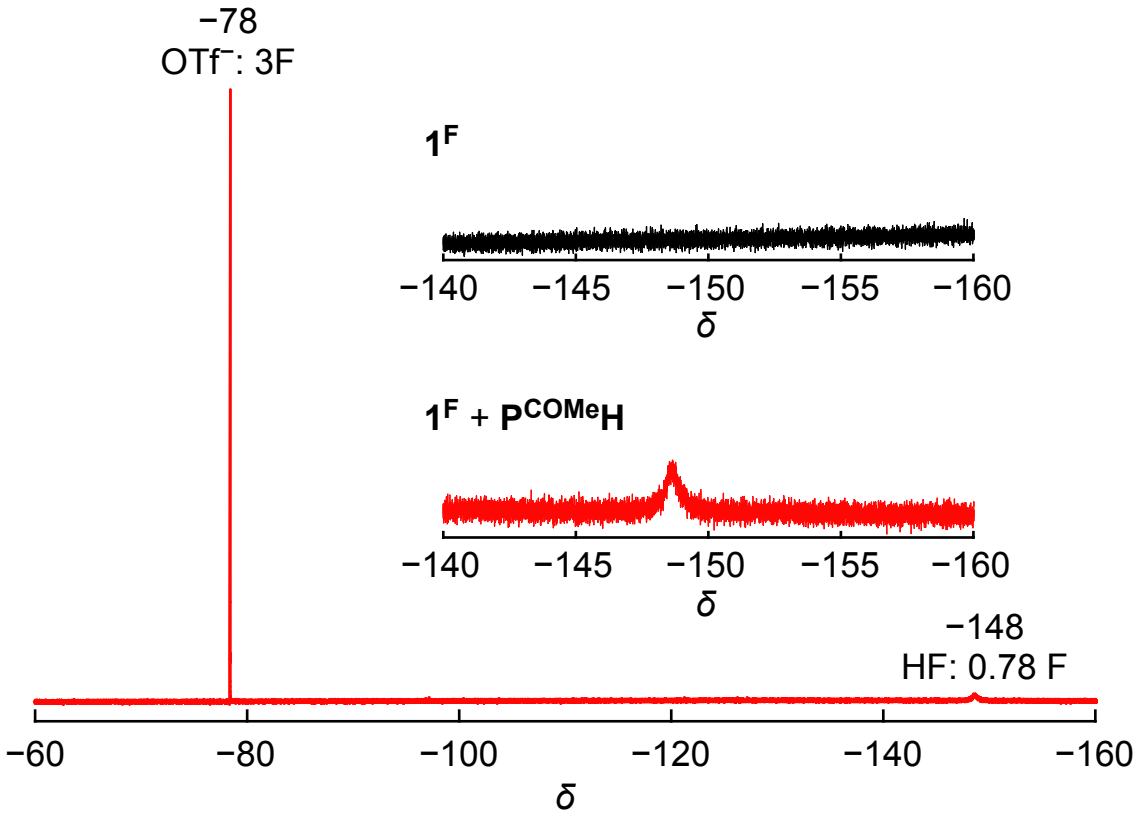

Figure S2-15. ^{19}F NMR spectra of a post reaction solution of **1^{F}** and P^{COMe}H in CH_3CN. The yield of HF was determined by the integral ratio between OTf^- and HF.

Chapter 3. Oxidation Reactivity of Mononuclear Tetrahedral Copper(II)-methoxide Complex

Introduction

High-valent (mostly tetravalent and pentavalent) transition-metal terminal oxygen complexes have long attracted much attention as a key reactive intermediate in the biological and abiological oxidation reactions.[1-9] In addition, tri-valent transition metal complexes with a terminal oxide or hydroxide ligand such as Fe^{III}–OMe, Mn^{III}–OH, and Ru^{III}–OH have been investigated as a functional model of lipoxygenases.[10-12] However, terminal oxygen complexes of late-transition metal such as copper, another important transition-metal element in the biological oxidation reactions, have been less explored. In this respect, Tolman and coworkers have developed the mononuclear high-valent copper(III) complexes containing hydroxide or alkoxide terminal ligand using dianionic ligands (*N*,*N*′-bis(2,6-diisopropylphenyl)-2,6-pyridinedicarboxamide derivatives), and explored their hydrogen atom abstraction (HAA) reactivity.[13-18] Garcia-Bosch and coworkers reported a copper(II)-hydroxide complex supported by a redox-active ligand, which upon oxidation provides "high-valent" intermediates consisting with the oxidized ligand and the Cu^{II}–OH core.[19, 20] Thus, these systems use the higher oxidation state (such as copper(III) or copper(II)-oxidized ligand for the substrate oxidation. It should be also noted that the copper centers in these systems exhibit square planer geometry stabilizing the high-valent oxidation state.

Recently, Itoh and coworkers have developed a series of *tetrahedral* copper(II) complexes, $[Cu^{II}(TMG_3tach)(L)]^+$ ($\mathbf{1^L}$), where TMG_3tach is an N_3-tridentate ligand consisting of *cis,cis*-1,3,5-triamino-cyclohexane (tach) and *N*,*N*,*N*′,*N*′-tetramethylguanidino (TMG) substituents and L is an anionic axial co-ligand (F^-, Cl^-, Br^-, I^-, MeO^-, $C_6F_5O^-$, $C_6F_5S^-$, and ROO^-) (Figure 3-1).[21-24] The copper(II)-halide complexes $\mathbf{1^X}$ (X = F^-, Cl^-, Br^-, and I^-) showed C–H and O–H activation reactivity, even though the metal ion has a normal copper(II) oxidation state but not a high-valent

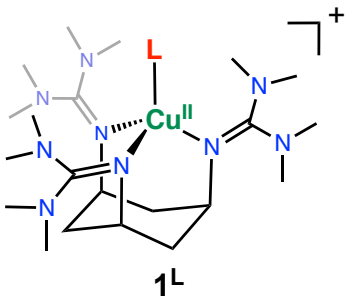

$\mathbf{1^L}$

Figure 3-1. Copper(II) complexes $\mathbf{1^L}$ used in this study (L = MeO^-, F^-, Cl^-, and Br^-).

oxidation state such as copper(III). In Chapter 2, the author concluded that such an oxidation reactivity is attributed to the tetrahedral geometry of the copper(II)-halide complexes which basically stabilizes the low-valent copper(I) oxidation state. Namely, the oxidation reactions by $\mathbf{1^X}$ utilizes the Cu^{II}/Cu^{I} redox couple in contrast to the ordinary oxidation reactions based on the Cu^{III}/Cu^{II} redox chemistry.

In this chapter, the author has found that the copper(II)-methoxide complex $\mathbf{1^{OMe}}$ exhibited much higher C–H and O–H activation reactivity compared to $\mathbf{1^X}$. The results will provide important insights into the oxidation mechanism of the mononuclear copper monooxygenases such as peptidylglycine α-hydroxylating monooxygenase (PHM), dopamine β-monooxygenase (DβM), and lytic polysaccharide monooxygenase (LPMO).

Experimental Section

General

The reagents and solvents used in this study, except the ligand and the copper complexes, were commercial products of the highest available purity and used as received without further purification, unless otherwise noted.[36] Ligand TMG_3tach and its Cu(II) complexes were prepared according to the reported procedures.[21] All reactions were carried out under N_2 atmosphere using standard Schlenkline or a glovebox (miwa DB0-1KP or KK-011-AS, KOREA KIYON product, $[O_2]<1$ ppm). UV-visible spectra were taken on a Jasco V-570 or a Hawlett Packard 8453 photo diode array spectrophotometer equipped with a Unisoku thermostated cryostat cell holder USP-203. Electrospray ionization mass spectra (ESI-MS) measurements were performed on a microTOF II focus (Bruker Daltonics). Electron paramagnetic resonance (EPR) spectra were measured on a BRUKER EMX-micro continuous-wave X-band spectrometer.

Kinetic Measurements

Kinetic measurements for the reactions of the copper(II) complexes $\mathbf{1^X}$ with external substrates were performed using a Hawlett-Pckard 8453 photo diode array spectrophotometer equipped with a Unisoku thermostated cryostat cell holder USP-203 (a desired temperature can be fixed within ± 0.5°C) in CH_2Cl_2. Typically, after formation of $\mathbf{1^{OMe}}$ by the reaction of $\mathbf{1^{Br}}$ (0.25 mM) with 3 equimolar amount of 3 $^{n}Bu_4NOH$ (10% in MeOH) at −20°C in CH_2Cl_2, the reactions were initiated by injecting a substrate solution into the solution of $\mathbf{1^{OMe}}$ with use of a microsyringe at a desired temperature. The reactions were monitored by following decrease in absorbance at 347 nm.

Results and Discussion

C–H Bond Activation

The methoxide complex $\mathbf{1}^{\mathbf{OMe}}$ was generated in situ by treating the bromide complex $\mathbf{1}^{\mathbf{Br}}$ (0.25 mM) in CH_2Cl_2 with 3 equiv. of TBAOH (tetrabutylammonium hydroxide, 10 % in methanol) as reported in previous work.[21] Quantitative formation of $\mathbf{1}^{\mathbf{OMe}}$ was confirmed by the UV-vis and EPR spectra (Figures S3-1 and S3-2) which were identical to those of the reported spectra.[21] $\mathbf{1}^{\mathbf{OMe}}$ is relatively stable at a low temperature like –60°C but decomposed slowly at a higher temperature (k_{dec} = 2.7 x 10^{-4} s^{-1} at –20°C, Figure S3-3). Then, the C–H bond activation reactivity of $\mathbf{1}^{\mathbf{OMe}}$ was examined using CHD (1,4-cyclohexadiene) as a substrate at –20°C (Scheme 3-1).

Scheme 3-1. Reaction of $\mathbf{1}^{\mathbf{OMe}}$ and 1,4-cyclohexadiene (CHD).

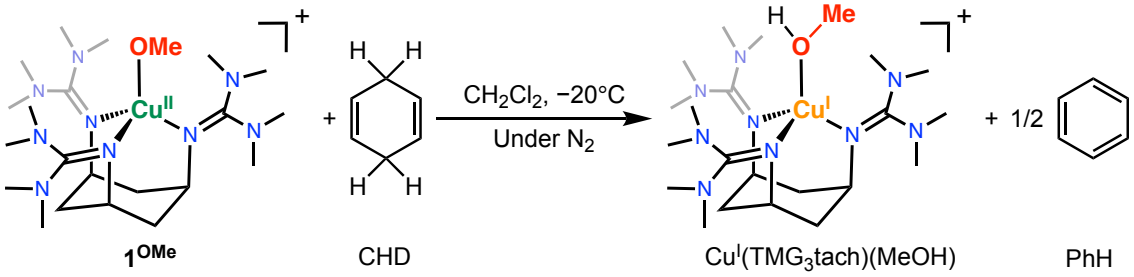

In Figure 3-2(a) is shown the spectral changes observed upon addition of CHD (250 mM in CH_2Cl_2) to the $\mathbf{1}^{\mathbf{OMe}}$ solution described above. The absorption band at 347 nm due to $\mathbf{1}^{\mathbf{OMe}}$ gradually decreased obeying first-order kinetics (inset of Figure 3-2(a)), and the first-order rate constant (k_{obs}) showed first-order dependence on the

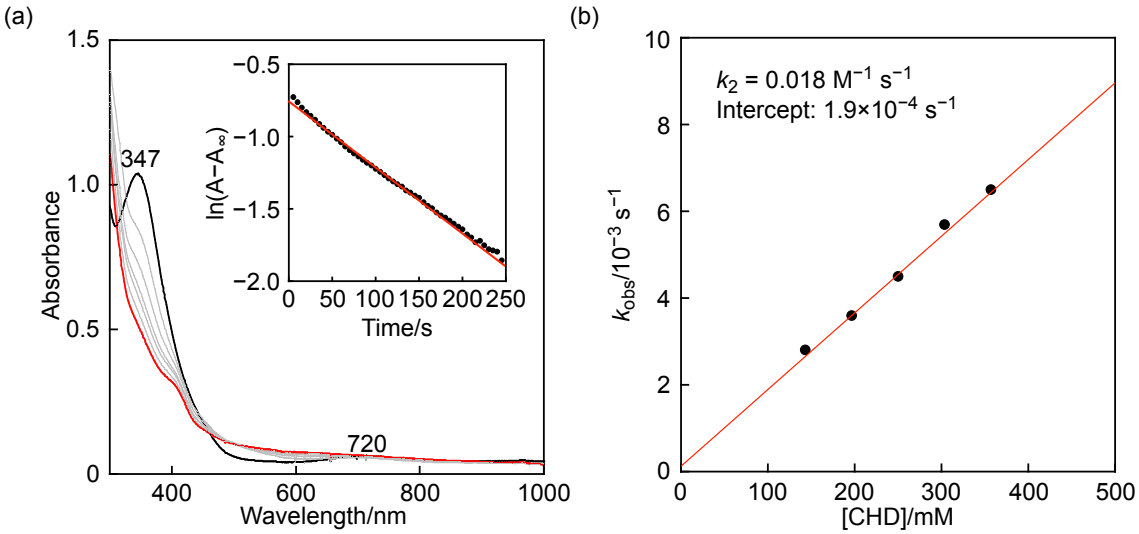

Figure 3-2. (a) UV-vis spectral changes for the reaction of $\mathbf{1}^{\mathbf{OMe}}$ (0.25 mM) with 1,4-cyclohexadiene (CHD, 250 mM) in CH_2Cl_2 at −20°C. Inset: First-order plot based on the absorption change at 347 nm. (b) Plot of k_{obs} vs. [CHD].

concentration of CHD (Figure 3-2(b)), from which the second-order rate constant was determined as 1.8 x 10^{-2} M^{-1} s^{-1} from the slope. In the plot of k_{obs} against the CHD concentration (Figure 3-2(b)), there is a small intercept (1.9 x 10^{-4} s^{-1}) which is almost the same to the self-decomposition rate constant k_{dec} determined in the absence of substrate (Figure S3-3). From the post-reaction solution, benzene was detected as the oxidation product of CHD and its yield was determined as 32% based on $\mathbf{1}^{\mathbf{OMe}}$ using GC-FID (maximum yield of benzene is 50% since $\mathbf{1}^{\mathbf{OMe}}$ is a one-electron oxidant). The post-reaction solution was EPR silent indicating the disappearance of the copper(II) complex $\mathbf{1}^{\mathbf{OMe}}$, and ESI-MS analysis showed the formation of a copper(I)-methanol complex (Figures S3-4 and S3-5). In chapter 1, the author examined the oxidation of CHD by $\mathbf{1}^{\mathbf{X}}$ (X = F^-, Cl^-, and Br^-), where $\mathbf{1}^{\mathbf{F}}$ exhibited the highest reactivity and the second-order rate constant was 1.4 x 10^{-3} M^{-1} s^{-1} at 25°C.[23] However, the reaction did not proceed at the low temperature like –20°C. Thus, it can be concluded that the C–H activation reactivity of $\mathbf{1}^{\mathbf{OMe}}$ is extremely higher than that of the halide complexes $\mathbf{1}^{\mathbf{X}}$.

The oxidation of CHD by $\mathbf{1}^{\mathbf{OMe}}$ proceeds *via* a PCET (proton-coupled electron-transfer) mechanism where proton is transferred to the axial ligand MeO^- giving MeOH and electron is transferred to the copper(II) ion giving the copper(I) complex (Scheme 1). The thermodynamics of PCET reactions are evaluated by the pK_a value and the reduction potential of the oxidant.[25, 26] Since the author has not yet succeeded to determine those values of $\mathbf{1}^{\mathbf{OMe}}$ and $\mathbf{1}^{\mathbf{X}}$, quantitative evaluation of the reaction rates is difficult at this stage. Nonetheless, the higher reactivity of $\mathbf{1}^{\mathbf{OMe}}$ compared to the halide complexes $\mathbf{1}^{\mathbf{X}}$ can be attributed to the higher basicity of the methoxide ligand (pK_a of MeOH is 29 in DMSO) compared to that of Br^- (pK_a of HBr is 0.9 in DMSO).[27]

O–H Bond Activation

Reactivity of $\mathbf{1}^{\mathbf{OMe}}$ toward phenolic substrates (4-sustituted-2,6-di-*tert*-butylphenol P^YH) was then examined (Scheme 3-2).

Scheme 3-2. Reaction of $\mathbf{1}^{\mathbf{OMe}}$ and 4-substituted-2,6-di-*tert*-butyophenol (P^YH)

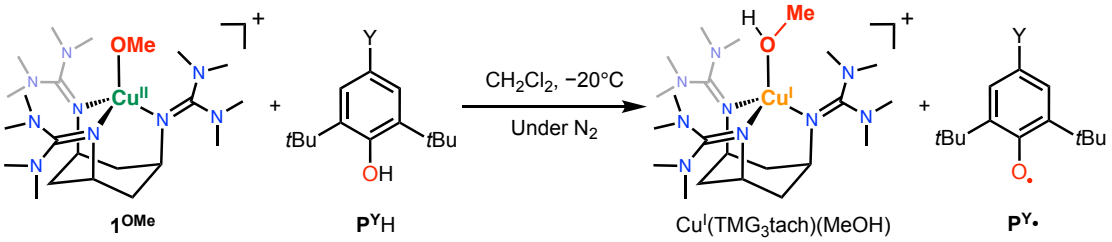

Figure 3(a) shows the spectral changes observed upon addition of $P^{t\mathrm{Bu}}H$ (Y = *tert*-butyl, 25 mM) to $\mathbf{1}^{\mathbf{OMe}}$ (0.25 mM) in CH_2Cl_2 at −20 °C under an N_2 atmosphere as a typical example, where the absorption bands at 347 nm and 720 nm due to $\mathbf{1}^{\mathbf{OMe}}$ gradually decrease with a concomitant increase in the absorption bands at 380, 400 and

626 nm, obeying first-order kinetics as shown in the inset of Figure 3-3(a)). The absorption bands of the post-reaction solution at 380, 400 and 626 nm are identical to those of 2,4,6-tri-*tert*-butylphenoxyl radical (P^{tBu}•).[28] On the basis of the molar absorption coefficient of P^{tBu}• at λ_{max}=626 nm (ε = 400 ± 10 M^{-1} cm^{-1}), the yield of the phenoxyl radical was estimated as ~85% based on $\mathbf{1}^{\mathbf{OMe}}$. In this case as well, the ESI-MS of the post-reaction solution showed the formation of copper(I)-methanol complex (Figure S3-6). The formation of the phenoxyl radical and the copper(I) complex was further confirmed by the EPR spectrum shown in Figure S3-7, where only an EPR signal ascribable to P^{tBu}• was observed at g = 2.0041,[29] but the EPR signals due to the copper(II) complex $\mathbf{1}^{\mathbf{OMe}}$ completely disappeared.

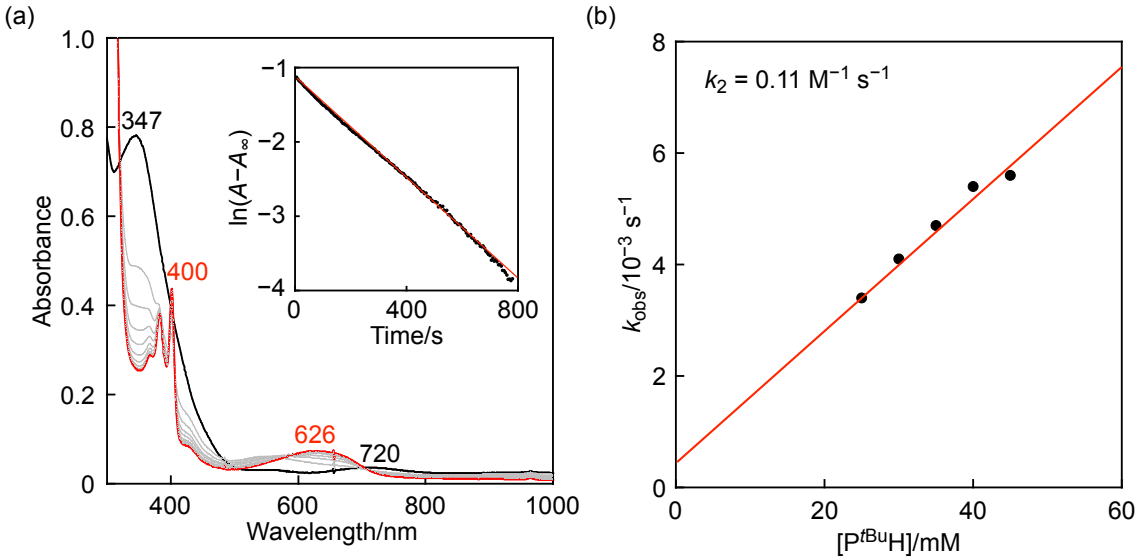

Figure 3-3. (a) UV-vis spectral changes for the reaction of $\mathbf{1}^{\mathbf{OMe}}$ (0.25 mM) with 2,4,6-tri-*tert*-butylphenol (P^{tBu}H**,** 25 mM) in CH_2Cl_2 at −20°C. Inset: Pseudo first-order plot based on the absorption change at 347 nm. (b) Plot of k_{obs} vs. [P^{tBu}H].

The pseudo first-order rate constant (k_{obs}) obtained from the plot of ln(A−A_∞) against the reaction time (inset of Figure 3-3(a)) showed linear correlation with the concentration of P^{tBu}H as shown in Figure 3-3(b), from which the second-order rate constant (k_2) was determined as 0.11 M^{-1} s^{-1} from the slope.

To examine the electronic effects of the *para*-substituents (Y) of the phenol substrates, the reactions with a series of 4-substituted-2,6-di-*tert*-butylphenols (Y = OMe, H, Br, and COMe) were examined under the same reaction conditions (in CH_2Cl_2 at −20°C). The kinetic analysis data are given in Figures S3-8–S3-11. In the reactions with P^{OMe}H, P^{H}H, and P^{Br}H, the reaction obeyed first-order kinetics in the presence of an excess amount of P^{Y}H (a pseudo first-order reaction condition) and plots of the observed first-order rate constants (k_{obs}) against the substrate concentration exhibited

linear correlations, from which the second-order rate constants (k_2) were determined as 0.35 M^{-1} s^{-1}, 0.31 M^{-1} s^{-1}, and 1.8 M^{-1} s^{-1} from the slopes, respectively. For $P^{COMe}H$, the second-order rate constant (k_2) was determined as 31 M^{-1} s^{-1} in the reaction of a stoichiometric amount of the substrate (under a second-order reaction condition, Figure S3-11), because the reaction was too fast under the pseudo-first-order reaction conditions (in the presence of an excess amount of the substrate). In the case of $P^{OMe}H$ as the substrate, the quantitative formation of the phenoxyl radical product P^{OMe}• was also confirmed by the appearance of its characteristic absorption bands at 387, 406 and 540 nm (Figure S3-8).[30] The formation of the phenoxyl radical P^{OMe}• and the copper(I)-methanol complex was also confirmed by the EPR spectrum shown in Figure S3-12, where only an EPR signal ascribable to P^{OMe}• was observed at g = 2.0041,[24] whereas the copper(II) complex $\mathbf{1}^{\mathbf{OMe}}$ completely disappeared. On the other hand, the final organic products of the reactions with other phenols $P^{Y}H$ (Y = H, Br, and COMe) were 3,3',5,5'-tetra-*tert*-butyl-[1,1'-bi(cyclohexylidene)]-2,2',5,5'-tetraene-4,4'-dione as evident from the intense absorption bands below ~500 nm (Figures S3-9–S3-11), which was formed by the C–C coupling reaction of generated phenoxyl radical species P^{Y}• and following elimination of Y_2 from the dimeric intermediate.[24] In all the cases, the ESI-MS of the post-reaction solutions showed the formation of copper(I)-methanol complex (Figure S3-6).

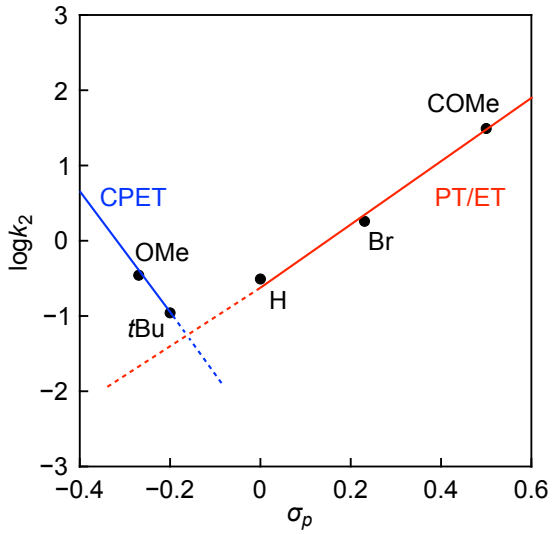

Figure 3-4. Hammett plot for the reaction of $\mathbf{1}^{\mathbf{OMe}}$ and $P^{Y}H$.

Figure 3-4 shows a Hammett plot of logk_2 against σ_p of the substrate substituents. As clearly seen, logk_2 increases linearly as the electron-withdrawing (EW) ability of the para-substituent Y increases (increasing the σ_p value) in going from Y = H to COMe with a Hammett ρ value of 2.7. In the cases of Y = OMe and *t*Bu, however, the data points deviated from that linear line and the logk_2 values were larger than those expected

Scheme 3-3. Possible mechanism for the phenol oxidation reaction by $\mathbf{1}^{\mathbf{OMe}}$.

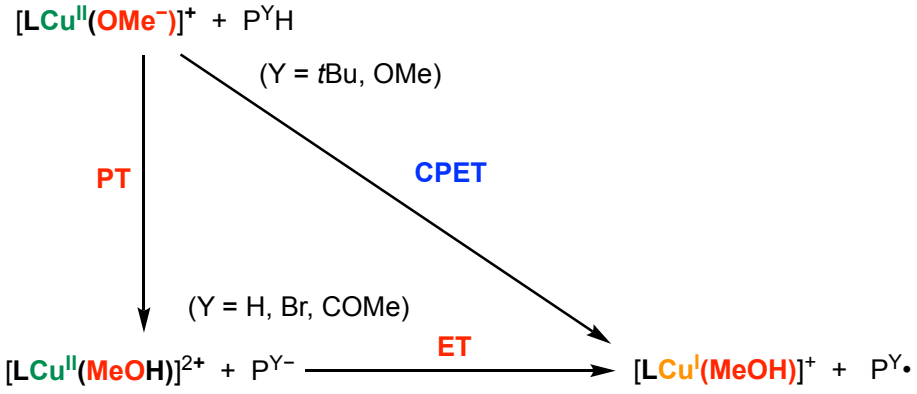

work using copper(II)-bromide complex $\mathbf{1}^{\mathbf{Br}}$ and in the reactions of phenol derivatives with copper(III)-superoxide (Cu^{III}–OO•) and nickel(III)-fluoride (Ni^{III}–F) complexes supported by 2,6-diamidepyridine ligands.[24, 31, 32] Those results were interpreted as a change of reaction mechanism across the series of phenol derivatives. Namely, the reactions with the phenols have the electron-withdrawing (EW) substituent involve a PT-ET (proton transfer following electron transfer) mechanism, whereas the oxidation of phenols with the electron-donating (ED) substituent includes a concerted proton/electron transfer (CPET) mechanism as illustrated in Scheme 3-3. For the phenol substrates with the EW-substituent such as $P^{COMe}H$ deprotonation of the phenol substrate by methoxide group (pK_a = 29 in DMSO)[33] takes place forming phenolates and methanol complex. Then, electron transfer from the generated phenolate to the copper(II) ion occurs, giving a copper(I)-methanol complex and the phenoxyl radical product. On the other hand, for the reaction of phenols with the ED-substituent like $P^{OMe}H$, proton-transfer and electron-transfer occur concertedly (CPET mechanism) due to the higher pK_a of the phenolic proton of $P^{OMe}H$.

To gain further insight into the O–H activation mechanism, the effects of the axial ligand X were examined using $P^{OMe}H$ as a substrate under the same reaction conditions. Figure S3-13 shows the kinetic analysis data for the reaction of $\mathbf{1}^{\mathbf{Br}}$ with $P^{OMe}H$ under the same experimental conditions. The quantitative formation of the phenoxyl radical product P^{OMe}• was also confirmed by the appearance of its characteristic absorption bands at 387, 406 and 540 nm (Figure S3-13(a)). The second-order rate constant (k_2) were determined as 0.15 M^{-1} s^{-1} in a similar manner (Figure S3-13(b)). Apparently, the reactivity of $\mathbf{1}^{\mathbf{OMe}}$ is larger than that of $\mathbf{1}^{\mathbf{Br}}$. However, difference in the reactivity between $\mathbf{1}^{\mathbf{OMe}}$ and $\mathbf{1}^{\mathbf{Br}}$ for the phenol oxidation was smaller than that in the oxidation of CHD. This may be due to the lower pK_a of $P^{OMe}H$ compared to that of CHD. Namely, in the oxidation of $P^{OMe}H$, the electron-transfer process governs the overall reaction rate.

Scheme 3-4. Reaction of $\mathbf{1^X}$ and TEMPO-H.

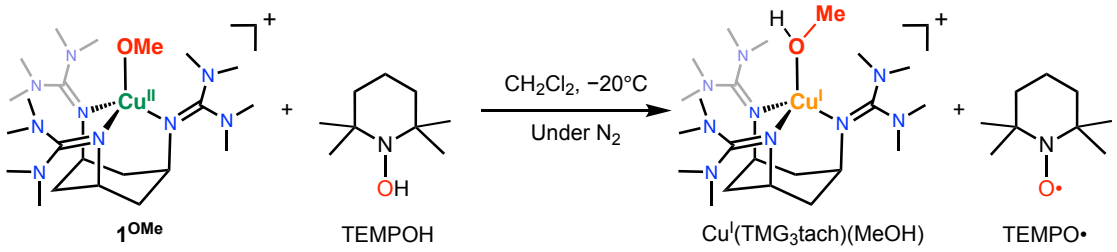

The effects of the axial ligand X was further examined using $\mathbf{1^{OMe}}$, $\mathbf{1^{Br}}$, $\mathbf{1^{Cl}}$, and $\mathbf{I^F}$ in the reaction with TEMPOH (2,2,6,6-tetramethylpiperidin-1-ol) having weaker BDFE (65 kcal/mol)[26] as the substrate. The kinetic analysis data are given in Figures S3-14–S3-17. The second-order rate constants (k_2) were determined as 163, 0.049, 0.26, and 3.1 M^{-1} s^{-1} for the reactions of $\mathbf{1^{OMe}}$, $\mathbf{1^{Br}}$, $\mathbf{1^{Cl}}$, and $\mathbf{I^F}$ in the same way. In the reaction of $\mathbf{1^{OMe}}$, formation of TEMPO• (2,2,6,6-tetramethylpiperidin-1-oxyl) and the copper(I)-methanol complex was confirmed by the EPR spectrum shown in Figure S3-18, where only an EPR signal ascribable to TEMPO• was observed at g = 2.0042, whereas the copper(II) complex $\mathbf{1^{OMe}}$ completely disappeared (Scheme 3-4). The ESI-MS of the post-reaction solutions also showed the formation of copper(I)-methanol complex (Figure S3-19).

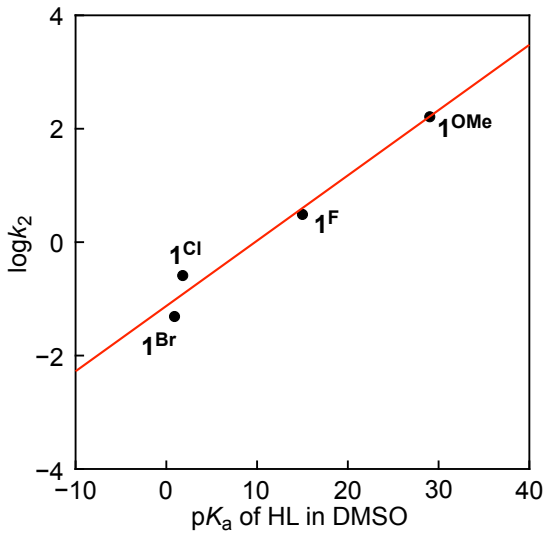

Figure 3-5. Plot of logk_2 vs. pK_a of HL for the reaction of $\mathbf{1^L}$ and TEMPOH.

In this case as well, reactivity of $\mathbf{1^{OMe}}$ was much larger than those of the halide complexes. Figure 3-5 shows the plot of logk_2 against the pK_a values of HBr, HCl, HF, and MeOH, where a good linear correlation is obtained. Namely, the higher the basicity of the conjugated base (Br^-, Cl^-, F^-, and MeO^-) the higher the oxidation

reactivity. This is consistent with the above discussion that the higher reactivity of $\mathbf{1}^{\mathbf{OMe}}$ is attributed to the higher basicity of methoxide ligand, enhancing the proton-transfer process in the oxidation of TEMPOH via PCET mechanism.[25]

Conclusion

In this chapter, reactivity of a mononuclear tetrahedral copper(II)-methoxide complex $\mathbf{1}^{\mathbf{OMe}}$ supported an N_3-tridentate ligand (TMG_3tach) was examined in the C–H and O–H bond activation reactions using 1,4-cyclohexadiene (CHD), 4-sustituted-2,6-di-*tert*-butylphenol (P^YH), and 2,2,6,6-tetramethylpiperidin-1-ol (TEMPOH) as the substrates. In these reactions, $\mathbf{1}^{\mathbf{OMe}}$ showed much higher reactivity compared to the copper(II)-halide complexes $\mathbf{1}^{\mathbf{X}}$. Such an enhanced reactivity can be attributed to the higher basicity of methoxide (MeO^-) ligand compared to those of halide ligands (X^-), enhancing the proton-transfer process in the proton-coupled electron-transfer mechanism. In the C–H and O–H bond activation reactions, it is well documented that the higher basicity of the terminal oxygen ligand of high-valent iron and manganese complexes is important in enhancing the reactivity.[3, 34, 35] The present study demonstrated that the same is true in the copper(II) system.

Reference

(1) Larson, V. A.; Battistella, B.; Ray, K.; Lehnert, N.; Nam, W., *Nat. Rev. Chem*., **2020**, *4*, 404-419.

(2) Borovik, A.S., *Chem. Soc. Rev*., **2011**, *40*, 1870-1874.

(3) Lee, J. L.; Ross, D. L.; Barman, S. K.; Ziller, J. W.; Borovik, A. S., *Inorg. Chem*., **2021**, *60*, 13759-13783.

(4) Sacramento, J. J. D.; Goldberg, D. P., *Acc. Chem. Res*. **2018**, *51*, 2641-2652.

(5) Kal, S.; Xu, S.; Que, L., *Angew. Chem. Int. Ed*., **2020**, *5*, 7332-7349.

(6) Collins, T. J.; Ryabov, A. D., *Chem. Rev*., **2017**, *117*, 9140-9162.

(7) Follmer, A. H.; Borovik, A. S., *Dalton Trans*., **2023**, *52*, 11005-11016.

(8) Rice, D. B.; Massie, A. A.; Jackson, T. A., *Acc. Chem. Res*., **2017**, *50*, 2706-2717.

(9) Shimoyama, Y.; Kojima, T., *Inorg. Chem*., **2019**, *5*, 9517-9542.

(10) Goldsmith, C. R.; Jonas, R.T.; Stack, T. D. P., *J. Am. Chem. Soc*., **2002**, *124*, 83-96.

(11) Goldsmith, C. R.; Cole, A. P.; Stack, T. D. P.; *J. Am. Chem. Soc*., **2005**, *127*, 9904-9912.

(12) Ohzu, S.; Ishizuka, T.; Kotani, H.; Kojima, T. Kojima., *Chem. Commun*., **2014**, *50*, 15018-15021.

(13) Donoghue, P. J.; Tehranchi, J.; Cramer, C. J.; Sarangi, R.; Solomon, E. I.; Tolman, W. B., *J. Am. Chem. Soc*., **2011**, *133*, 17602-17605.

(14) Dhar, D.; Tolman, W. B., *J. Am. Chem. Soc*., **2015**, *137*, 1322-9.
(15) Dhar, D.; Yee, G. M.; Spaeth, A. D.; Boyce, D. W.; Zhang, H.; Dereli, B.; Cramer, C. J.; Tolman, W. B., *J. Am. Chem. Soc*., **2016**, *138*, 356-368.
(16) Mandal, M.; Elwell, C. E.; Bouchey, C. J.; Zerk, T. J.; Tolman, W. B.; Cramer, C. J. *J. Am. Chem. Soc*. **2019**, *141*, 17236-17244.
(17) Zerk, T. J.; Saouma, C. T.; Mayer, J. M.; Tolman, W. B., *Inorg. Chem*., **2019**, *58*, 14151-14158.
(18) Krishnan, V. M.; Shopov, D. Y.; Bouchey, C. J.; Bailey, W. D.; Parveen, R.; Vlaisavljevich, B.; Tolman, W. B., *J. Am. Chem. Soc*., **2021**, *143*, 3295-3299.
(19) Wu, T.; MacMillan, S. N.; Rajabimoghadam, K.; Siegler, M. A.; Lancaster, K. M.; Garcia-Bosch, I., *J. Am. Chem. Soc*., **2020**, *142*, 12265-12276.
(20) Wu, T.; Musgrove, J.; Siegler, M. A.; Garcia-Bosch, I., *Chem. Asian J*., **2021**, *16*, 1608-1618.
(21) Shimizu, I.; Morimoto, Faltermeier, Y. D.; Kerscher, M.; Paria, S.; Abe, T.; Sugimoto, H.; Fujieda, N.; Asano, K.; Suzuki, T.; Comba, P. Itoh, S., *Inorg. Chem*., **2017**, *56*, 9634-9645.
(22) Shimizu, I.; Morimoto, Y.; Velmurugan, G.; Gupta, T.; Paria, S.; Ohta, T.; Sugimoto, H.; Ogura, T.; Comba ,P.; Itoh, S., *Chem. Commun*., **2019**, *25*, 11157-11165.
(23) Lan, Y.; Morimoto, Y.; Shimizu, I.; Sugimoto, H. Itoh, S., *Inorg. Chem*., **2023**, *62*, 10539-10547.
(24) Yang, L.; Ito, R.; Sugimoto, H.; Morimoto, Y.; Itoh, S., *Chem. Commun*., **2024**, *60*, 7586-7589.
(25) Warren, J. J.; Tronic, T. A.; Mayer, J. M., *Chem. Rev*., **2010**, *110*, 6961-7001.
(26) Agarwal, R. G.; Coste, S. C.; Groff, B. D.; Heuer, A. M.; Noh, H.; Parada, G. A.; Wise, C. F.; Nichols, E. M.; Warren, J. J.; Mayer, J. M., *Chem. Rev*. **2022**, *122*, 1-49.
(27) Bordwell, F. G. *Acc. Chem. Res*., **1988**, *21*, 456-463.
(28) Manner, V. W.; Markle, T. F.; Freudenthal, J. H.; Roth, J. P.; Mayer, J. M., *Chem. Commun*., **2008**, *2*, 256-258.
(29) Ar, D.; A. Kilpatrick, F. R.; Cula, B.; Herwig, C.; Limberg, C., *Inorg. Chem*. **2021**, *60*, 13844-13853.
(30) Collman, J. P.; Decréau, R. A.; Sunderland, C. J., *Chem. Commun*., **2006**, *37*, 3894-3896.
(31) Mondal, P.; McDonald, A. R., *Chem. Eur. J*. **2020**, *26*, 10083-10089.
(32) Bailey, W. D.; Dhar, D.; A. Cramblitt, C.; Tolman, W. B., *J. Am. Chem. Soc*. **2019**, *141*, 5470-5480.
(33) Olmstead, W. N.; Margolin, Z.; Bordwell, F. G., *J. Org. Chem*., **1980**, *45*, 3295-3299.
(34) Barman, S. K.; Yang, M. Y.; Parsell, T. H.; Green, M. T.; Borovik, A. S., *Proc. Natl.*

Acad. Sci., **2021**, *118*, e2108648118.
(35) Barman, S. K.; Jones, J. R.; Sun, C.; Hill, E. A.; Ziller, J. W.; Borovik, A. S., Borovik, *J. Am. Chem. Soc.*, **2019**, *141*, 11142-11150.
(36) Perrin, D. D.; Armarego, W. L. F.; Perrin, D. R., *Purification of Laboratory Chemicals 4th Edition*, 4th ed., Pergamon Press, Elmsford, NY, **1996**.

Supporting Information

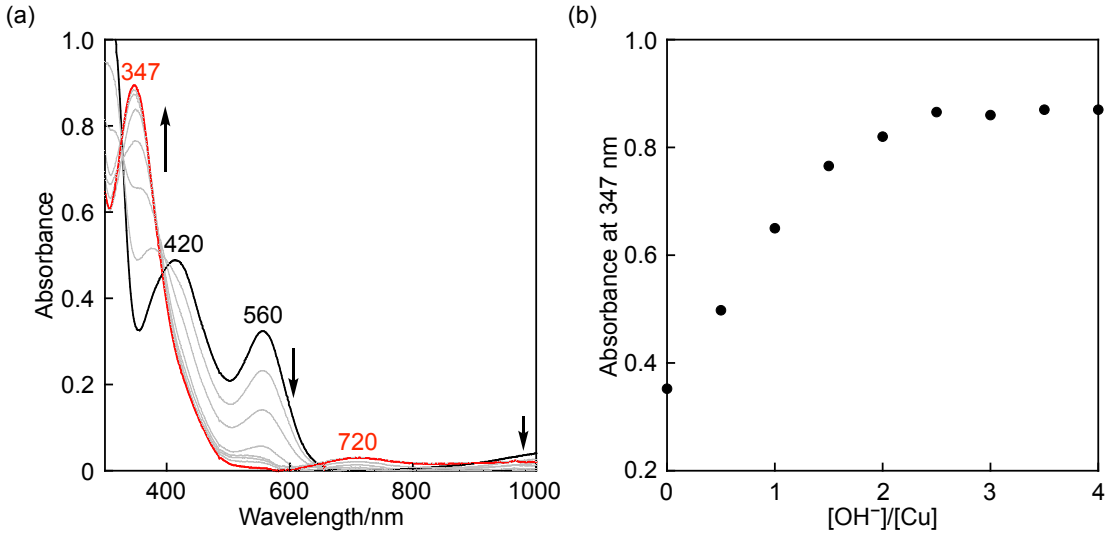

Figure S3-1. (a) UV-vis spectral changes observed upon addition of an MeOH solution containing TBAOH to a CH_2Cl_2 solution of $\mathbf{1^{Br}}$ (0.25 mM) at −20 °C. (b) Absorbance changes at 347 nm.

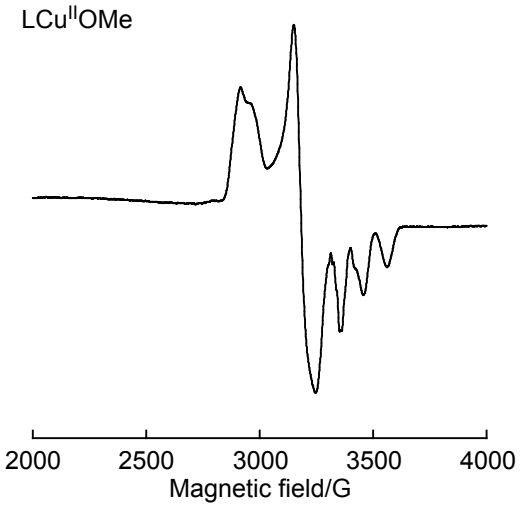

Figure S3-2. X-band (9.55 GHz, 4 mW) EPR spectrum of $\mathbf{1^{OMe}}$ (0.25 mM) measured at 107 K, $g_z = 2.36$, $g_y = 2.17$, $g_x = 2.03$, $A_x = 90$ G

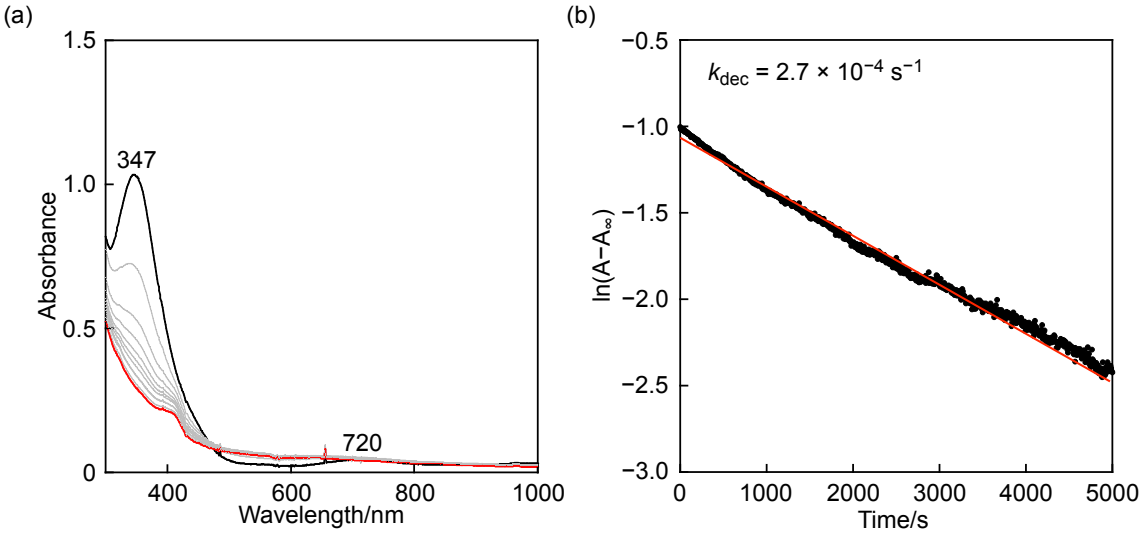

Figure S3-3. (a) UV-vis spectral changes for the decomposition of **1**$^{\mathbf{OMe}}$ (0.25 mM) in CH_2Cl_2 at −20°C. (b) First-order plot based on the absorption change at 347 nm.

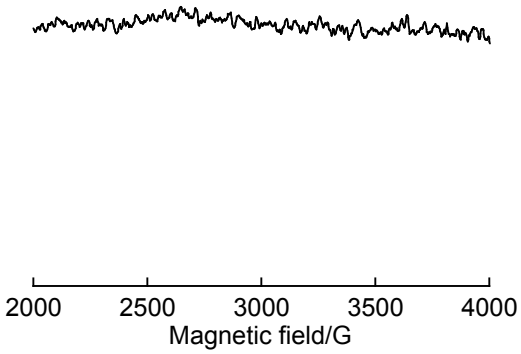

Figure S3-4. X-band (9.55 GHz, 4 mW) EPR spectrum of the post-reaction solution of **1**$^{\mathbf{OMe}}$ and CHD measured at 104 K.

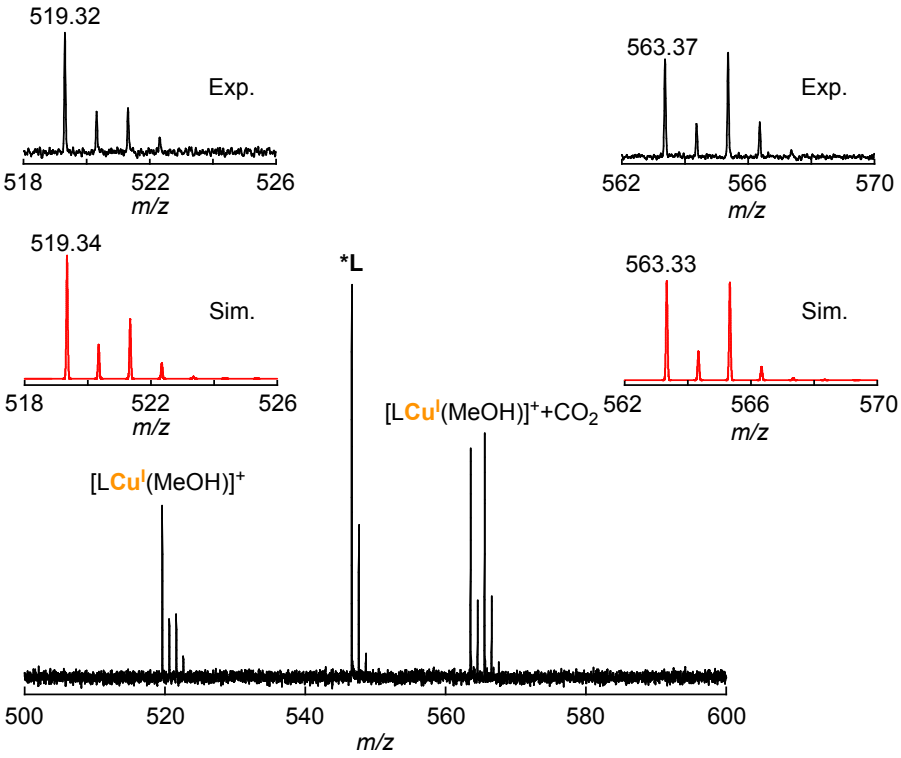

Figure S3-5. ESI-MS of the post-reaction solution showing the formation of $[(TMG_3tach)Cu^{I}(MeOH)]^+$ in the reaction of $\mathbf{1^{OMe}}$ and 1,4-cyclohexadien (CHD). The peak at *m/z* = 546.3 denoted as ***L** corresponds to a molecule consisting with TMG_3tach, Na^+ and 3 MeOH.

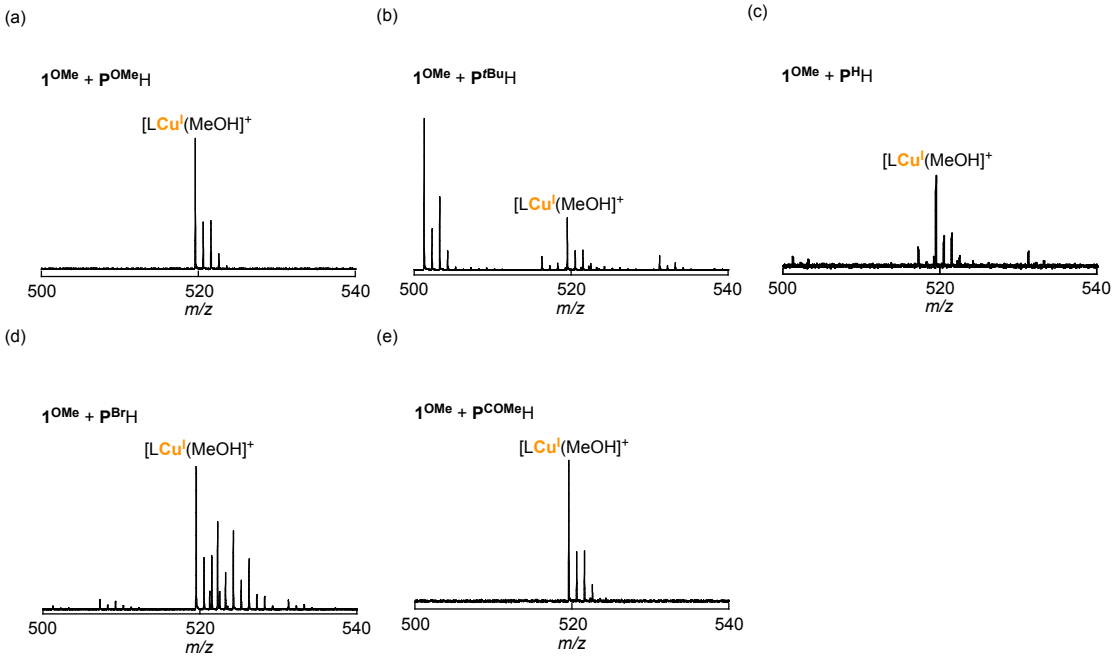

Figure S3-6. ESI-MS of the post-reaction solutions showing the formation of $[(TMG_3tach)Cu^{I}(MeOH)]^{+}$ in the reaction of $\mathbf{1^{OMe}}$ and $P^{Y}H$ (Y = OMe, *t*Bu, H, Br, and COMe).

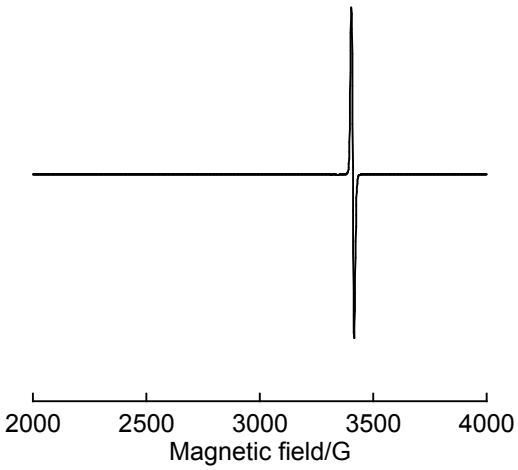

Figure S3-7. The X-band EPR spectrum of the post-reaction solutions between $\mathbf{1^{OMe}}$ and $\mathbf{P^{tBu}H}$ showing the formation of phenoxyl radical ($P^{tBu}\bullet$) at $g = 2.0041$ in CH_2Cl_2 at 110 K.

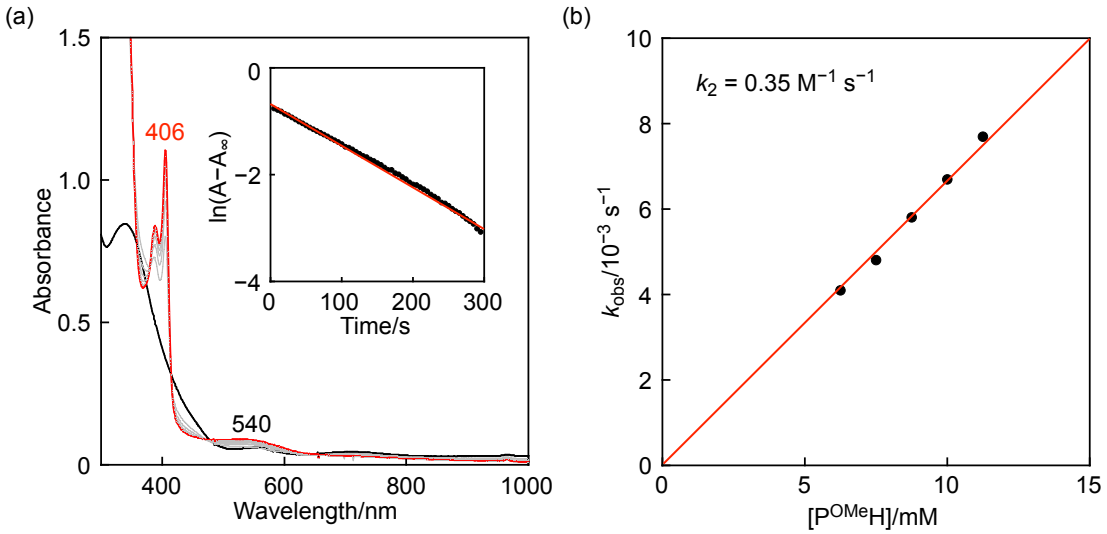

Figure S3-8. (a) UV-vis spectral changes for the reaction of **1^{OMe}** (0.25 mM) with 4-methoxy-2,6-di-*tert*-butylphenol (P^{OMe}H, 22.5 mM) in CH_2Cl_2 at −20°C. Inset: Pseudo first-order plot based on the absorption change at 405 nm. (b) Plot of k_{obs} vs. [P^{OMe}H].

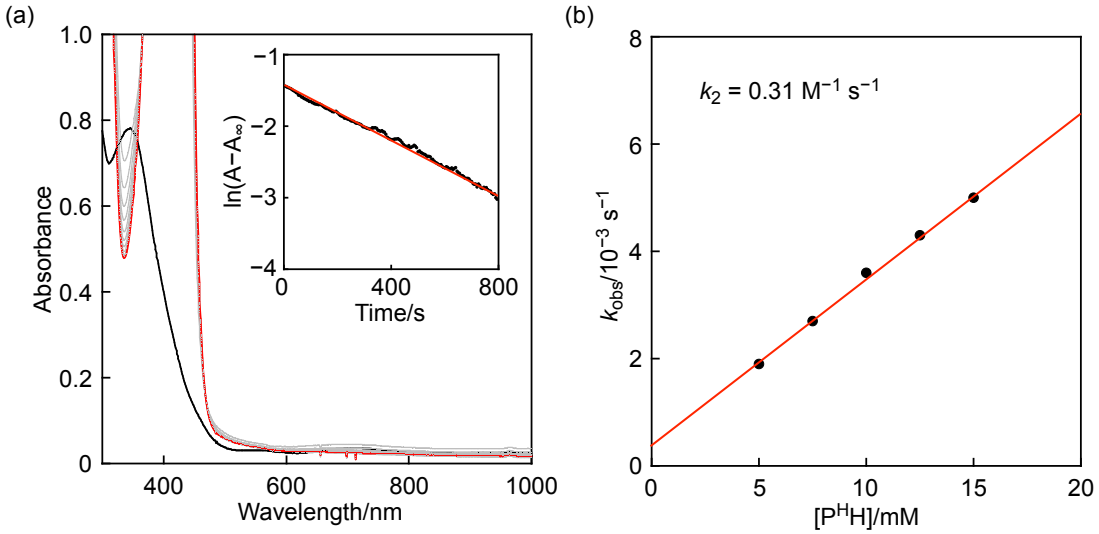

Figure S3-9. (a) UV-vis spectral changes for the reaction of **1^{OMe}** (0.25 mM) with 2,6-di-*tert*-butylphenol (P^{H}H, 5.0 mM) in CH_2Cl_2 at −20°C. Inset: Pseudo first-order plot based on the absorption change at 347 nm. (b) Plot of k_{obs} vs. [P^{H}H].

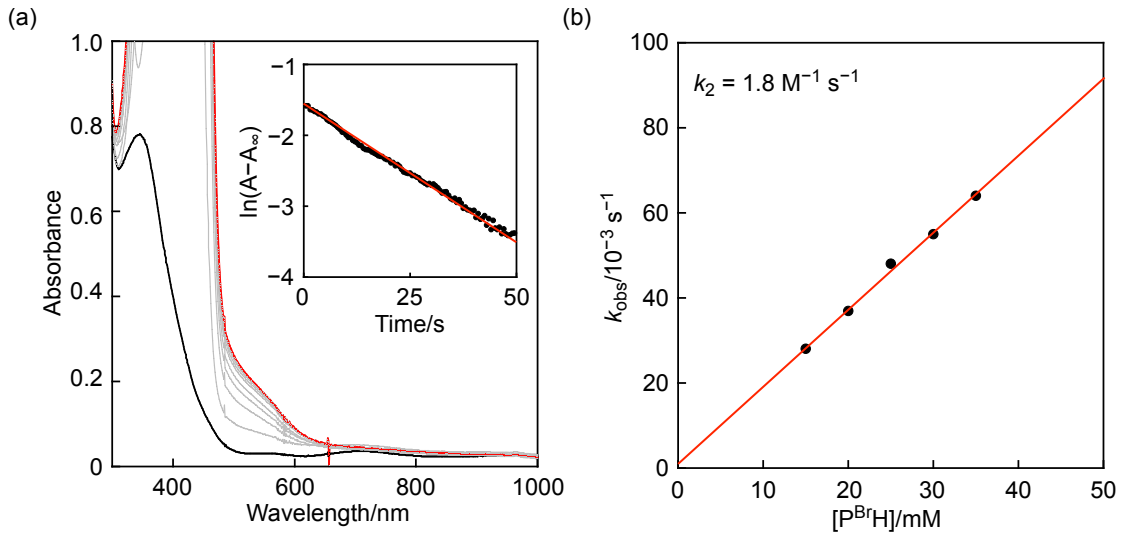

Figure S3-10. (a) UV-vis spectral changes for the reaction of **1**$^{\mathbf{OMe}}$ (0.25 mM) with 4-bromo-2,6-di-*tert*-butylphenol (P^{Br}H, 20 mM) in CH_2Cl_2 at −20°C. Inset: Pseudo first-order plot based on the absorption change at 500 nm. (b) Plot of k_{obs} vs. [P^{Br}H].

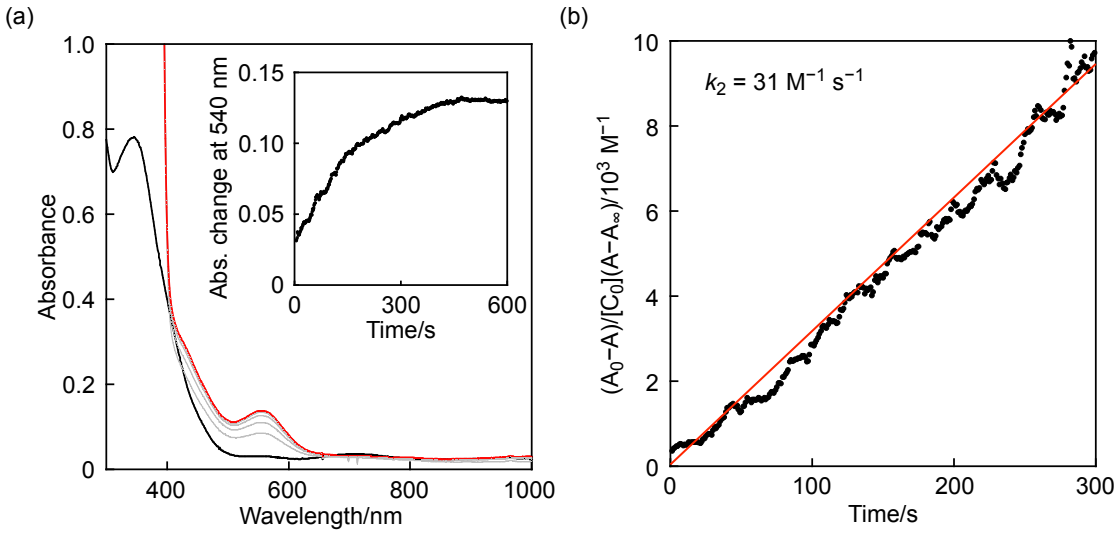

Figure S3-11. (a) UV-vis spectral changes for the reaction of **1**$^{\mathbf{OMe}}$ (0.25 mM) with 4-acetyl-2,6-di-*tert*-butylphenol (P^{COMe}H, 0.25 mM) in CH_2Cl_2 at −20°C. Inset: Absorption change at 540 nm. (b) Second-order plot.

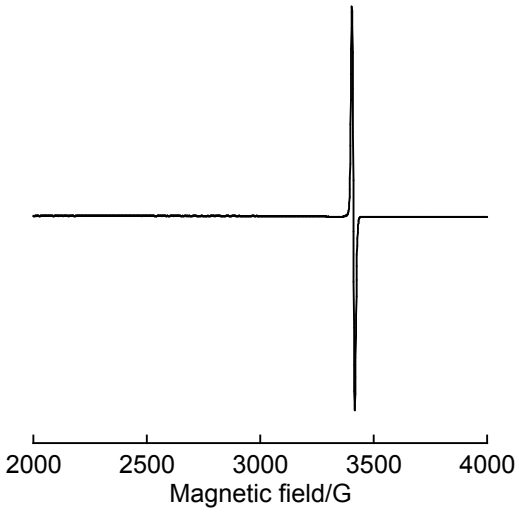

Figure S3-12. X-band EPR spectrum of the post-reaction solutions between $\mathbf{1}^{\mathbf{OMe}}$ and $P^{OMe}H$ showing the formation of phenoxyl radical (P^{OMe}•) at g = 2.0041 in CH_2Cl_2 at 110 K.

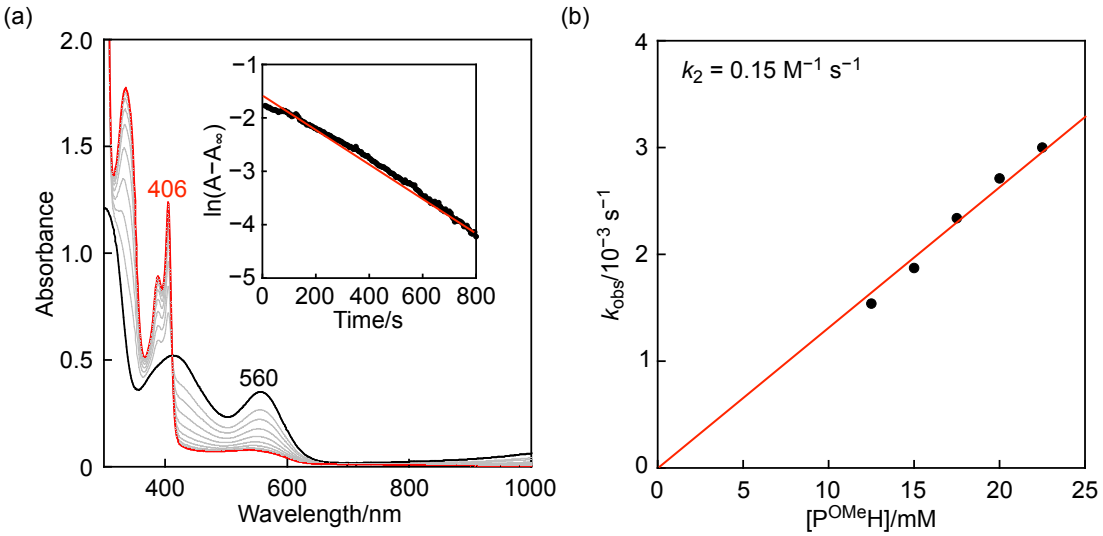

Figure S3-13. (a) UV-vis spectral changes for the reaction of $\mathbf{1}^{\mathbf{Br}}$ (0.25 mM) with 4-methoxy-2,6-di-*tert*-butylphenol ($P^{OMe}H$, 22.5 mM) in CH_2Cl_2 at −20°C. Inset: Pseudo first-order plot based on the absorption change at 560 nm. (b) Plot of k_{obs} vs. $[P^{OMe}H]$.

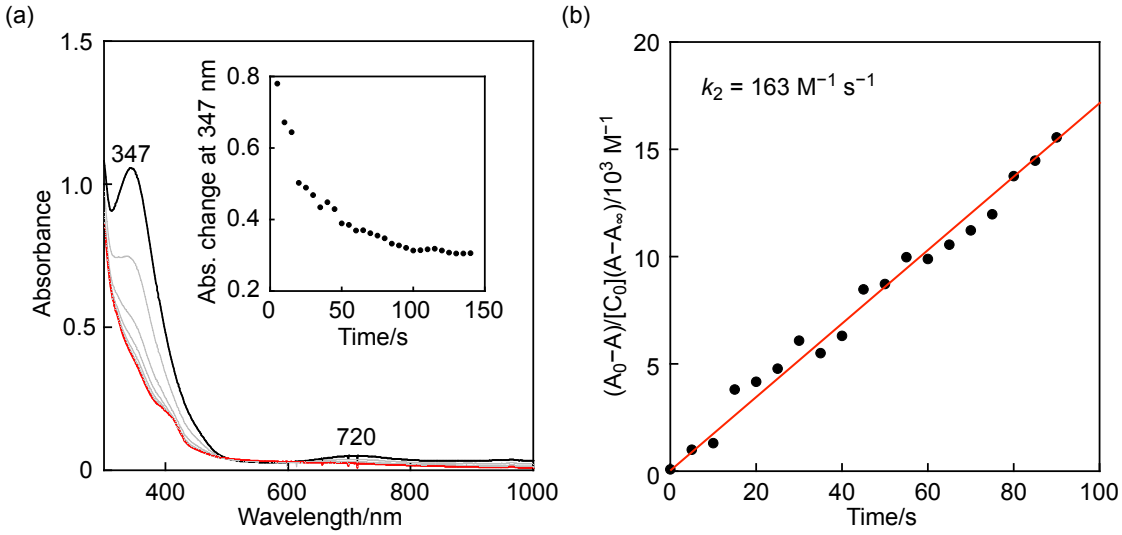

Figure S3-14. (a) UV-vis spectral changes for the reaction of $\mathbf{1}^{\mathbf{OMe}}$ (0.25 mM) with TEMPOH (0.25 mM) in CH_2Cl_2 at −20°C. Inset: Absorption change at 347 nm. (b) Second-order plot.

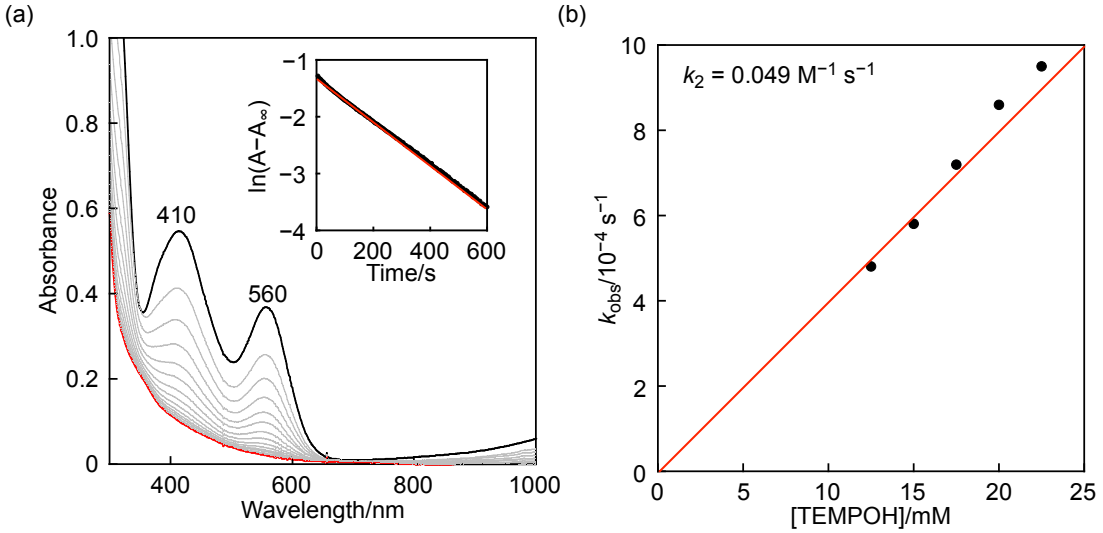

Figure S3-15. (a) UV-vis spectral changes for the reaction of $\mathbf{1}^{\mathbf{Br}}$ (0.25 mM) with TEMPOH (12.5 mM) in CH_2Cl_2 at −20°C. Inset: Pseudo first-order plot based on the absorption change at 560 nm. (b) Plot of k_{obs} vs. [TEMPOH].

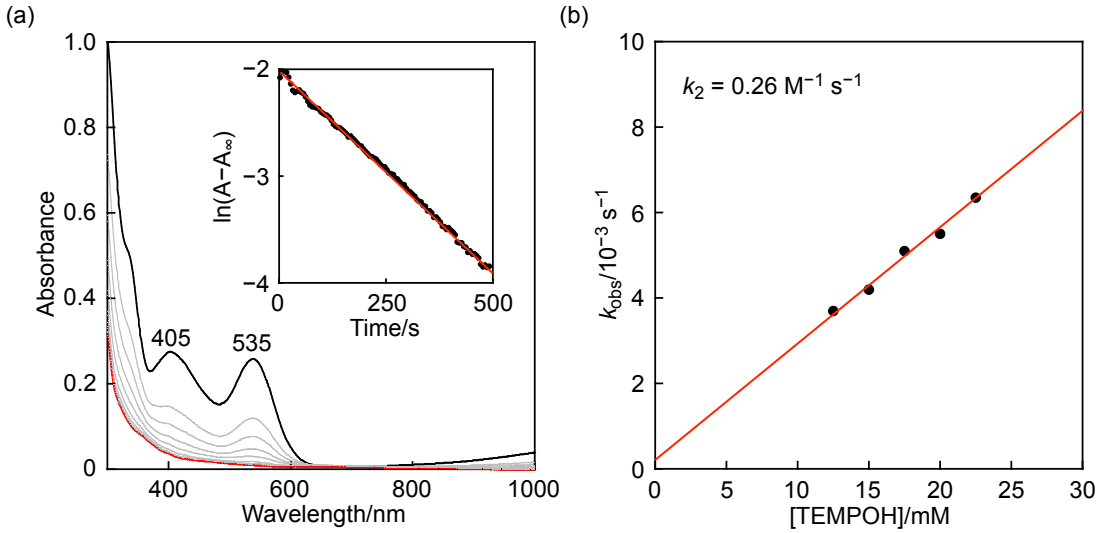

Figure S3-16. (a) UV-vis spectral changes for the reaction of $\mathbf{1}^{\mathbf{Cl}}$ (0.25 mM) with TEMPOH (12.5 mM) in CH_2Cl_2 at −20°C. Inset: Pseudo first-order plot based on the absorption change at 535 nm. (b) Plot of k_{obs} vs. [TEMPO-H].

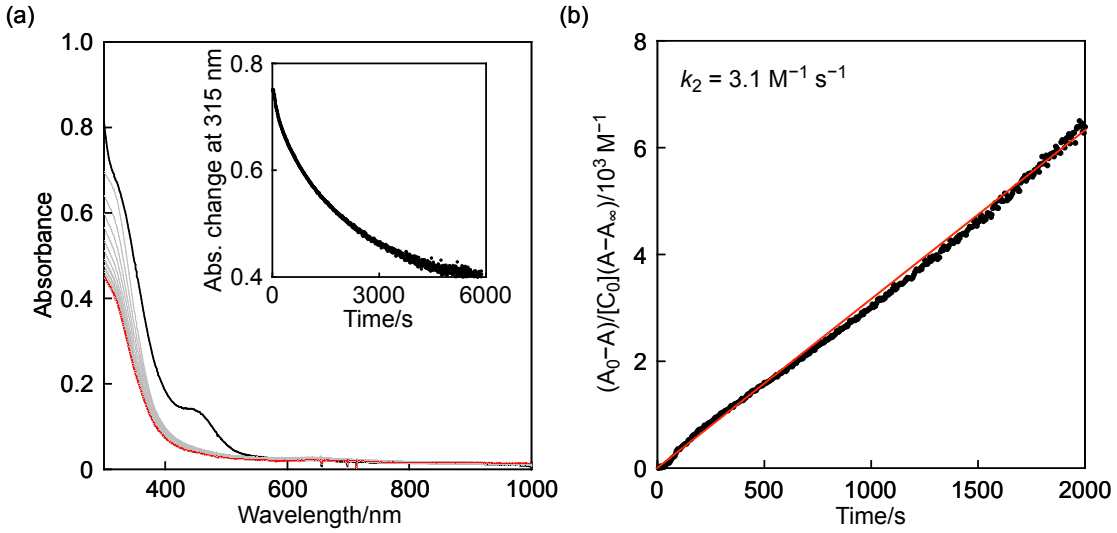

Figure S3-17. (a) UV-vis spectral changes for the reaction of $\mathbf{1}^{\mathbf{F}}$ (0.25 mM) with TEMPOH (0.25 mM) in CH_2Cl_2 at −20°C. Inset: Absorption change at 347 nm. (b) Second-order plot.

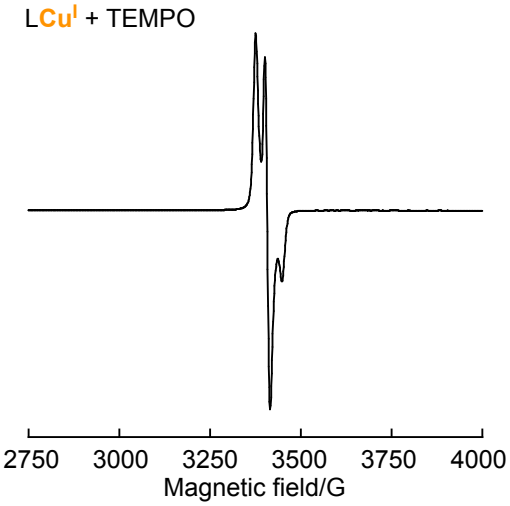

Figure S3-18. X-band (9.55 GHz, 4 mW) EPR spectra of the post-reaction solution of **1**$^{\mathbf{OMe}}$ and TEMPOH in CH_2Cl_2 at 104 K showing the formation of TEMPO radical at g = 2.0042.

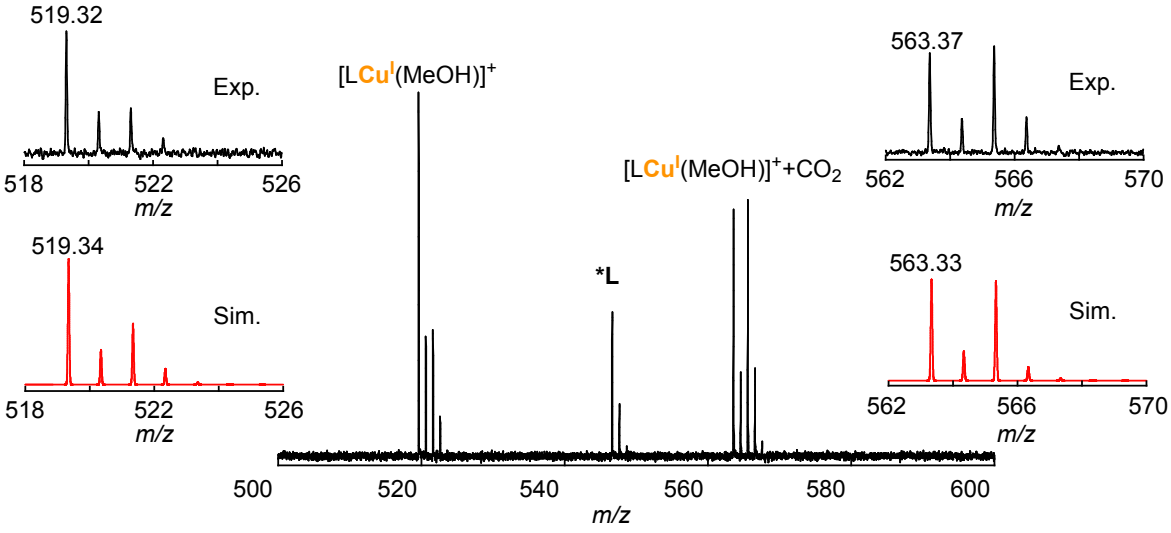

Figure S3-19. ESI-MS of the post-reaction solution showing the formation of [(TMG$_3$tach)Cu^{I}(MeOH)]$^{+}$ in the reaction of **1**$^{\mathbf{OMe}}$ and TEMPOH. The peak at m/z = 546.3 denoted as ***L** corresponds to a molecule consisting with TMG$_3$tach, Na^{+} and 3 MeOH.

General Conclusion

In summary, structures, physicochemical properties, and reactivities of a series of mononuclear tetrahedral copper(II) complexes $\mathbf{1^L}$ (L = F^-, Cl^-, Br^-, I^- and MeO^-) supported a N_3-tridentate ligand (TMG_3tach) were examined. In particular, the author focuses her attention on the geometric effect and the axial ligand effect of the copper(II) complexes. The results and findings in this research are summarized as follows.

In Chapter 1, it has been proved that $\mathbf{1^F}$ induced direct C–H bond activation of the external substrate CHD. Such a reactivity can be attributed to the basicity of F^- and unstable Cu(II) electronic state in tetrahedral geometry, resulting the higher hydrogen atom accepting ability.

In Chapter 2, the author examined the O−H activation reactions by copper(II)-halide complexes $\mathbf{1^X}$. A dichotomous phenomenon was observed, where the substrates having an EW-substituent are oxidized via proton-transfer/electron-transfer (PTET) mechanism and those having an ED-substituent undergoes concerted proton/electron transfer (CPET) mechanism. Moreover, the TMG group is shown to work as a proton accepter from the phenol substrate in the PTET mechanism, and in the reaction of $\mathbf{P^{COMe}}$H and $\mathbf{1^F}$, strong BDE of HF (product) greatly enhanced the reactivity.

In Chapter 3, the reactivity of a mononuclear tetrahedral copper(II)-methoxide complex supported by the same ligand TMG_3tach was examined in the C–H and O–H bond activation reactions using 1,4-cyclohexadiene (CHD), 4-sustituted-2,6-di-tert-butylphenol ($\mathbf{P^Y}$H), and 2,2,6,6-tetramethylpiperidin-1-ol (TEMPOH) as the substrates. In these reactions, $\mathbf{1^{OMe}}$ showed much higher reactivity compared to the copper(II)-halide complexes $\mathbf{1^X}$. Such an enhanced reactivity can be attributed to the higher basicity of methoxide (MeO^-) ligand compared to those of halide ligands (X^-), enhancing the proton-transfer process in the proton-coupled electron-transfer mechanism.

These new findings described in this thesis add new insights into the chemistry of mononuclear copper(II) complexes in a distorted tetrahedral geometry.

List of publications

1. Characterization and Reactivity Studies of Mononuclear Tetrahedral Copper(II)-Halide Complexes
Lan Yang, Yuma Morimoto, Ikuma Shimizu, Hideki Sugimoto, and Shinobu Itoh
Inorg. Chem. **2023**, *62*, 10539−10547 (DOI: 10.1021/acs.inorgchem.3c00320).

2. Oxidation Mechanism of Phenols by Copper(II)–halide Complexes
Lan Yang, Rin Ito, Hideki Sugimoto, Yuma Morimoto and Shinobu Itoh
Chem. Commun., **2024**, *60*, 7586-7589 (DOI: 10.1039/d4cc02483d).

3. Oxidation Reactivity of Mononuclear Tetrahedral Copper(II)-methoxide Complex
Lan Yang, Rin Ito, Hideki Sugimoto, and Shinobu Itoh
Coord. Chem. Res., under revision.

Acknowledgement

The studies presented in this thesis have been carried out under the guidance of Professor Shinobu Itoh at Osaka University during 2019-2025.

The author would like to express her gratitude to Professor Shinobu Itoh for kind guidance, invaluable suggestion, and continuous encouragement throughout his study.

Her gratitude also goes to Associate Professor Hideki Sugimoto and Dr. Yuma Morimoto for their excellent suggestion and continuous encouragement throughout her study.

Similarly, the author deeply appreciates Mr. Rin Ito for his considerable cooperation on the experiments in Chapter 2.

The author thanks all techniques in Analytical Division, Graduate School of Engineering, Osaka University for NMR, Mass Spectroscopy, EPR and Elemental Analysis.

Special thanks to all the members of Bio-Functional Chemistry (BFC) laboratory for their help, valuable suggestions, useful discussions, and friendship.

The author acknowledges financial support from Japan Science and Technology Agency (Support for Pioneering Research Initiated by the Next Generation).

Finally, the author acknowledges continuous encouragement and support given by her friends, and family, Xiaojuan Hu, Zhiliang Yang, Cuijiao Pan, Chaoyue Hu, Yunjiao Zhang, Dongcheng Yang, Baiwei Yang and Bailing Yang.

Osaka, Japan
January, 2025

Lan Yang

Bio-functional Chemistry Laboratory
Division of Applied Chemistry
Graduate School of Engineering
Osaka University